

1

UNIVERSITY OF BRISTOL

2

DOCTORAL THESIS

3

4

Investigating, implementing, and creating methods for analysing large neuronal ensembles

5

6

Author:

Thomas J. DELANEY

Supervisors:

Dr. Cian O'DONNELL

Dr. Michael C. ASHBY

7

9 *A thesis submitted in fulfillment of the requirements*

10 *for the degree of Doctor of Philosophy*

11 *in the*

12 Biological Intelligence & Machine Learning Unit

13 Department of Computer Science

14 August 28, 2020

15 Word count: 39000

¹⁶ **Declaration of Authorship**

¹⁷ I declare that the work in this dissertation was carried out in accordance with the requirements
¹⁸ of the University's Regulations and Code of Practice for Research Degree Programmes
¹⁹ and that it has not been submitted for any other academic award. Except where indicated by
²⁰ specific reference in the text, the work is the candidate's own work. Work done in collabora-
²¹ tion with, or with the assistance of, others, is indicated as such. Any views expressed in the
²² dissertation are those of the author.

²³ Signed:

²⁴ _____

²⁵ Date:

²⁶ _____

Acknowledgements

28 I would like to thank my supervisors, Cian O'Donnell and Mike Ashby, for their help, en-
29 couragement, advice, and patience over the last four years. This includes not only helping
30 with research, but also enabling and encouraging me to make the most of my opportunities
31 during that time. Without their help, I would not have grown as much as I have done in those
32 years. I very grateful for their time and effort.

33 I would also like to thank the members of the Bristol Computational Neuroscience Unit
34 for introducing me to all the various aspects of computer science, neuroscience, and machine
35 learning, of which I otherwise would not have heard. As the first person to introduce me to
36 the concept of mathematical neuroscience during my undergraduate days, and a great source
37 of advice and guidance during my PhD, I would also like to thank Conor Houghton.

38 Personally, I would like to thank my girlfriend Ashley, who has been nothing but helpful since
39 I met her.

40 Finally, I would like to thank my father, mother, brother and sister. I am truly fortunate to
41 have such a good family. I thank them for their love, encouragement, and excellent example.

42 *Abstract*

43 Since the use of multi-electrode recording in neuroscience began, the number neurons
44 being recorded in parallel has been increasing. Recently developed methods using calcium
45 or voltage imaging have also contributed to the growth in neuronal datasets. As datasets grow,
46 the need for new analysis methods also grows. In this research we attempted to address some
47 of the problems associated with reading from large neuronal ensembles using fluorescent
48 calcium indicators, and some of the problems with analysing data read from large neuronal
49 ensembles.

50 We created a biophysical model for the fluorescence trace produced by a calcium indicator
51 responding to a given spike train. Our model reproduced the characteristics of a real
52 fluorescence trace recognised by spike inference algorithms. This model will be useful for
53 anyone using or considering calcium imaging.

54 To find order in the correlated behaviour of a large multi-region neuronal ensemble, we
55 applied a novel method from network science to detect structure and communities in corre-
56 lated behaviour. We investigated the similarities between these communities and their brain
57 anatomy. Our results indicate local correlated networks function at shorter timescales (<
58 50ms), while multi-region correlated networks function over longer timescales (> 100ms).
59 This result agrees with previous findings from EEG data, but has not been shown before using
60 spiking data.

61 We developed a statistical model for the number of neurons spiking in a neuronal ensem-
62 ble based on the Conway-Maxwell-binomial distribution. Our aim was to capture correlated
63 activity in a neuronal population without measuring correlation coefficients directly. The
64 model captured correlated activity at very short timescales better than measuring correlation
65 coefficients. We also replicated one of the findings of Churchland et al. (2010) relating to
66 the quenching of neural variability at stimulus onset. We propose a connection between this
67 result and the changes in association captured by our model.

68 **Contents**

69	Declaration of Authorship	iii
70	Acknowledgements	v
71	Abstract	vii
72	1 Introduction	1
73	1.1 Overview	1
74	1.2 Modelling the fluorescence of calcium indicators	2
75	1.3 Functional networks	4
76	1.4 A new statistical model for capturing correlated behaviour	6
77	2 Sensitivity of the spikes-to-fluorescence transform to calcium indicator and neu-	
78	ron properties	9
79	2.1 Introduction	10
80	2.2 Methods	12
81	2.2.1 Calcium dynamics model	12
82	Photon release & capture	14
83	2.2.2 Parameter optimisation	15
84	Fixed parameters	17
85	2.2.3 Julia	17
86	2.2.4 Spike inference	18
87	Comparing spike inference quality	22
88	2.2.5 Perturbation analysis	22
89	2.2.6 Signal-to-noise ratio	23
90	2.2.7 Data sources	23
91	2.3 Results	23
92	2.3.1 A biophysical computational model can generate accurate fluores-	
93	cence traces from spike trains	23

94	2.3.2	Spike inference algorithms perform similarly on real data compared with time series simulated from the model	25
95	2.3.3	Relative effects of various buffers to the fluorescence signal	25
96	2.3.4	Spike inference accuracy is sensitive to indicator properties, and likely varies within and between cells	28
97	2.3.5	Single spike inference accuracy drops for high firing rates, but firing rate itself can be estimated from mean fluorescence amplitude	32
98	2.4	Discussion	34
102	3	Functional networks expand across anatomical boundaries as correlation time- scale increases	39
103	3.1	Introduction	40
104	3.2	Data	41
105	3.2.1	Brain regions	41
106	3.2.2	Video recordings	42
107	3.3	Methods	42
108	3.3.1	Binning data	42
109	3.3.2	Correlation coefficients	43
110		Total correlations, r_{SC}	43
111		Shuffled total correlations	44
112		Separating Correlations & Anti-correlations	44
113	3.3.3	Conditioning on behavioural data	44
114		Linear regression	44
115		Elastic net regularisation	45
116		Conditional covariance	46
117		Measures of conditional correlation	47
118	3.3.4	Information Theory	47
119		Entropy $H(X)$	47
120		Maximum entropy limit	48
121		Mutual Information $I(X; Y)$	49
122		Variation of Information $VI(X, Y)$	51
123		Measuring entropies & mutual information	51
124	3.3.5	Network analysis	51
125		Correlation networks	51

127	Rectified correlations	52
128	Sparsifying data networks	52
129	Communities	52
130	Weighted configuration model	53
131	Sparse weighted configuration model	53
132	Spectral rejection	53
133	Node rejection	54
134	Community detection	55
135	3.3.6 Clustering Comparison	55
136	Adjusted Rand Index	55
137	Clusterings as random variables	56
138	Information based similarity measures	57
139	Information based metrics	58
140	Comparing detected communities and anatomical divisions	58
141	3.4 Results	59
142	3.4.1 Average correlation size increases with increasing time bin width	59
143	3.4.2 Goodness-of-fit for Poisson and Gaussian distributions across increasing time bin widths	60
144	3.4.3 Differences between and inter- and intra- regional correlations decrease with increasing bin width	62
145	3.4.4 Connected and divided structure in correlation based networks reduces in dimension with increasing bin width	63
146	3.4.5 Detecting communities in correlation based networks	67
147	3.4.6 Functional communities resemble anatomical division at short timescales	67
148	3.4.7 Conditional correlations & signal correlations	69
149	3.4.8 Absolute correlations and negative rectified correlations	74
150	3.5 Discussion	77
151	4 A simple two parameter distribution for modelling neuronal activity and capturing neuronal association	81
152	4.1 Introduction	82
153	4.2 Data	83
154	4.2.1 Experimental protocol	83
155	4.3 Methods	84

160	4.3.1	Binning data	84
161	4.3.2	Number of <i>active</i> neurons	84
162	4.3.3	Moving windows for measurements	84
163	4.3.4	Fano factor	86
164	4.3.5	Probability Distributions suitable for modelling ensemble activity	86
165		Association	86
166		Binomial distribution	87
167		Beta-binomial distribution	87
168		Conway-Maxwell-binomial distribution	88
169	4.3.6	Fitting	90
170	4.3.7	Goodness-of-fit	92
171	4.4	Results	92
172	4.4.1	Increases in mean number of active neurons and variance in number of active neurons at stimulus onset in some regions	92
173		Primary visual cortex	93
174		Hippocampus	93
175		Thalamus	93
176	4.4.2	Conway-Maxwell-binomial distribution is usually a better fit than binomial or beta-binomial	93
177	4.4.3	Relative goodness-of-fit for binomial, beta-binomial, and COMb distributions	98
178		Log likelihoods of distributions fitted to stimulated and unstimulated responses	98
179		Distribution of fitted parameters for stimulated and unstimulated responses	100
180		Examples of empirical distributions and fitted distributions	102
181	4.4.4	Conway-Maxwell-binomial distribution captures changes in association at stimulus onset	102
182	4.4.5	Replicating stimulus related quenching of neural variability	102
183	4.4.6	Effects of greater bin widths	105
184	4.5	Discussion	106
191	5	Studies with practical limitations & negative results	109
192	5.1	Dynamic state space model of pairwise and higher order neuronal correlations	110

193	5.2 A multiscale model for hierarchical data applied to neuronal data	110
195	6 Discussion	113
196	Bibliography	121

¹⁹⁷ List of Figures

198	2.1 A: Example spike train (blue) and the corresponding GCaMP6s fluorescence	
199	trace (green), data replotted from (Berens et al., 2018). Inset shows zoomed	
200	section of traces to highlight slow decay of GCaMP6s fluorescence relative	
201	to spike time intervals. B: Schematic diagram of the neuron calcium and	
202	GCaMP computational model. C: Good visual match of data fluorescence	
203	trace (green) and model simulated fluorescence (orange) in response to an	
204	identical spike train (blue).	11
205	2.2 A: Workflow to compare spike inference for real versus simulated fluores-	
206	cence data. B: True positive rates achieved by three different spike inference	
207	algorithms when applied to observed spike trains, and simulated spike trains.	
208	Data points overlaid as blue circles. The performance is similar from real	
209	and simulated data for each of the algorithms.	26
210	2.3 Calcium Buffering Dynamics (A) The proportions of bound and free cal-	
211	cium concentrations within a cell, with the associated spike train. (B)-(F)	
212	The dynamics of the concentration of (B) excited indicator bound calcium,	
213	(C) indicator bound calcium, (D) immobile endogenous buffer bound cal-	
214	cium, (E) mobile endogenous buffer bound calcium, and (F) free calcium in	
215	response to an action potential at \sim 23.2s.	27

216	2.4 (A) An example trace for each of the five pairs of values used for the binding	
217	and unbinding rates of the fluorescent calcium indicator. (B) The signal-to-	
218	noise ratio of the modelled fluorescence traces using each of the four per-	
219	turbed value pairs, and the experimental value. The SNRs for the value pairs	
220	perturbed downward are lower than that for the unperturbed value pair or	
221	the higher value pairs. (C) The true-positive rates of the deconvolution al-	
222	gorithm's predictions when inferring from the observed data, and inferring	
223	from modelled traces using the perturbed and experimental values. We used	
224	the OASIS algorithm for spike inference here. The results from the other	
225	spike inference methods were similar, with their true positive rates scales	
226	similarly to figure 2.2 B.	30
227	2.5 (A) An example trace for each of the five perturbed values for the concen-	
228	tration of fluorescent calcium indicator. The top two traces are produced	
229	by the lower perturbed values, the middle trace is produced by the experi-	
230	mental value, and the lowest two traces are produced when using the higher	
231	perturbed values. (B) The signal-to-noise ratio of the modelled fluorescence	
232	traces using each of the four perturbed values, and the experimental value.	
233	Extreme perturbations of the concentration either above or below the experi-	
234	mental level lowered the SNR. (C) The true-positive rates of the deconvolu-	
235	tion algorithm's predictions when inferring from the observed data, and	
236	inferring from modelled traces using the perturbed and experimental values.	
237	We found that the algorithms performs equally badly on the two most ex-	
238	treme values, and performs equally well on the experimental value, and the	
239	next higher perturbed value. We used the OASIS algorithm for spike infer-	
240	ence here. The results from the other spike inference methods were similar,	
241	with their true positive rates scales similarly to figure 2.2 B.	31

242	2.6 (A) An example trace for each of the five perturbed values for the concentration of immobile endogenous buffer. (B) The signal-to-noise ratio of the modelled fluorescence traces using each of the four perturbed values, and the experimental value. The lower values for the immobile buffer produce the same SNR as the experimental value. But the higher perturbed values produce fluorescence traces with a lower SNR. (C) The true-positive rates of the deconvolution algorithm's predictions when inferring from the observed data, and inferring from modelled traces using the perturbed and experimental values. We used the OASIS algorithm for spike inference here. The results from the other spike inference methods were similar, with their true positive rates scales similarly to figure 2.2 B.	33
253	2.7 Simulating fluorescence traces at different firing rates Example modelled traces created using simulated spike trains with a mean firing rate of 1Hz (left column), 5Hz (middle column), and 10Hz (right column). Note the difference in amplitude with different mean firing rates.	34
256	2.8 Inference quality and $\Delta F / F_0$ vs Firing rate (left) The spike inference accuracy when applied to 30 traces created using simulated spike trains with mean firing rates of 1, 5, and 10 Hz. (right) The mean $\Delta F / F_0$ across those 30 traces for each frequency.	34
261	3.1 Probe Locations: The locations of the probes in each of the three mouse brains (Stringer et al., 2019).	42
263	3.2 Entropy Limit: The upper limit on entropy of binned spike count data as a function of the maximum observed spike count. The orange line is the analytical maximum. The blue line is the entropy of samples with $N = 1000$ data points taken from the discrete uniform distribution.	49
268	3.3 (A) An example of the correlation coefficients between two different pairs of cells, one where both cells are in the same brain region (intra-regional pair), and one where both cells are in different brain regions (inter-regional pair). The correlation coefficients have been measured using different time bin widths, ranging from 5ms to 3s. Note the increasing amplitude of the correlations with increasing bin width. (B) A raster plot showing the spike times of each pair of cells.	59

274	3.4	Mean correlation coefficients measured from pairs of 50 randomly chosen neurons. (A) All possible pairs, (B) positively correlated pairs, and (C) neg- atively correlated pairs. (D) Mean and standard error of χ^2 test statistics for Poisson and Gaussian distributions fitted to neuron spike counts.	61
275			
276			
277			
278	3.5	(Left)The mean intra-region and inter-region correlations using all possible pairs of ~ 500 neurons, spread across 9 different brain regions. (Right) Courtesy of Stringer et al. (2019), mean inter-regional (out-of-area) correla- tion coefficients vs mean intra-regional (within-area) correlation coefficients for a bin width of 1.2s. Note that the intra-regional coefficients are higher in each case.	63
279			
280			
281			
282			
283			
284	3.6	The mean intra-regional correlations (coloured dots) and mean inter-regional correlations (black dots) for a given region, indicated on the x-axis, for dif- ferent time bin widths. Each black dot represents the mean inter-regional correlations between the region indicated on the x-axis and one other region. (A) shows these measurements when we used a time bin width of 5ms. (B) shows these measurements when we used a time bin width of 1s. Note that the difference between the mean inter-regional correlations and mean intra- regional correlations is smaller for 1s bins.	64
285			
286			
287			
288			
289			
290			
291			
292	3.7	Mean inter-regional (main diagonal) and intra-regional (off diagonal) corre- lation coefficients. (A) Shows these measurements when spike times were binned using 5ms time bins. (B) Shows the same, using 1s time bins. Note that the matrices are ordered according to the main diagonal values, therefore the ordering is different in each subfigure.	65
293			
294			
295			
296			
297	3.8	The number of dimensions in the k -partite and connected structure in the cor- relation based networks beyond the structure captured by a sparse weighted configuration null network model (see section 3.3.5), shown for different time bin widths. Note that the k -partite structure disappears for time bin width greater than 200ms for all three subjects. The dimension of the connected structure reduces with increasing bin width for 2 of the 3 subjects (top row). .	66
298			
299			
300			
301			
302			

303	3.9 (A-B) Correlation matrices with detected communities indicated by white	
304	lines. Each off main diagonal entry in the matrix represents a pair of neu-	
305	rons. Those entries within a white square indicate that both of those neurons	
306	are in the same community as detected by our community detection proce-	
307	dure. Matrices shown are for 5ms and 1s time bin widths respectively. Main	
308	diagonal entries were set to 0. (C-D) Matrices showing the anatomical dis-	
309	tribution of pairs along with their community membership. Entries where	
310	both cells are in the same region are given a colour indicated by the colour	
311	bar. Entries where cells are in different regions are given the grey colour also	
312	indicated by the colour bar.	68
313	3.10 (A) The variation of information is a measure of distance between cluster-	
314	ings. The distance between the anatomical ‘clustering’ and community de-	
315	tection ‘clustering’ increases with increasing time bin width. (B) The ad-	
316	justed Rand index is a normalised similarity measure between clusterings.	
317	The anatomical and community detection clusterings become less similar as	
318	the time bin width increases.	69
319	3.11 Comparing the components of the total covariance across different values for	
320	the time bin width. We observed a consistent increase in $E[\text{cov}(X, Y Z)]$ as	
321	the time bin width increased. But we saw different trends for $\text{cov}(E[X Z], E[Y Z])$	
322	for each mouse.	70
323	3.12 Comparing the components of the total covariance across different values for	
324	the time bin width. We saw a consistent increase in $\rho_{X,Y Z}$ as the time bin	
325	width increased in all three subjects. But we saw different trends in ρ_{signal} for	
326	each of the subjects.	71
327	3.13 Matrices showing the regional membership of pairs by colour, and the com-	
328	munities in which those pairs lie. (A-B) Detected communities and regional	
329	membership matrix for network based on rectified spike count correlation	
330	$\rho_{X,Y Z}$, using time bin widths of 0.005s and 1s respectively. (C-D) Detected	
331	communities and regional membership matrix for network based on rectified	
332	signal correlation ρ_{signal} , using time bin widths of 0.005s and 1s respectively.	72

333	3.14 Distance and similarity measures between the anatomical division of the neu-	
334	rons, and the communities detected in the network based on the spike count	
335	correlations $\rho_{X,Y Z}$. (A) The variation of information is a ‘distance’ mea-	
336	sure between clusterings. The distance between the anatomical ‘clustering’	
337	and the community clustering increases as the time bin width increases. (B)	
338	The adjusted Rand index is a similarity measure between clusterings. The	
339	detected communities become less similar to the anatomical division of the	
340	cells as the time bin width increases.	73
341	3.15 Distance and similarity measures between the anatomical division of the neu-	
342	rons, and the communities detected in the network based on the signal cor-	
343	relations ρ_{signal} . (A) The variation of information is a ‘distance’ measure be-	
344	tween clusterings. The distance between the anatomical ‘clustering’ and the	
345	community clustering increases as the time bin width increases. (B) The ad-	
346	justed Rand index is a similarity measure between clusterings. The detected	
347	communities become less similar to the anatomical division of the cells as	
348	the time bin width increases.	74
349	3.16 (A-B) Absolute correlation matrices with detected communities indicated by	
350	white lines. These communities are based on the absolute value of the total	
351	correlation between each pair of cells. Those entries within a white square in-	
352	dicate that both of those neurons are in the same community. Matrices shown	
353	are for 5ms and 1s time bin widths respectively. Main diagonal entries were	
354	set to 0. (C-D) Matrices showing the anatomical distribution of pairs along	
355	with their community membership. Regional membership is indicated by the	
356	colour bar. (E) Variation of information between the anatomical division of	
357	the cells, and the detected communities. (F) Adjusted Rand index between	
358	the anatomical division, and the detected communities.	75

359	3.17 (A-B) Sign reversed rectified correlation matrices with detected communities indicated by white lines. Those entries within a white square indicate that both of those neurons are in the same community. Matrices shown are for 5ms and 1s time bin widths respectively. Main diagonal entries were set to 0. (C-D) Matrices showing the anatomical distribution of pairs along with their community membership. Regional membership is indicated by the colour bar. (E) Variation of information between the anatomical division of the cells, and the detected communities. (F) Adjusted Rand index between the anatomical division, and the detected communities.	76
368	4.1 Figures showing the over-dispersion possible for a beta-binomial distribution relative to a binomial distribution. Parameters are shown in the captions. . .	88
370	4.2 Figures showing (A) the under-dispersion and (B) over-dispersion permitted by the COMb distribution relative to a binomial distribution. (C) illustrates that the p parameter of the COMb distribution does not correspond to the mean of the distribution, as it does for the binomial and beta-binomial distributions. (D) shows a heatmap for the value of the Kullback-Liebler divergence between the COMb distribution and the standard binomial distribution with same value for n , as a function of p and ν . The point of this figure is to give the reader a sense of how the values of p and ν influence the difference between the COMb distribution and the binomial distribution. The divergence is smallest when $\nu \approx 1$, or when $p \approx 0.5$. When $\nu = 1$, the PMF for the COMb distribution is the same as the PMF for the binomial distribution. When $p = 0.5$ the mass of the distribution is centred around $n/2$ for both the COMb and the binomial distribution. The difference between the two distributions is controlled by the ν parameter. The further the p and ν parameters are from 0.5 and 1 respectively, the greater the difference between the COMb distribution and the binomial distribution. Parameters for all figures are shown in the captions.	91

387	4.3 (A) Raster plot showing the spikes fired by 33 randomly chosen neurons in 388 the primary visual cortex. (B-C) (B) average and (C) variance of the number 389 of active neurons, measured using a sliding window 100ms wide, split into 390 100 bins. The midpoint of the time interval for each window is used as the 391 timepoint (x-axis point) for the measurements using that window. The grey 392 shaded area indicates the presence of a visual stimulus. The opaque line is 393 an average across the 160 trials that included a visual stimulus of any kind. 394 We can see a transient increase in the average number of active neurons and 395 the variance of this number, followed by a fluctuation and another increase.	94
396	4.4 (A) Raster plot showing the spikes fired by 33 randomly chosen neurons in 397 the hippocampus. (B-C) (B) average and (C) variance of the number of active 398 neurons, measured using a sliding window 100ms wide, split into 100 bins. 399 The midpoint of the time interval for each window is used as the timepoint (x- 400 axis point) for the measurements using that window. The grey shaded area 401 indicates the presence of a visual stimulus. The opaque line is an average 402 across the 160 trials that included a visual stimulus of any kind. We can see 403 a transient increase in the average number of active neurons and the variance 404 of this number at stimulus onset.	95
405	4.5 (A) Raster plot showing the spikes fired by 33 randomly chosen neurons in 406 the thalamus. (B-C) (B) average and (C) variance of the number of active 407 neurons, measured using a sliding window 100ms wide, split into 100 bins. 408 The midpoint of the time interval for each window is used as the timepoint (x- 409 axis point) for the measurements using that window. The grey shaded area 410 indicates the presence of a visual stimulus. The opaque line is an average 411 across the 160 trials that included a visual stimulus of any kind. We can 412 see in immediate increase at stimulus onset, a subsequent fall, and another 413 sustained increased until the stimulus presentation ends.	96

414	4.6 (A) An example of the binomial, beta-binomial, and Conway-Maxwell-binomial	
415	distributions fitted to a sample of neural activity. The Conway-Maxwell-	
416	binomial distribution is the best fit in this case. The histogram shows the	
417	empirical distribution of the sample. The probability mass function of each	
418	distribution is indicated by a different coloured line. (B) Across all samples	
419	in all trials, the proportion of samples for which each fitted distribution was	
420	the the best fit. The Conway-Maxwell-binomial distribution was the best fit	
421	for 93% of the samples taken from V1 using a bin width of 1ms.	97
422	4.7 Number of active neurons data from the primary visual cortex, 1ms bin	
423	widths. (Left column) Histograms of log likelihoods for the binomial, beta-	
424	binomial, and COMb distributions fitted to windows where no visual stimu-	
425	lus was present. 160 trials. (Right column) Similar histograms for windows	
426	where a visual stimulus was present. 160 trials. In both cases, there are	
427	marginal increases in the log likelihoods from binomial to beta-binomial to	
428	COMb. The log likelihoods are larger for the unstimulated windows.	99
429	4.8 Histograms of fitted parameters for binomial, beta-binomial, and COMb dis-	
430	tributions. Distributions fitted to data from the primary visual cortex, using	
431	1ms bin widths. (Left column) The distributions were fitted a window before	
432	the onset of the visual stimulus. (Right column) The distributions were fitted	
433	to a window immediately after the onset of the visual stimulus.	101
434	4.9 Examples of empirical and fitted distributions. At least one example from	
435	each of the 5 brain regions from which we had data.	103
436	4.10 (A) We fit a Conway-Maxwell-binomial distribution to the number of active	
437	neurons in 1ms time bins of a 100ms sliding window. We did this for all	
438	trials with a visual stimulus and took the average across those trials. We see	
439	a transient drop in value for the distribution's ν parameter at stimulus onset.	
440	This shows an increase in positive association between the neurons. (B) We	
441	measured the correlation coefficient between the spike counts of all possible	
442	pairs of neurons in the same sliding window. The took the average of those	
443	coefficients. We also did this for every visually stimulated trial, and took the	
444	average across trials. The increase in positive association is not reflected with	
445	an increase in average correlation.	104

446	4.11 (A) The mean Fano factor of the spike counts of the cells in the primary visual cortex. Means were taken across cells first, then across trials. There was a significant decrease in the Fano factors immediately after stimulus onset. (B) The mean Fano factor of the spike counts of the cells in the motor cortex. No significant change in measurements at any point.	105
451	4.12 (A) The mean ν parameter of the COMb distribution fitted to activity in the primary visual cortex. Mean taken across all stimulated trials. A bin width of 10ms was used to classify cells as active or inactive. The change in association at stimulus onset is still captured. Some high frequency fluctuations are filtered out by using the wider bins (compare to figure 4.10a) (B) The mean Fano factor of the cells in the primary visual cortex. The change in the mean Fano factor at stimulus onset is not significant when using a bin width of 10ms.	107
457		

458 List of Tables

459	2.1	Fixed parameters A table of the parameters fixed before optimising the	
460		model. The values of these parameters could be changed to model differ-	
461		ent fluorescent calcium indicators.	17
462	4.1	Details of the different bin width and analysis window sizes used when bin-	
463		ning spike times, and analysing those data.	85
464	4.2	Relative dispersion of the COMb distribution, and association between Bernoulli	
465		variables as represented by the value of the ν parameter.	90
466	4.3	Proportion of samples for which each distribution was the best fit, grouped	
467		by bin width. The COMb distribution is the best fit most of the time.	98

List of Abbreviations

COMb	Conway-Maxwell-binomial (distribution)
OASIS	Online active set method to infer spikes
SNR	Signal to noise ratio
NMI	Normalised mutual information
AMI	Adjusted mutual information
VI	Variation of information

⁴⁶⁹ **List of Symbols**

$[Ca^{2+}]$	Free calcium concentration	mol
$[BCa]$	Fluorescent indicator bound calcium	mol
$[ECa]$	Endogenous mobile buffer bound calcium	mol
$[ImCa]$	Immobile mobile buffer bound calcium	mol
$[BCa^*]$	excited fluorescent indicator bound calcium	mol
k_{X_f}	binding (affinity) rate	$mol^{-1} s^{-1}$
k_{X_b}	unbinding (dissociation) rate	s^{-1}

470 **Chapter 1**

471 **Introduction**

472 **1.1 Overview**

473 Since Hodgkin and Huxley's squid experiments featuring a single axon (Hodgkin and Hux-
474 ley, 1939), to more recent research with spike sorted data from ~ 24000 neurons from 34
475 brain regions from 21 mice (Allen et al., 2019), the number of neurons contributing to elec-
476 trophysiological datasets has been growing. The number of simultaneously recorded neurons
477 has doubled approximately every seven years since the use of multi-electrode recording in
478 neuroscience began (Stevenson and Kording, 2011). Recording methods using two-photon
479 calcium imaging have also been used to extract data from populations containing over 10000
480 neurons (Peron et al., 2015). This dramatic growth in the number of neurons available for
481 analysis requires a dramatic change in analysis methods.

482 There are multiple methods for reading activity from neuronal ensembles: electrophysiolog-
483 ogy, calcium imaging, and voltage imaging. Electrophysiology involves inserting electrodes
484 into the brain of an animal. The electrodes read extra-cellular membrane potential, and using
485 these readings we observe activity in the ensemble. Calcium imaging and voltage imaging
486 use indicator dyes or fluorescent proteins that emit fluorescence traces that indicate either
487 the concentration of calcium in a neuron's cytoplasm, or the neuron's membrane potential.
488 In this project, we have attempted to address some of the difficulties in collecting data from
489 these large ensembles using fluorescent calcium indicators, and some of the difficulties in
490 analysing the collected data.

491 The rest of this introductory chapter will give some background about methods of record-
492 ing from the brain, and some background for the rest of the document. Chapter two describes
493 a biophysical model for the fluorescence trace induced by a given spike train in a cell con-
494 taining a fluorescent calcium indicator. Our third chapter describes our investigations into

495 the correlated activity across different regions of a mouse behaving spontaneously. We ap-
496 plied a novel community detection method (Humphries et al., 2019) from network science
497 to correlation based networks of neurons, and observed differences in the structure of these
498 correlations at different timescales. In our fourth chapter, we detail a new statistical model
499 for the number of neurons spiking in a neuronal ensemble at any given moment. With this
500 model, we attempted to capture correlated activity in a new way. The fifth chapter is a brief
501 description of the work that yielded negative results or was abandoned. The final chapter is a
502 discussion of our work and results from the previous chapters and their implications.

503 1.2 Modelling the fluorescence of calcium indicators

504 To focus on calcium imaging for a start, a neuron that contains a fluorescent calcium indicator
505 in its cytoplasm will fluoresce when bombarded with photons. The amount that the cell
506 will fluoresce is dependent on the concentration of fluorescent indicator within the cell, and
507 the concentration of calcium within the cell. When a neuron fires an action potential, the
508 influx of free calcium ions causes an increase in fluorescence when those ions bond with the
509 fluorescent indicator and those bounded molecules are bombarded with photons. After the
510 action potential, as calcium is extruded from the cell the fluorescence returns to a baseline
511 level. This is the basic mechanism of fluorescent calcium indicator based imaging.

512 This method has some advantages over electrophysiology as measure of neuronal ensem-
513 ble activity. Many of the problems with electrophysiology are within the processes used to
514 isolate spikes in the extracellular voltage readings, and assign these spikes to individual cells.
515 These processes are collectively called ‘spike sorting’. A comparison of many different spike
516 sorting algorithms found that these algorithms only agreed on a fraction of cases (Buccino
517 et al., 2019). Furthermore, because electrodes measure extracellular voltage, neurons that do
518 not spike will not be detected. Isolating individual neurons is easier and more reliable when
519 using calcium imaging data, because cells will emit a baseline level of fluorescence when not
520 firing action potentials. Another advantage is that calcium imaging sites can be re-used for
521 weeks for longitudinal studies (Chen et al., 2013). One of the methods of delivering the flu-
522 orescent indicator is by adeno-associated viruses, consequently there can be problems with
523 indicator gradients around the infection site, and expression levels will change in individual
524 cells over weeks (Tian et al., 2009; Chen et al., 2013). This delivery method can also cause
525 cell pathology, and nuclear filling (Zariwala et al., 2012), but these problems can be solved by
526 using lines of transgenic mice (Dana et al., 2014). The fluorescence signal itself can serve a a

527 good indicator of cell activity, but similarly to electrophysiology, the aim of calcium imaging
528 is often spike detection.

529 If the imaging data is collected at a high enough frequency, and the signal-to-noise ratio
530 of the fluorescence trace is high enough, it should be possible to infer the spike times to some
531 level of accuracy. For example, the calmodulin based indicator GCaMP6s has a sufficiently
532 high signal-to-noise ratio that isolated action potentials can be detected and inferred (Chen
533 et al., 2013). Many spike inference algorithms exist (Vogelstein et al., 2010; Pnevmatikakis
534 et al., 2016; Friedrich and Paninski, 2016; Pnevmatikakis et al., 2013; Pnevmatikakis et al.,
535 2014; Deneux et al., 2016; Greenberg et al., 2018), and some of these can perform both cell
536 isolation and spike detection simultaneously (Vogelstein et al., 2010; Pnevmatikakis et al.,
537 2016; Pnevmatikakis et al., 2014; Deneux et al., 2016). But the relationship between spik-
538 ing and fluorescence change is not fully understood. For example, the fluorescent indicator
539 will act like an additional calcium buffer within the cell cytoplasm and will compete with
540 the other endogenous buffers to bind with free calcium ions. Therefore, the concentration
541 of those endogenous buffers, and the binding dynamics of those buffers will have an effect
542 on the change in fluorescence in response to an action potential. Furthermore, the binding
543 dynamics of the fluorescent indicator itself will have an effect on the change in fluorescence.
544 For example, the GCaMP series of fluorescence indicators are based on the calcium buffer
545 protein calmodulin. This protein has four binding sites, whose affinities interact non-linearly.
546 But most of the spike inference algorithms model the fluorescence as a linear function of
547 a calcium trace, and they model this calcium trace as a first or second order autoregression
548 with a pulse input to represent action potentials. Deneux et al. (2016) developed two dif-
549 ferent calcium fluorescence models behind their spike inference algorithm (MLspike) with a
550 more biological inspiration. For their simpler model, they take a physiological approach and
551 account for baseline calcium indicator dynamics. They end up with a system of first order
552 differential equations defining the dynamics of calcium concentration, baseline fluorescence,
553 and fluorescence. For their more complicated model specifically for genetically encoded cal-
554 cium indicators, they also took into account indicator binding and unbinding rates, which
555 added another equation to their system of equations. The algorithms that use the autore-
556 gression model and the MLspike algorithm are outperformed by the most recently published
557 spike inference algorithm (Greenberg et al., 2018). This algorithm takes into account the
558 binding dynamics of both the endogenous buffers and fluorescent calcium indicator, and the
559 concentrations of free calcium, indicator, and endogenous buffer within the cell cytoplasm.
560 The performance of this algorithm shows that there is value in more biologically inspired

561 models of fluorescent calcium indicators.

562 In light of the growing popularity of two-photon calcium imaging, and the lack of bio-
563 logically inspired spike inference algorithms ((Greenberg et al., 2018) developed their spike
564 inference algorithm in parallel to our work), we decided to develop a biologically inspired
565 model for fluorescent calcium indicator fluorescence. The idea being that our model would
566 take a spike train, or simply spike times, provided by the user, and return the fluorescence
567 trace that would be induced by this spike train or spike times. The model contains parameters
568 for concentrations of indicator and endogenous buffers, as well as affinity and unbinding rates
569 for these buffers. There are also parameters for the baseline concentration of free calcium in
570 the cell cytoplasm, and the cell radius (as a means for calculating the cell volume). With this
571 model, we hoped that experimentalists would be able to test out different calcium indicators
572 on the types of spike trains that they expect to encounter. This way they could decide ahead
573 of time which indicator suited their situation best. Since the output of our model is a fluo-
574 rescence trace, the spike inference models mentioned above can be applied to the modelled
575 fluorescence. This means that the model could also be used to benchmark the performance
576 of these spike inference algorithms, and to investigate the impact of variations in the model
577 on spike inference accuracy.

578 1.3 Functional networks

579 We have outlined some of the advantages that calcium imaging has over electrophysiology.
580 But electrophysiology is more useful in some situations. One particular drawback for two-
581 photon calcium imaging is that usually it can only be used for imaging near to the surface
582 of the brain. This problem can be solved by removing the tissue around the area to be im-
583 aged, and custom building a two-photon microscope Dombeck et al., 2010. Imaging with
584 three (or presumably more) photons may solve this problem in the future (Ouzounov et al.,
585 2017). A better option for reading activity from neurons beyond the surface of the brain is to
586 use Neuropixels probes (Jun et al., 2017). These probes can be used to read from thousands
587 of neurons simultaneously in many different areas of the brain (Allen et al., 2019; Stringer
588 et al., 2019; Steinmetz, Carandini, and Harris, 2019; Steinmetz et al., 2019). This brings us
589 to another problem for which we require new innovations in our analysis methods. Specif-
590 ically, analysing correlated behaviour in neural ensembles consisting of neurons from many
591 different brain regions.

592 Until the invention of new technologies such as the Neuropixels probes, most elec-
593 trophysiology datasets read from neurons in only one or two regions. Therefore most of
594 the research on interactions between neurons in different regions is limited to two regions
595 (Wierzynski et al., 2009; Patterson et al., 2014; Girard, Hupé, and Bullier, 2001). In chapters
596 3 and 4 we used datasets with neurons from 9 and 5 different brain regions respectively. In
597 their review of the interaction between growing the number of neurons in datasets and the
598 analysis methods applied to those dataset, Stevenson and Kording (2011) assert that an im-
599 portant objective of computational neuroscience is to find order in these kinds multi-neuron
600 of datasets. This was our main aim for the research described in chapter 3.

601 In light of recent findings based on correlated behaviour showing that spontaneous be-
602 haviours explain activity in many different parts of the brain that would otherwise be regarded
603 as noise (Stringer et al., 2019), that satiety is represented brain wide (Allen et al., 2019), and
604 that exploratory and non-exploratory states are represented in the amygdala (Gründemann
605 et al., 2019), it was clear that state representation or motor control had an influence on cor-
606 related behaviour in areas of the brain not usually associated with these tasks. Also, given
607 differences in timescales of fluctuations in different brain regions (Murray et al., 2014), and
608 different timescales for event representation in different brain regions (Baldassano et al.,
609 2017), we decided to investigate brain wide correlated behaviour at timescales ranging from
610 5ms up to 3s.

611 We started off measuring the correlations in spike counts between individual neurons in
612 our ensemble. These measurements induced a weighted undirected graph where each node
613 represented a neuron, and the weight of each edge was the strength of the correlation be-
614 tween the neurons represented by the nodes at either end of that edge. In order to put the
615 neurons into groups with correlated behaviour, we applied a novel community detection al-
616 gorithm (Humphries et al., 2019) to this graph. We repeated this analysis for timescales
617 from milliseconds to seconds. Bear in mind that our correlation based graph was completely
618 agnostic of the anatomical regions in which our cells resided. We then compared our corre-
619 lated communities to their anatomy at each timescale. In this way, we used a novel method,
620 never applied neuronal data before, to analyse the makeup of correlated communities across
621 different regions at different timescales.

622 1.4 A new statistical model for capturing correlated behaviour

623 Many important findings have been made by measuring the correlations between binned
624 spike counts, but there are some problems with this method of analysis. Firstly, the width
625 of the bins used to bin spike times into spike counts has an effect on the magnitude of the
626 correlations measured. Using a short bin width can cause your measurements to be artificially
627 small (Cohen and Kohn, 2011). This may not be an issue if one is considering relative size of
628 correlations when using the same bin width, but it is still not ideal. Secondly, while pairwise
629 correlations can capture most of the information in a small network (up to 40 cells) of highly
630 correlated cells (Schneidman et al., 2006), a model based on pairwise correlations alone will
631 fail to capture the activity of larger (~ 100 cells) networks, higher order correlated activity
632 is required (Ganmor, Segev, and Schneidman, 2011). One problem with these higher order
633 correlations is that they may be defined in different ways (Staude, Grün, and Rotter, 2010).
634 Furthermore if we want to include them in a model this usually involves greatly increasing the
635 number of parameters to fit, which increases the dimension of the parameter space leading
636 to the ‘curse of dimensionality’. Some models attempt to sidestep these problems while
637 still capturing higher-order correlations. These models attempt to capture the relationship
638 between each individual neuron in the ensemble, and the ensemble as a whole. Okun et al
639 (2015) called the strength of this relationship the ‘population coupling’, and demonstrated
640 that this quantity can predict an individual neuron’s response to optogenetic stimulation of
641 the whole ensemble. They also showed that this quantity was an indicator of the neuron’s
642 synaptic connectivity (Okun et al., 2015). With the ‘population tracking model’, O’Donnell
643 et al. (2016) linked the probability of firing an action potential for each individual neuron
644 with the distribution of the number of active neurons. This allowed model fitting for a large
645 number of neurons, as well as calculation of full pattern probabilities, and population entropy
646 (O’Donnell et al., 2017).

647 In this work, we also aimed to capture correlated behaviour between the neurons in a
648 neuronal ensemble without measuring correlations directly. Correlation coefficients capture
649 the linear component of the relationship between two random variables, but will not mea-
650 sure any relationship beyond linearity. Also, measuring correlation coefficients using short
651 timebins can be difficult for neuronal data (Cohen and Kohn, 2011). We decided to abandon
652 correlation, and we aimed to quantify a more general concept of association by modelling
653 the number of active neurons in the ensemble using a Conway-Maxwell-binomial (COMb)
654 distribution (Kadane, 2016).

655 The COMb distribution is a probability distribution over the number of successes in a
656 sequence of Bernoulli trials, where these trials can be associated in some way. The COMb
657 distribution is an extension of the standard binomial distribution, with an additional parameter
658 to model association between the Bernoulli variables. Using this additional parameter the
659 distribution can capture positive association, where the Bernoulli variables tend to take the
660 same value, negative association, where the Bernoulli variables tend to take opposite values,
661 or no association i.e. the standard binomial distribution.

662 We fit a COMb distribution to spike sorted electrophysiological data taken from five
663 different regions in the brain of an awake mouse exposed to visual stimuli (Steinmetz et al.,
664 2019). We examined whether or not a model based on the COMb distribution was able to
665 capture changes in the number of active neurons in these neuronal ensembles in response to
666 the stimuli. We also investigated the relationship between the changes as captured by the
667 COMb model and the change in neural variability as measured by Churchland et al. in their
668 famous paper (Churchland et al., 2010).

669 Our overall aim was to investigate some of the challenges in analysing large ensembles
670 of neurons present today. That included collecting the data to analyse (via calcium imaging),
671 and subsequently analysing these data. We felt that this was a worthwhile project because
672 the size of datasets, in terms of numbers of neurons and data collected, is growing rapidly.
673 Consequently these challenges will only become greater unless they are addressed. This is
674 our attempt at addressing them.

675 **Chapter 2**

676 **Sensitivity of the**
677 **spikes-to-fluorescence transform to**
678 **calcium indicator and neuron**
679 **properties**

680 *Abstract*

681 Fluorescent calcium indicators such as GCaMP are widely used to monitor neuronal activity.
682 However the relationship between the fluorescence signal and the underlying action potential
683 firing is poorly understood. This lack of knowledge makes it difficult for experimenters
684 to decide between different indicator variants for a given application. We addressed this
685 problem by studying a basic biophysical model of calcium dynamics in neuronal soma. We
686 fit the model parameters to publicly available data where GCaMP6s fluorescence and whole-
687 cell electrophysiological recordings were made simultaneously in the same single neurons.
688 We systematically varied the model's parameters to characterise the sensitivity of spike train
689 inference algorithms to the calcium indicator's main biophysical properties: binding rate,
690 dissociation rate, and molecular concentration. This model should have two potential uses:
691 experimental researchers may use it to help them select the optimal indicator for their desired
692 experiment; and computational researchers may use it to generate simulated data to aid design
693 of spike inference algorithms.

694 **2.1 Introduction**

695 Although fluorescent calcium indicators such as GCaMP are widely used to monitor neuronal
696 activity, the relationship between the fluorescence signal and the underlying action potential
697 firing is imperfect. The fluorescence signal has a low signal-to-noise ratio, and most indica-
698 tors' kinetics are slow relative to the millisecond-timescale dynamics of the membrane volt-
699 age (example in figure 2.1A). This makes spike inference difficult. Furthermore, the effects
700 of the indicator and cell properties on the fluorescence signal are unknown. For example,
701 genetically encoded indicators can accumulate within neurons over weeks and months (Chen
702 et al., 2013). Studies using calcium-sensitive fluorescent dyes have shown that indicator con-
703 centration has substantial effects on the spike-to-fluorescence relationship (Maravall et al.,
704 2000). Therefore spike rates inferred from GCaMP fluorescence signals may give mislead-
705 ing results if comparing across imaging sessions. More generally, the poor understanding of
706 the spike-to-fluorescence transform means experimenters may not know whether to trust the
707 outputs of spike train inference methods in any given application.

708 Spike trains are usually inferred from the time series of intensity values of one pixel of the
709 fluorescence image, where the pixel is located at the cell's soma. The problems of identifying
710 these pixels, and inferring spikes from their time series can solved separately or together.
711 When attempting to infer spikes, the fluorescence trace is modelled as a linear combination of
712 calcium concentration dynamics, a baseline calcium concentration, and some Gaussian noise.
713 The calcium concentration dynamics are modelled as an autoregressive process of degree 1
714 or 2 with a pulse input corresponding to the spike train, or the number of spikes fired in a
715 time step. The model includes no dynamics for the fluorescent indicator itself. Furthermore,
716 in order to make this model into an easily solvable linear programming problem the number
717 of spikes fired in a timestep is not restricted to non-negative integers but to arbitrary non-
718 negative values (Vogelstein et al., 2010; Pnevmatikakis et al., 2016; Friedrich and Paninski,
719 2016; Pnevmatikakis et al., 2013; Pnevmatikakis et al., 2014). More biologically inspired
720 spike inference models do exist (Deneux et al., 2016), but their fundamentals are very similar.
721 In this work, we investigated the effect of changing dynamics and buffer concentrations on
722 the accuracy of the inference algorithms based on these models.

723 The aim of this project was to model the fluorescence traces produced by a fluorescent
724 calcium indicator in a neuron soma resulting from a specific spike train, given calcium indi-
725 cator parameters such as binding rate, dissociation rate, and molecular concentration. Such

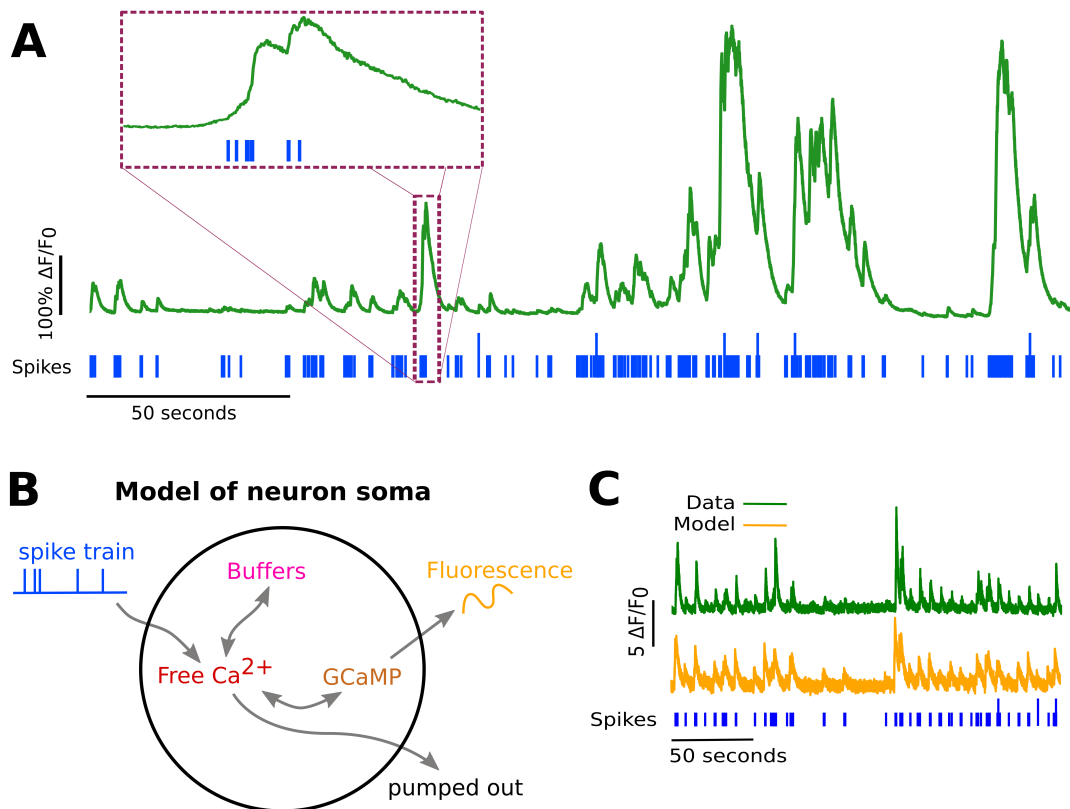


FIGURE 2.1:

- A: Example spike train (blue) and the corresponding GCaMP6s fluorescence trace (green), data replotted from (Berens et al., 2018). Inset shows zoomed section of traces to highlight slow decay of GCaMP6s fluorescence relative to spike time intervals.
- B: Schematic diagram of the neuron calcium and GCaMP computational model.
- C: Good visual match of data fluorescence trace (green) and model simulated fluorescence (orange) in response to an identical spike train (blue).

726 a model would allow benchmarking of various spike inference algorithms, and enable under-
727 standing of how indicator characteristics affect the quality of spike train inference.

728 The model we developed consisted of free calcium, fluorescent indicator molecules, and
729 mobile and immobile endogenous calcium buffers. The indicator molecules which were
730 bound to a calcium molecule could be either excited, i.e. able to release a photon, or relaxed.
731 In order to reproduce the noise inherent in the data collection, we modelled the release of
732 photons from the excited indicator bound calcium as a stochastic process.

733 The fluorescence traces produced by the simulation were calibrated to reproduce the
734 signal-to-noise ratio observed in experimental data. Previously published spike inference
735 algorithms were then used to infer spike trains from the experimental fluorescence traces and
736 the modelled fluorescence traces. The parameters of the model were then varied in order to
737 determine the effect on the system dynamics and the effects on spike inference.

738 2.2 Methods

739 2.2.1 Calcium dynamics model

740 We wrote a biophysical model of the calcium dynamics within a cell soma. When a neuron
741 fires an action potential, voltage-dependent calcium ion-channels open up that allow a current
742 of calcium ions (Ca^{2+}) to flow into the neuron (Koch, 1999). The increase in the free calcium
743 ion concentration inside of the cell, along with changes in the concentration of potassium
744 and sodium, causes the change in cell membrane potential, which must be repolarised. The
745 repolarising process consists of free calcium ions leaving the cell through open ion channels,
746 or binding to molecules within the cell called buffers, or calcium storage by organelles such
747 as the endoplasmic reticulum. A diagram illustrating the cell, its channels, and its buffers
748 can be seen in figure 2.1A. There are several different types of calcium buffer, each with
749 different dynamics and different concentrations within different types of excitable cell. The
750 fluorescent calcium indicator is another calcium buffer, with the useful property that when it
751 is bound to a calcium ion, the bound molecule may become excited by a photon and release
752 a photon in return. This is what creates the fluorescence. After the action potential has taken
753 place, the free calcium concentration within the cell will return to a baseline level (Maravall
754 et al., 2000).

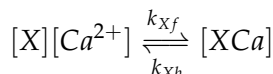
755 We modelled the the dynamics of five molecular concentrations,

- 756 • Free calcium ion concentration, $[\text{Ca}^{2+}]$

2.2. Methods

- 757 • Fluorescent indicator bound calcium, $[BCa]$
- 758 • Endogenous mobile buffer bound calcium, $[ECa]$
- 759 • Endogenous immobile buffer bound calcium, $[ImCa]$
- 760 • Excited buffered calcium, $[BCa^*]$

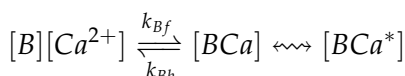
The term ‘buffering’ refers to free calcium ions coming into contact with buffer molecules followed by the binding of those molecules. Diagrammatically:



761 where $[X]$ represents any buffer molecule, and k_{X_f} and k_{X_b} represent the binding (association)
762 and unbinding (dissociation) rates in units of per molar concentration per second (M^{-1}
763 s^{-1}) and per second (s^{-1}) respectively. The speed of this chemical reaction is determined by
764 the binding and unbinding rates.

765 There are a number different endogenous buffers in any neuron. Which buffers are
766 present, and the buffers’ concentrations vary from cell to cell. In order to capture the ef-
767 fects of different kinds of buffers without modelling dozens of different individual buffers,
768 we modelled two different kinds of buffer only. These ‘mobile’ and ‘immobile’ buffers were
769 designed to be aggregations of the effects of multiple different buffers into two effective
770 buffers with different concentrations and binding rates. (Bartol et al., 2015) also divide cal-
771 cium buffers into mobile and immobile varieties. Note that since the model has no spatial
772 component, the mobile and immobile buffers only differ in their binding and unbinding rates.

The fluorescent calcium indicator behaves similarly to the other calcium buffers. The cal-
cium is buffered by the indicator in the same way. But an indicator bound calcium molecule
can become excited by absorbing the energy from a photon. An excited indicator bound
calcium molecule can then release a photon to go back to its ‘relaxed’ state.



773 The released photons are captured by a photon collector. This gives us the fluorescence trace.

774 The system of equations we used to model all of these interactions is as follows:

$$\begin{aligned} \frac{d[Ca^{2+}]}{dt} = & k_{Bb}[BCa] + k_{Eb}[ECa] + k_{Imb}[ImCa] \\ & - k_{Bf}[B][Ca^{2+}] - k_{Ef}[E][Ca^{2+}] - k_{Imf}[Im][Ca^{2+}] \\ & + \beta([Ca_0^{2+}] - [Ca^{2+}]) \end{aligned} \quad (2.1)$$

$$\frac{d[BCa]}{dt} = k_{Bf}[B][Ca^{2+}] - k_{Bb}[BCa] + r[BCa^*] - \eta[BCa] \quad (2.2)$$

$$\frac{d[ECa]}{dt} = k_{Ef}[E][Ca^{2+}] - k_{Eb}[ECa] \quad (2.3)$$

$$\frac{d[ImCa]}{dt} = k_{Imf}[Im][Ca^{2+}] - k_{Imb}[ImCa] \quad (2.4)$$

$$\frac{d[BCa^*]}{dt} = \eta[BCa] - r[BCa^*] \quad (2.5)$$

775 where $[Ca_0^{2+}]$ is the baseline calcium concentration within the cell soma, β is a rate defining
776 how quickly free calcium enters or leaves the cell in the absence of an action potential, η is
777 the excitation rate for indicator bound calcium, r is the photon release rate for the excited
778 indicator bound calcium, and f and b are used to indicate the forward and backward rates
779 for chemical reactions respectively. The excitation rate defines the proportion of indicator
780 bound calcium that becomes excited at each time step. The photon release rate defines the
781 proportion of excited indicator bound calcium that releases a photon and returns to its relaxed
782 state at each time step. An action potential is modelled as a discontinuous increase in the free
783 calcium concentration to an appropriate value (Maravall et al., 2000).

784 Note that each of the three pairs of binding and unbinding terms in the first equation has a
785 corresponding pair in one of the subsequent three equations. Binding removes a free calcium
786 molecule and adds a bound calcium molecule, and unbinding does the opposite.

787 When using this model to simulate a fluorescence trace, the system of equations above are
788 first solved over a period of 25s without action potentials. This lets each of the five tracked
789 chemical concentrations reach their steady state. Then we use the given spike train and the
790 parameters to model the fluorescence trace.

791 Photon release & capture

792 We used a simple model for the photon release. The number of photons released at each time
793 step was controlled by the number of excited indicator bound calcium molecules in the cell

2.2. Methods

794 and a parameter called the ‘release rate’. The release rate is an optimised free parameter of
795 the model.

796 As for the photon capture, in two-photon excitation microscopy the photons scattered
797 by the fluorescent indicator get scattered in all directions. Therefore the number of photons
798 detected is stochastic. This made the process for capturing photons the natural source of
799 noise in the system. The number of photons captured, and therefore the intensity of the
800 fluorescence, is modelled using a binomial distribution. The number of photons released was
801 used as the number of trials. The probability of success, or ‘capture rate’ was a free parameter
802 of the model that we optimised.

803 **2.2.2 Parameter optimisation**

804 The free parameters of the model are as follows:

805 **Calcium rate, β** Controls how quickly the concentration of free calcium will be driven to
806 the baseline concentration.

807 **Capture rate, p** The average proportion of photons captured by the photon detector.

808 **Excitation rate, η** The number of indicator bound calcium molecules that become excited
809 by photon bombardment at each time step.

810 **Release rate, r** The number of excited indicator bound calcium molecules that release a
811 photon at each time step.

812 To optimise the free parameters given a fluorescence trace, we applied the following proce-
813 dure:

814 1. The frequency power spectrum of the trace was measured.

815 2. The power spectrum was smoothed using a boxcar smoother (aka. sliding average, box
816 smoother).

817 3. The log of the smoothed power spectrum was measured.

818 4. Use the model to create a modelled fluorescence trace.

819 5. Apply steps 1, 2, and 3 to the modelled fluorescence trace.

820 6. Calculate the root mean squared difference between the log power of the actual fluo-
821 rescence trace, and the log power of the modelled fluorescence trace.

822 7. Calculate the root mean squared difference between the actual fluorescence trace and
823 the modelled fluorescence trace.

824 8. Use an optimisation algorithm to reapply this process, attempting to minimize the sum
825 of the two root mean squared differences at each iteration.

826 Using the root mean squared difference of the log power spectra as part of the objective
827 function forces the model to match the noise frequency of the actual fluorescence. Using
828 the root mean squared difference of the traces themselves forces the model to match the
829 amplitude of the fluorescence trace more accurately. Using both of these terms as part of our
830 objective function was designed to make our model match the change in $\Delta F / F_0$ in response
831 to an action potential as well as the signal-to-noise ratio of the the actual fluorescence trace.
832 We weighted both of these terms equally.

833 In order to minimise the objective function, a suite of meta-heuristic optimisation (aka.
834 black-box optimisation) algorithms were implemented on each of the traces in the dataset.
835 These methods were chosen because they don't require a gradient for the objective function
836 (gradient-free) and they are particularly useful for minimising stochastic objective functions
837 like the one we used here. The free parameters were optimised for each individual fluores-
838 cence trace. The most successful method for each trace was recorded. The method that was
839 most often successful was probabilistic descent, and the second most successful method was
840 generating set search. Both of these methods are examples of pattern search. These two
841 methods were the best optimisers on about 75% of the traces in the dataset. The other meth-
842 ods were differential evolution (with and without radius limited sampling, adaptive and not
843 adaptive), natural evolution strategy, and random search for comparison.

844 Although this optimisation procedure minimises the value of the optimisation function,
845 the value never reaches zero for a number of reasons. Firstly, the fluorescence traces carry
846 low frequency fluctuations that cannot be captured by the model. Secondly, the model as-
847 sumes that the process of calcium binding to the fluorescent indicator is linear in time (see
848 equation 1), but there are more complicated dynamics involved here. Fluorescent calcium
849 indicators, the GCaMP series for example, are often built upon the calcium binding protein
850 called 'calmodulin'. This protein has four calcium binding sites. These sites are locally split
851 into two pairs. Each pair has a different affinity for calcium, and the affinity of the binding
852 sites is affected by the occupancy of the other binding sites (Kilhoffer et al., 1992). So the
853 calcium to calcium indicator binding process is non-linear, but the model does not take this
854 into account.

2.2. Methods

Parameter	Description	Value	Source
baseline	The baseline concentration of free calcium within the cell soma	$4.5 \times 10^{-8} \text{M}$	(Maravall et al., 2000)
cell radius	The radius of the soma (assumed to be spherical)	10^{-5}M	(Fiala and Harris, 1999)
endogenous	The concentration of endogenous mobile buffer within the cell soma	10^{-4}M	(Faas et al., 2011)
frequency	The frequency at which the spike trains are sampled.	100Hz	
immobile	The concentration of endogenous immobile buffer within the cell soma	$7.87 \times 10^{-5} \text{M}$	(Bartol et al., 2015)
indicator	The concentration of fluorescent indicator within the cell soma	10^{-4}M	(Maravall et al., 2000)
k_{Bb}	The unbinding rate of the fluorescent calcium indicator	160s^{-1}	(Bartol et al., 2015)
k_{Bf}	The binding rate of the fluorescent calcium indicator	$7.77 \times 10^8 \text{s}^{-1} \text{M}^{-1}$	(Bartol et al., 2015)
k_{Eb}	The unbinding rate of the endogenous mobile buffer	10^4s^{-1}	(Bartol et al., 2015)
k_{ef}	The binding rate of the endogenous mobile buffer	$10^8 \text{s}^{-1} \text{M}^{-1}$	(Bartol et al., 2015)
k_{Imb}	The unbinding rate of the endogenous immobile buffer	524s^{-1}	(Bartol et al., 2015)
k_{Imf}	The binding rate of the endogenous immobile buffer	$2.47 \times 10^8 \text{s}^{-1} \text{M}^{-1}$	(Bartol et al., 2015)
peak	The increase in free calcium concentration within the cell induced by an action potential	$2.9 \times 10^{-7} \text{M}$	(Maravall et al., 2000)

TABLE 2.1: **Fixed parameters** A table of the parameters fixed before optimising the model. The values of these parameters could be changed to model different fluorescent calcium indicators.

855 **Fixed parameters**

856 As well as the optimised parameters mentioned in section 2.2.2, the model also has thirteen
 857 fixed parameters. Please see table 2.1 for details of these parameters and their values. In
 858 an application of the model, these parameters can be changed in order to model any given
 859 fluorescent calcium indicator, or even prospective indicators that only exist in theory.

860 **2.2.3 Julia**

861 The programming language used to write and execute the model was ‘Julia’. Julia is a dy-
 862 namic programming language designed for technical computing. Julia was designed specif-
 863 ically to provide a convenient high-level dynamic language similar to MATLAB, or Python,
 864 with improved performance. Julia’s type system and Julia’s direct interfaces with C and

865 Fortran allow this aim to be achieved (Bezanson et al., 2012). The Julia version of the
866 ‘Sundials’ package for ODE solving was used to solve the system of equations above. The
867 BlackBoxOptim.jl package for Julia was used to perform the optimisation.

868 **2.2.4 Spike inference**

869 We used spike inference algorithms to compare the quality of spike inference using the mod-
870 elled traces to the quality of spike inference using the observed traces. We also used the
871 spike inference algorithms to assess the effect of parameter perturbation on the spike infer-
872 ence. Three algorithms were used:

873 **Constrained non-negative matrix deconvolution algorithm (aka CNMD algorithm)** The
874 underlying model models the fluorescence as a linear combination of a calcium trace
875 with additional noise. This calcium trace is a first order autoregression with a pulse
876 input to represent action potentials. This algorithm uses a constrained version of non-
877 negative Weiner deconvolution to infer a calcium signal and a ‘spiking activity signal’
878 from the fluorescence trace (Vogelstein et al., 2010; Pnevmatikakis et al., 2016). The
879 spiking activity signal is a non-negative vector of real numbers reflecting the cell’s
880 activity rather than an actual spike train.

881 The underlying model of the fluorescence trace used by this algorithm requires 5 pa-
882 rameters that are calculated from the data: the standard deviation of the white noise
883 component of the trace, the decay time constant, the order of the autoregressive model,
884 baseline calcium concentration (or equivalently, baseline fluorescence), and the initial
885 calcium concentration (or equivalently, initial fluorescence).

886 The standard deviation of the noise was estimated by calculating the power spectral
887 density of the fluorescence trace, then taking the exponent of the mean of the log of
888 the density across the frequency range between 0.25 and 0.5 times the Nyquist rate
889 for the fluorescence trace. The time constant of the fluorescence trace was estimated
890 from the autocovariance of the denoised fluorescence trace. If a stable autoregressive
891 model could not be found at the default order for the autoregression ($p = 2$), the order
892 was increased by one, and the decay time constant was re-estimated. If a value was
893 not provided for the baseline concentration and initial concentration they were both
894 assumed to be 0. We did not provide values for these parameters.

2.2. Methods

We inferred a spike train by choosing an optimised threshold for the spiking activity signal. Whenever the spiking activity signal exceeded that threshold, an action potential was inferred. The threshold was optimised by minimising the difference between the number of spikes in the ground truth spike train and the number of spikes predicted. This kind of calibration gives the algorithm an advantage when predicting the correct number of spikes, but not the timing of those spikes. Because of this, comparisons in performance between different spike inference algorithms are not valid. However, comparisons between the performance of this algorithm applied to different fluorescence traces are still valid.

MLSpike algorithm Deneux et al. (2016) developed two different calcium fluorescence models behind their spike inference algorithm (MLspike) with a more biological inspiration. For their simpler model, they take a physiological approach and account for baseline calcium indicator dynamics. They end up with a system of first order differential equations defining the dynamics of calcium concentration, baseline fluorescence, and fluorescence. For their more complicated model specifically for genetically encoded calcium indicators, they also took into account indicator binding and unbinding rates, which added another equation to their system of equations. This algorithm uses a generalised version of the Viterbi algorithm to return the spike train that maximises the likelihood of producing the given fluorescence trace. The Viterbi algorithm is an algorithm for estimating the most likely sequence of hidden states resulting in a sequence of observed states in a discrete-time finite-state Markov process (Forney, 1973). In this case, each hidden state is defined by the presence or absence of an action potential, and each observed state is the value of the fluorescence trace at each time step. (Deneux et al., 2016).

We used the autocalibration algorithm provided with this spike inference algorithm to estimate values for the standard deviation of the white noise in the fluorescence trace, the increase in fluorescence in response to an action potential, and the decay time constant of the fluorescence trace. The standard deviation of the noise in the trace was estimated as the mean of power spectral density of the trace in the frequency range between 3 and 20Hz. The authors of this algorithm believed that the frequencies lower than this range will contain information about the calcium dynamics, while the frequencies above this range contain correlated noise and are therefore unsuitable for estimating white noise.

927 The increase in fluorescence in response to an action potential and the decay time con-
928 stant were estimated in parallel. Firstly, a ‘calcium events’ trace was extracted from the
929 fluorescence trace using a modified version of the spike inference algorithm with fixed
930 values for the increase in calcium in response to a calcium event and decay time con-
931 stant. The temporally isolated calcium events with moderate amplitudes ($\Delta F/F \leq .25$)
932 were extracted, and the other events were removed. The idea here was to extract a
933 trace of the calcium concentration produced by isolated groups of action potentials.
934 The event amplitude and the time decay constant were then estimated from this trace
935 of ‘good’ events. Next, a histogram of the event amplitudes was constructed. An
936 estimate of the number of spikes in each event was estimated from the peaks of this
937 histogram. A number of spikes was then assigned to each calcium event based on this
938 estimate. Finally, the autocalibrated values for the change in fluorescence and the decay
939 time constant were calculated by fitting to the modified calcium event trace.

940 Many values that may be influential in the autocalibration process were hard-coded by
941 the authors of the algorithm. Particularly, defining ‘moderate’ calcium events as those
942 that produce $\Delta F/F \leq .25$ may be suitable for indicators with lower signal-to-noise
943 ratios than GCaMP6s. This could be the reason for this algorithm’s poor performance
944 in our application (see Results section 2.3.2).

945 The poor performance in comparison to the other two algorithms could also be down
946 to the other algorithms being calibrated to match the number of spikes in the ground
947 truth spike trains.

948 **Online Active Set method to Infer Spikes (OASIS)** This algorithm is once again based on
949 an auto-regressive model of the fluorescence trace, but can be generalised to any or-
950 der. Both the first and second order versions can be fit to a spike train in a reasonable
951 time. The algorithm itself is a generalisation of the pool adjacent violators algorithm
952 (PAVA) that is used in isotonic regression. The OASIS algorithm works through the
953 fluorescence trace from beginning to end, this combined with the speed of the algo-
954 rithm means that it could be used for real-time online spike inference (Friedrich and
955 Paninski, 2016).

956 This algorithm required the standard deviation of the noise component of the fluo-
957 rescence trace and the fluorescence trace decay time constant to be estimated. The
958 standard deviation of the noise was estimated by calculating the power spectral den-
959 sity of the fluorescence trace, then taking the mean of the density across the frequency

2.2. Methods

range between 0.25 and 0.5 times the Nyquist rate for the fluorescence trace. These frequencies were judged to be most likely to contain uncorrelated noise, rather than signal or correlated noise, by the developers of the algorithm. The time constant of the fluorescence trace was estimated from the autocovariance of the denoised fluorescence trace. In practice, we used the `estimate_parameters` function provided by the authors of this algorithm to estimate these parameters.

This algorithm also required one more parameter, a constant that indicated the minimal non-zero activity within a bin in order for a spike to be assigned to that bin. When applying the algorithm, we used 10 different values for this parameter, and counted the total number of spikes inferred by the algorithm each time. We then chose the value that gave the smallest difference between the total number of inferred spikes and the total number of actual spikes. Calibrating the algorithm in this way gives the algorithm an advantage for inferring the number spikes, but not for inferring the timing of the spikes. This kind of calibration makes the results of the different algorithms incomparable, but the results from the same algorithm applied to different fluorescence traces are still comparable.

In order to quantify the quality of spike inference for a given algorithm, we ran that algorithm on all of the fluorescence traces in dataset number eight of the spike finder datasets. These datasets contained fluorescence traces from neurons containing a fluorescent calcium indicator (either OGB-1 or GCaMP6s) and spike trains from those cells simultaneously recorded using loose-patch electrophysiological recordings. This provided us with a *ground-truth* for spike inference from the fluorescence traces. Then we measured some binary classification measures on the results. These measures included

- Accuracy
- True positive rate (aka recall, sensitivity, hit rate)
- True negative rate (aka specificity)
- Precision
- Negative predicted value
- False negative rate (aka miss rate)
- False positive rate (aka fall-out)

990 ● False discovery rate

991 ● False omission rate

992 In making these measurements, we allowed a tolerance of two subsequent time bins for spike
993 prediction. For example, the spike train data is a vector of 0s and 1s, with one element
994 for each time bin, and time bin being 10ms. A ‘0’ denotes inactivity, a ‘1’ denotes the
995 presence of at least one action potential. The inferred spike trains produced by the spike
996 inference algorithms take the same form. In our analysis, if a spike appeared in the inferred
997 spike train up to two time frames after a spike in the observed spike train, that spike was
998 considered correctly inferred i.e. a true positive. However, once a spike in the inferred
999 spike train was matched to a spike from the observed spike train, the inferred spike could
1000 not be matched to another observed spike. To illustrate, if two spikes were inferred in the
1001 two time bins following an isolated observed spike, the first inferred spike was considered
1002 correctly inferred, but the second inferred spike was considered incorrectly inferred, i.e. a
1003 false positive.

1004 The most useful measure was the true positive rate. This is because the spiking is sparse
1005 and this measurement is sensitive to the number of spikes observed and inferred, but is not
1006 affected by the true negative or false negative rates. After optimising the parameters for each
1007 fluorescence trace we measured the spike inference quality for the observed fluorescence
1008 traces, and compared this to the spike inference quality for the modelled traces.

1009 When measuring the spike inference quality for higher frequency spike train (1 – 10Hz),
1010 we used the accuracy as our binary classification measure. At these frequencies the variance
1011 of the fluorescence trace was much higher than for sparser spiking regimes, therefore we
1012 wanted to take into account the number of false negatives inferred by the algorithm.

1013 **Comparing spike inference quality**

1014 In order to compare spike inference quality we had to use methods for comparing samples.
1015 When comparing the true positive rate distributions arising from two different datasets, or
1016 two different algorithms on the same dataset, we compared the distributions using a paired
1017 t-test.

1018 **2.2.5 Perturbation analysis**

1019 In order to measure the sensitivity of spike inference to changes in a given model parameter,
1020 we perturbed the parameter and compared the quality of spike inference with the perturbed

2.3. Results

parameters to the quality of spike inference with the experimental or optimised parameters. In order to maximise the possibility of observing a difference due to the perturbation, we perturbed the chosen parameter by a relatively large amount. For example, the experimental value for the molar concentration of the fluorescent indicator within the cell was 10^{-4}M (Maravall et al., 2000). The perturbed values used for this parameter were 10^{-2}M , 10^{-3}M , 10^{-5}M , and 10^{-6}M . The quality of the inference was compared by measuring the true positive rate for each perturbed value and using a t-test to compare the distributions of the results.

2.2.6 Signal-to-noise ratio

To assess the effect of perturbation on the modelled traces, we measured and compared the signal to noise ratio (SNR) on each of the modelled traces. We calculated the SNR as the peak change in fluorescence divided by the standard deviation of the baseline fluctuation of the fluorescence trace (Tada et al., 2014). We measured these values by running the model on a spike train consisting a long period of inactivity followed by one action potential. We ran the model on this spike train one hundred times. We then measured the mean change in fluorescence and standard deviation of baseline activity across the one hundred modelled fluorescence traces, and calculated the SNR.

2.2.7 Data sources

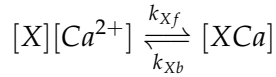
All of the data used in this project was sourced from the ‘Spike Finder’ project (spikefinder.codeneuro.org). The data consisted of a collection of datasets with simultaneously measured fluorescence traces and action potentials (Berens et al., 2018).

2.3 Results

2.3.1 A biophysical computational model can generate accurate fluorescence traces from spike trains

To study the relationship between action potential firing and calcium fluorescence, we built a computational model of calcium dynamics in a neuronal soma. The model consisted of four dynamic variables: the concentration of free calcium, two types of endogenous buffer, and the calcium-sensitive fluorescent indicator. Each of the buffers and the indicator could

independently bind and unbind with calcium. These reactions were modelled as



where X is the buffer concentration and Ca^{2+} is the calcium concentration. Each species could therefore exist in two states: either bound with calcium or unbound. To model the imaging process, we also added a third, excited state to the indicator. When in the calcium-bound state, the indicator could be converted to an excited state, corresponding to the absorption of a photon. The rate of this excitation process could be interpreted as the intensity of the light illuminating the sample. Once excited, the species decayed back to the unexcited state at a fixed rate, corresponding to the spontaneous emission of photons. The total emitted fluorescence signal was interpreted as proportional to this de-excitation flux. To represent experimental noise in the photon capture process, we drew a random number of captured photons at each time step from a binomial distribution, parameterised by a number p that corresponds to the mean fraction of released photons that are captured.

The model had 17 parameters in total describing the molecules' concentrations and reaction rates (Methods). We set 13 of these parameters to values from the literature. The remaining 4 parameter values we fit to publicly-available data (Berens et al., 2018), briefly explained as follows (see Methods for full details). Single neurons from acute rat cortical slices expressing GCaMP6s were imaged with two-photon microscopy while the membrane potentials of the somata of the same neurons were simultaneously recorded via whole-cell patch clamp electrophysiology. In this dataset, the electrical recordings give unambiguous information about neurons' spike times. To do the parameter fitting, we feed these spike trains as inputs to the computational model. After running, the model returns a simulated fluorescence trace. We aimed to find the model parameter values that give the best match between this simulated fluorescence trace and the real fluorescence time series recorded in the corresponding neuron. To do this we used a suite of optimisation procedures to jointly fit both the real neuron's fluorescence time series and power spectrum, which capture complementary information about the spikes-to-fluorescence mapping (Methods). We performed the fitting procedure independently for each of the 20 neurons in the spikefinder dataset (<http://spikefinder.org>). After fitting, the model produced realistic-looking fluorescence time series (Figure 2.1).

Given that fluorescence traces are often modelling using a linear combination of a first degree autoregressive process and white noise, it could be argued that a four parameter model

2.3. Results

1074 contains some redundancy in the parameter space. But, our aim was to create a biophysical
1075 model that could be useful for interpreting the role of cell dynamics behind the production of
1076 the fluorescence trace. Because of that we felt that our redundancy was justified.

1077 2.3.2 Spike inference algorithms perform similarly on real data compared with 1078 time series simulated from the model

1079 Researchers often pass the fluorescence time series through a spike inference tool before per-
1080 forming further statistical analyses. These spike inference algorithms take the fluorescence
1081 trace as input and attempt to estimate the neuronal spike train that triggered them (Vogelstein
1082 et al., 2010; Pnevmatikakis et al., 2016; Friedrich and Paninski, 2016; Pnevmatikakis et al.,
1083 2013; Pnevmatikakis et al., 2014; Deneux et al., 2016). Part of our motivation for building
1084 this model was to allow us to investigate which properties of the cell and the calcium indi-
1085 cator affect the quality of spike inference? In order to trust the conclusions from our model,
1086 we should first be confident that spike inference from our simulated fluorescence traces is
1087 similar to that from the real data. To test this we passed each of the simulated fluorescence
1088 traces through three previously published spike inference algorithms, quantified their perfor-
1089 mance against the ground-truth electrophysiology data, repeated the procedure for the real
1090 calcium fluorescence time series, and compared the accuracy of the inference processes in
1091 all cases. The *true positive rate*, also known as the *recall*, the *sensitivity*, or the *probabil-
1092 ity of detection* of spike inference varied across the three inference algorithms we tried (p
1093 value and statistical test here). The constrained non-negative matrix deconvolution algorithm
1094 (Pnevmatikakis et al., 2016) (CNMD algorithm) correctly detected approximately 45% of the
1095 true spikes, the OASIS algorithm (Friedrich and Paninski, 2016) correctly detected approx-
1096 imately 35% of the true spikes, and the ML spike algorithm (Deneux et al., 2016) correctly
1097 detected approximately 15% of the true spikes (see figure 2.2). Notably, for two of the three
1098 inference algorithms, the quality of inference was also fairly consistent for individual spike
1099 trains, not just the group means ($p > 0.05$, paired t-test). This demonstrates that the models
1100 were generating fluorescence time series that were similarly difficult to decode as the real
1101 data, in ways that were not specific to any one inference algorithm. This is evidence that the
1102 models captured real aspects of the spikes-to-fluorescence transform.

1103 2.3.3 Relative effects of various buffers to the fluorescence signal

1104 One of the benefits of computational models over laboratory experiments is that we can
1105 observe all the variables in the simulation to gain insight into the system's dynamics, which

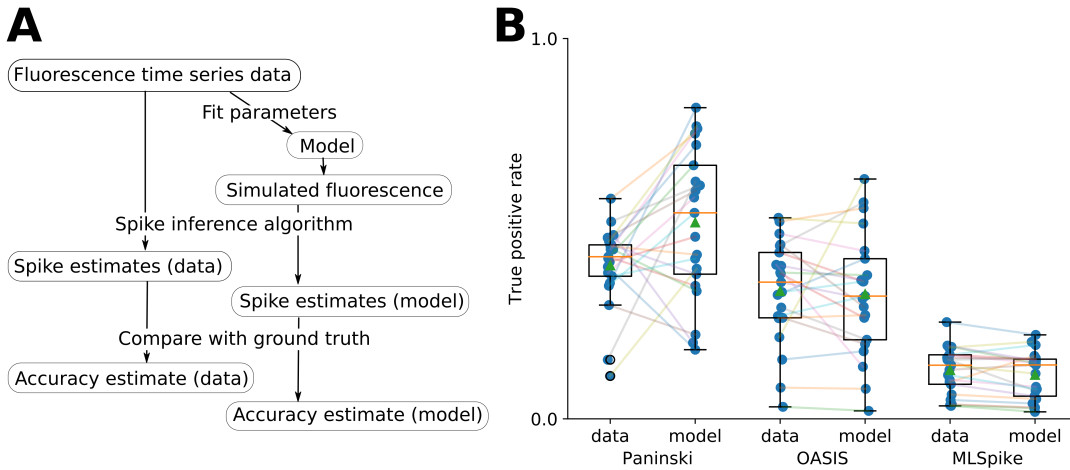


FIGURE 2.2:
A: Workflow to compare spike inference for real versus simulated fluorescence data.

B: True positive rates achieved by three different spike inference algorithms when applied to observed spike trains, and simulated spike trains. Data points overlaid as blue circles. The performance is similar from real and simulated data for each of the algorithms.

quantities

1106 can be difficult to do in the lab. We plotted the concentrations of the various species over
 1107 time for a version of the model fit to one data set, in response to the same train of spikes used
 1108 for fitting (figure 2.3). Figure 2.3a shows the absolute values of the species concentrations,
 1109 summed. Consistent with experimental estimates (Maravall et al., 2000), only a small fraction
 1110 ($\sim 0.1\%$) of calcium is free and unbound to any buffer. Of the bound calcium, the vast
 1111 majority, ($\sim 96\%$) is bound to the GCaMP indicator. The two types of endogenous buffer
 1112 are bound to the remaining calcium ($\sim 4\%$). An influx of calcium from a single spike adds
 1113 very little to the total calcium, in relative terms (red line in Figure 3a).

1114 When calcium entered the model neuron it was rapidly buffered (Bartol et al., 2015).
 1115 However the relative fractions of which buffer molecules bound to the influxed calcium was
 1116 dynamic, and changed over time. Figure 2.3 (b-f) shows the time course of the various species
 1117 over time in response to a calcium influx event from a single action potential. Crucially,
 1118 the indicator $[BCa]$ competed with the endogenous buffers $[ImCa]$ and $[ECa]$ – all three
 1119 bind calcium on similar timescales. This implies that the timescale and amplitude of the
 1120 $[BCa]$ variable will also depend on the binding rates and availabilities of the endogenous
 1121 buffers. For example if we decreased the concentration of an endogenous buffer, we might
 1122 expect both a faster rise time and greater peak amplitude of the $[BCa]$ signal in response to
 1123 a calcium influx event. The slowest component of the decay had a similar time constant for
 1124 $[BCa]$, $[ImCa]$ and $[ECa]$, which in turn matched the $[Ca]$ extrusion time constant in our

2.3. Results

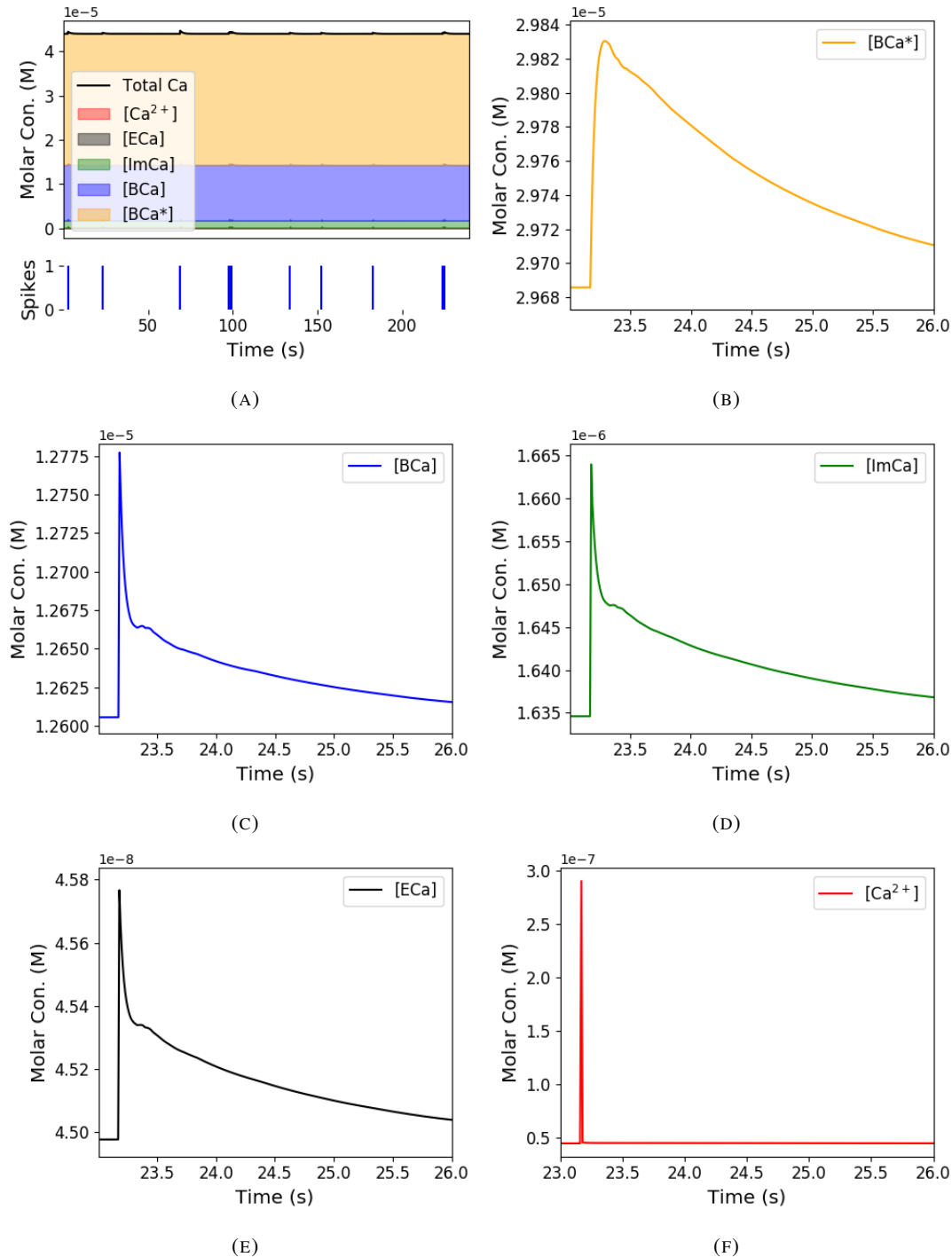


FIGURE 2.3: Calcium Buffering Dynamics (A) The proportions of bound and free calcium concentrations within a cell, with the associated spike train. (B)-(F) The dynamics of the concentration of (B) excited indicator bound calcium, (C) indicator bound calcium, (D) immobile endogenous buffer bound calcium, (E) mobile endogenous buffer bound calcium, and (F) free calcium in response to an action potential at ~ 23.2 s.

model ($\sim 6.29 \times 10^{-22} \text{Ms}^{-1}$). This implies that the buffers and the indicator had reached a dynamic equilibrium and were jointly tracking the free calcium concentration as calcium was slowly extruded from the cell.

Interestingly the excited bound calcium species ($[BCa^*]$) showed a qualitatively different timecourse in response to a calcium influx event. This concentration is subject to the added ‘excitation and release’ dynamic, where a certain proportion of the concentration absorbs the energy from an incoming photon and goes into an ‘excited state’ at each time step. A certain proportion of the concentration releases a photon and reverts to a ‘relaxed state’ at each timestep also. This means that the excited bound calcium lags behind the bound calcium trace. We could think of the excited bound calcium trace as a low pass filtered version of the bound calcium trace.

2.3.4 Spike inference accuracy is sensitive to indicator properties, and likely varies within and between cells

The above results imply that the fluorescence signal depends on the relative properties of both GCaMP and the endogenous buffers. We next used the model to directly ask how sensitive spike inference was to these components. We focused on three key parameters that likely vary from cell to cell and experiment to experiment: GCaMP binding kinetics, GCaMP concentration, and endogenous buffer concentration.

Several variants of GCaMP itself have been made that differ in calcium binding kinetics, baseline fluorescence, fluorescence efficiency, and other factors. For example, GCaMP6f has a decay time constant of $\sim 1\text{s}$, while GCaMP6s has a decay time constant of $\sim 2\text{s}$ (Chen et al., 2013). Here we asked how these differences in binding kinetics affect spike inference. We jointly varied the calcium binding and unbinding rates of the indicator by the same factor over a range from 100-fold slower to 100-fold faster from the fitted values, and simulated the fluorescence response for each of the parameter settings in response to the same spike trains as before (figure 2.4). Notably this manipulation does not affect the indicators affinity, and therefore would not affect steady-state responses to prolonged changes in calcium. Instead it is likely to affect its sensitivity to the spike train dynamics. We computed two summary measures from the simulated fluorescence traces: the signal-to-noise ratio for a single spike (Methods, section 2.2.6), and the accuracy of spike inference for each of the spike trains. We observed a reduction in the signal-to-noise ratio and the spike inference quality when we set the binding and unbinding rates to one hundredth of their fitted values, and to one tenth of their fitted values. When we increased the value of both binding rates, we observed

2.3. Results

no change in these measurements. The reduction in both rates lead to smaller increases in fluorescence in response to an action potential and a longer decay time (figure 2.4a), this caused the reduction in signal-to-noise ratio. As both rates were increased, the change in $\Delta F/F_0$ in response to an action potential increased and the decay time decreased slightly, but the fluorescence trace created by these values was very similar to the trace created by the fitted values.

Second, the overall concentrations of GCaMP often varies from cell to cell. For example different cells, even of the same type in the same tissue, can express different levels of GCaMP, due to proximity to the infection site, or the cell becoming ‘nuclear-filled’ (Tian et al., 2009; Chen et al., 2013). Also, GCaMP is often used for longitudinal experiments where the same cells are re-imaged across multiple days or weeks. However since GCaMP expression typically ramps up over time (Chen et al., 2013), the accuracy of spike inference may differ across multiple longitudinal recordings in the same cell. We addressed this by varying the concentration of calcium indicator in the model, simulating spike trains and measuring signal-to-noise ratio and spike inference accuracy on the resulting fluorescence traces. Both increasing and decreasing the concentration of the indicator had effects on the fluorescence trace, signal-to-noise ratio, and spike inference. The signal-to-noise ratio and spike inference quality decreased with decreased indicator concentration, and both showed a decrease when the indicator concentration was increased to 100 times its fitted value (figure 2.5). The signal-to-noise ratio showed an increase when the indicator concentration was increased to 10 times its fitted value, but there was no corresponding change in the spike inference quality. The decrease in indicator concentration caused a reduction in the increase in $\Delta F/F_0$ in response to an action potential, and an increase in the decay time of this increase (figure 2.5a). The increase in indicator concentration had the opposite effect, it caused an increase in the change in $\Delta F/F_0$ in response to an action potential, and a decrease in the decay time.

Third, the concentration and types of endogenous calcium buffers also vary from neuron to neuron, both within and between cell types (Bartol et al., 2015; Maravall et al., 2000; Neher and Augustine, 1992). Since the calcium buffer capacity of neurons is high, around 50-70 (Lee et al., 2000) in excitatory hippocampal pyramidal cells, around 100-250 (Lee et al., 2000) in inhibitory hippocampal pyramidal cells, and 900-200 in Purkinje cells (depending on the age of the subject), these endogenous buffers compete with GCaMP for binding to calcium, and variations in endogenous buffer concentration may affect GCaMP signal and therefore spike inference. To address this we varied the concentration of the endogenous buffer in the model neuron over five orders of magnitude from 0.8 to 8000 μM , simulated

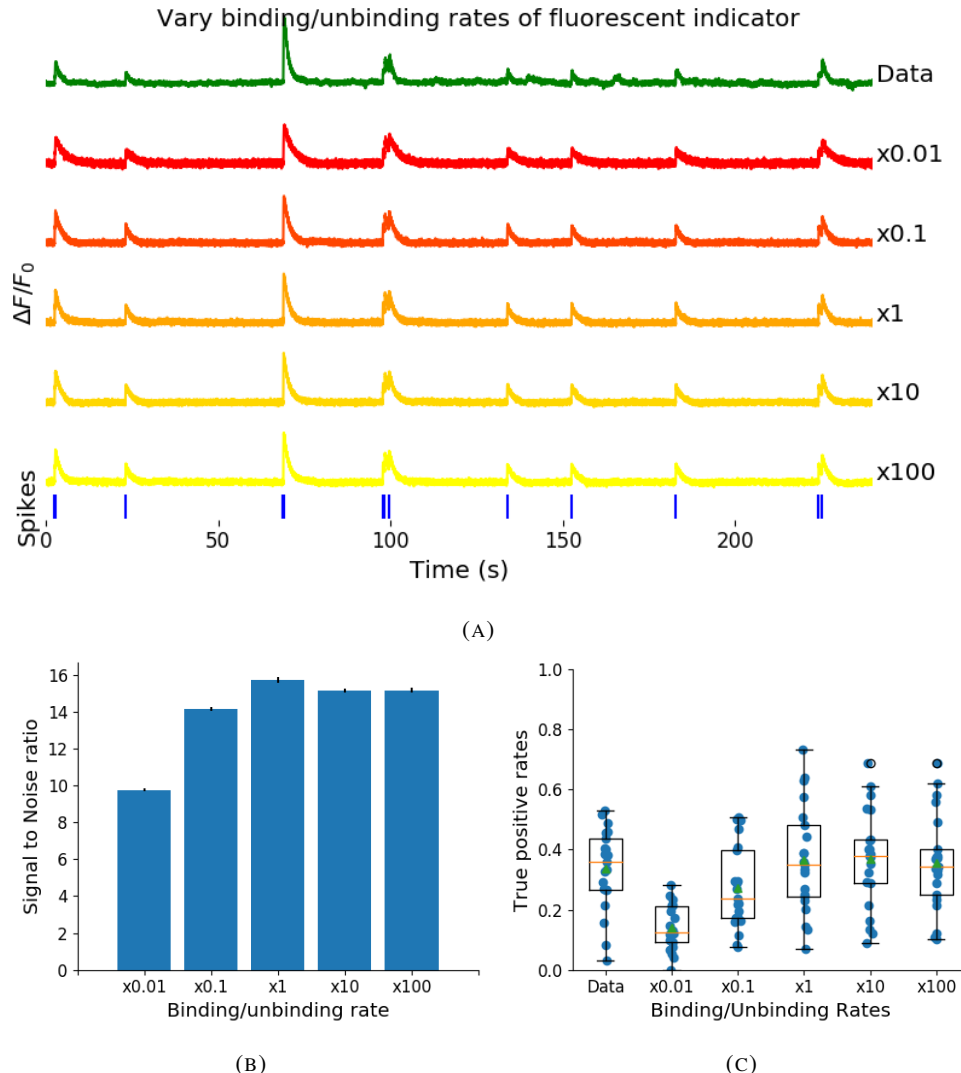


FIGURE 2.4: (A) An example trace for each of the five pairs of values used for the binding and unbinding rates of the fluorescent calcium indicator. (B) The signal-to-noise ratio of the modelled fluorescence traces using each of the four perturbed value pairs, and the experimental value. The SNRs for the value pairs perturbed downward are lower than that for the unperturbed value pair or the higher value pairs. (C) The true-positive rates of the deconvolution algorithm's predictions when inferring from the observed data, and inferring from modelled traces using the perturbed and experimental values. We used the OASIS algorithm for spike inference here. The results from the other spike inference methods were similar, with their true positive rates scales similarly to figure 2.2 B.

2.3. Results

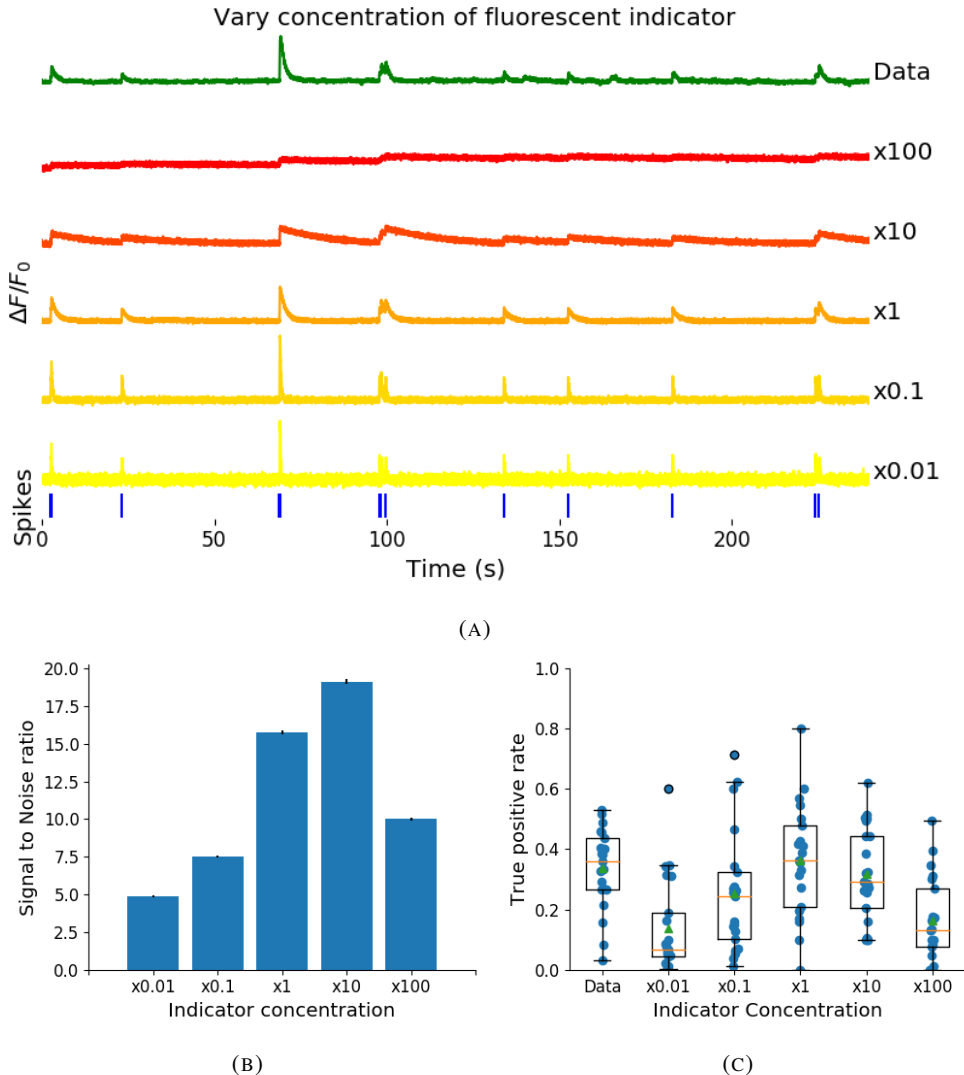


FIGURE 2.5: (A) An example trace for each of the five perturbed values for the concentration of fluorescent calcium indicator. The top two traces are produced by the lower perturbed values, the middle trace is produced by the experimental value, and the lowest two traces are produced when using the higher perturbed values. (B) The signal-to-noise ratio of the modelled fluorescence traces using each of the four perturbed values, and the experimental value. Extreme perturbations of the concentration either above or below the experimental level lowered the SNR. (C) The true-positive rates of the deconvolution algorithm's predictions when inferring from the observed data, and inferring from modelled traces using the perturbed and experimental values. We found that the algorithms performs equally badly on the two most extreme values, and performs equally well on the experimental value, and the next higher perturbed value. We used the OASIS algorithm for spike inference here. The results from the other spike inference methods were similar, with their true positive rates scales similarly to figure 2.2 B.

1192 calcium fluorescence traces in response to the same set of spike trains, and performed spike
1193 inference on the resulting fluorescence time series. Increasing the endogenous buffer con-
1194 centration had a substantial effect on the GCaMP fluorescence signal, both decreasing its
1195 amplitude and slowing its kinetics (figure 2.6(a)). This corresponded with a decrease in both
1196 single-spike signal-to-noise ratio (figure 2.6(b)) and spike inference accuracy (figure 2.6(c)).
1197 In contrast, decreasing endogenous buffer capacity from the fitted value had little effect on
1198 either the GCaMP signal or spike inference (figure 2.6).

1199 **2.3.5 Single spike inference accuracy drops for high firing rates, but firing rate
1200 itself can be estimated from mean fluorescence amplitude**

1201 The fluorescence signal recorded from neurons using calcium indicators is typically much
1202 slower than changes in membrane potential for two reasons: first, because the calcium and
1203 the indicator have slow binding and unbinding kinetics, the signal is a low-pass filtered ver-
1204 sion of the membrane potential. Second, neuronal two-photon imaging experiments are often
1205 performed in scanning mode, which limits their frame rate to $\sim 10\text{Hz}$ or slower. This im-
1206 plies that multiple spike events that occur close in time might be difficult to resolve from a
1207 calcium indicator time series. Many cells, especially several types of inhibitory interneurons,
1208 fire tonically at rates higher than 10Hz. We used the model to test whether spike inference
1209 accuracy depended on the neuron's firing frequency by driving the cell with spike trains sam-
1210 pled from a Poisson processes of varying frequency. We simulated a variable firing rate using
1211 an Ornstein-Uhlenbeck process, and simulated the spike trains using a Poisson distribution
1212 with its rate taken from this process. Because of the high frequency firing rate of these spike
1213 trains, we used the accuracy as the measure of spike inference quality. We simulated 30
1214 spike trains at average firing rate of 1, 5, and 10Hz, and measured the spike inference quality
1215 of all these traces. Spike inference accuracy decreased with increasing firing rate, for up to
1216 10Hz Poisson spike trains (figure 2.8(left)). Although the accuracy remained above 90% for
1217 each of the three frequencies. We also plotted the average $\Delta F / F_0$ as a function of stimula-
1218 tion firing rate. We found that it increased monotonically as a function of firing rate (figure
1219 2.8(right)).

1220 We expected lower spike inference quality as the average spiking frequency increased.
1221 Since the fluorescence trace, in some sense, is a low pass filtered version of the spike train, a
1222 tightly packed groups of spikes will be more difficult to infer than isolated spikes. However,
1223 the increasing amplitude of the fluorescence trace with increasing frequency suggests that
1224 some spike inference algorithm could be developed based on this amplitude.

2.3. Results

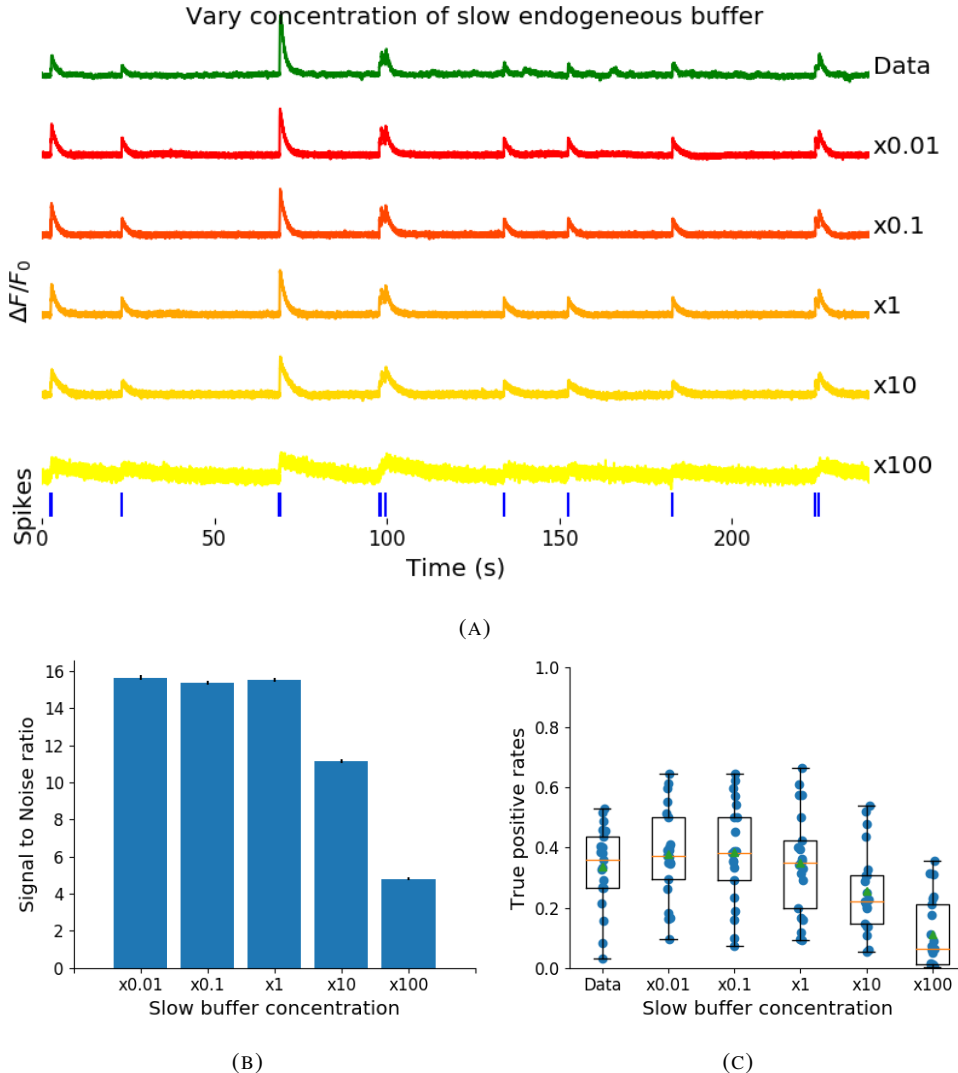


FIGURE 2.6: (A) An example trace for each of the five perturbed values for the concentration of immobile endogenous buffer. (B) The signal-to-noise ratio of the modelled fluorescence traces using each of the four perturbed values, and the experimental value. The lower values for the immobile buffer produce the same SNR as the experimental value. But the higher perturbed values produce fluorescence traces with a lower SNR. (C) The true-positive rates of the deconvolution algorithm's predictions when inferring from the observed data, and inferring from modelled traces using the perturbed and experimental values. We used the OASIS algorithm for spike inference here. The results from the other spike inference methods were similar, with their true positive rates scales similarly to figure 2.2 B.

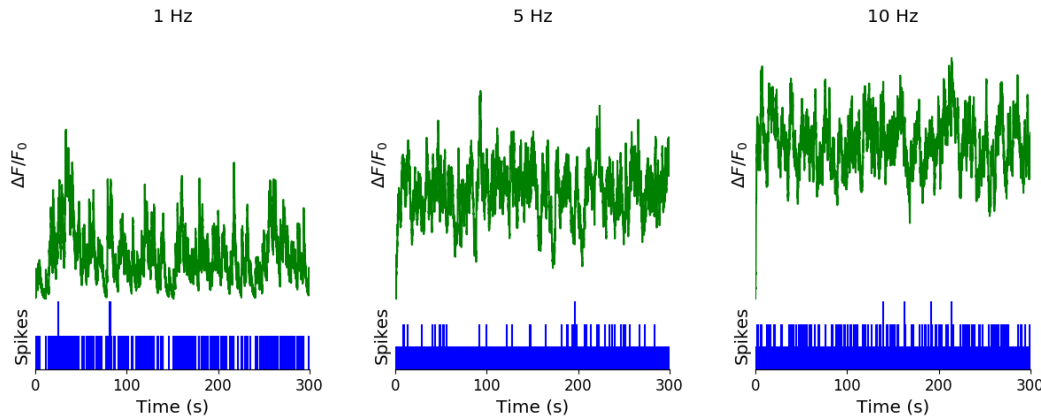


FIGURE 2.7: Simulating fluorescence traces at different firing rates Example modelled traces created using simulated spike trains with a mean firing rate of 1Hz (left column), 5Hz (middle column), and 10Hz (right column). Note the difference in amplitude with different mean firing rates.

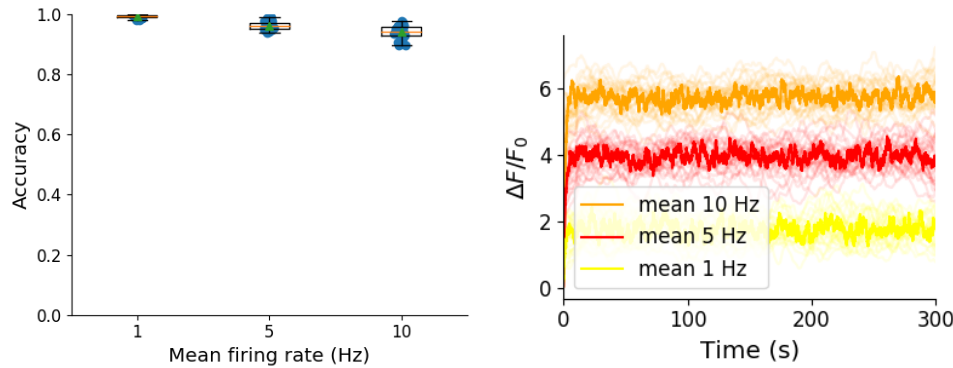


FIGURE 2.8: Inference quality and $\Delta F/F_0$ vs Firing rate (left) The spike inference accuracy when applied to 30 traces created using simulated spike trains with mean firing rates of 1, 5, and 10 Hz. (right) The mean $\Delta F/F_0$ across those 30 traces for each frequency.

1225 2.4 Discussion

1226 We designed a biophysical model for the changes in free calcium and bound calcium con-
 1227 centrations within a cell soma with a fluorescent calcium indicator. We used this model to
 1228 model the fluorescence trace resulting from a spike train in this cell. We fit the free parame-
 1229 terers of the model by matching the power spectrum and amplitude of fluorescence traces with
 1230 simultaneously measured spike trains. We inferred spikes from real fluorescence traces and
 1231 modelled fluorescence traces, and measured the quality of the spike inference in both cases.
 1232 We found that the spike inference quality was similar in both cases. We perturbed the concen-
 1233 tration of the calcium buffers in the model, and the binding/unbinding rates of those buffers
 1234 in the model, and measured the effect on the signal-to-noise ratio (SNR) of the modelled
 1235 fluorescence traces and the spike inference quality.

2.4. Discussion

1236 For the fluorescent calcium indicator, we found that any large perturbation away from the
1237 value taken from the literature led to a reduction in SNR, and spike inference quality. For
1238 the binding/unbinding rates, we kept the ratio of these rates constant, but altered their values
1239 in parallel. The lower values caused a reduction in SNR, and a reduction in spike inference
1240 quality. For the endogenous buffer concentration, an increase above the experimental value
1241 caused a reduction in SNR and spike inference quality.

1242 We perturbed the concentration of the indicator, the binding/unbinding rates, and the en-
1243 dogenous buffer concentration to values 100 times smaller and 100 times larger than than
1244 the value taken from the literature. Given that the indicator concentration can be controlled,
1245 at least to some extent, we thought it was worthwhile to simulate these extreme perturba-
1246 tions. For the binding/unbinding rates, such extreme values in these rates are unlikely for
1247 fluorescent calcium indicators or endogenous buffers. But these extreme perturbations are
1248 still useful for studying what kind of fluorescence trace an indicator with such extreme bind-
1249 ing/unbinding rates produce. Similarly, these extreme values in endogenous buffer are also
1250 unlikely to occur in neurons. But, using these values in our model allows us to analyse the
1251 interplay between the endogeneous buffer concentration and the fluorescence trace produced.

1252 Although the model produced visually similar time series to the real data, there were a
1253 few aspects it did not capture. First, the real data featured some low-frequency components
1254 that did not appear related to the spike events. These were not captured by the models we
1255 used in this study, but could be added in future by adding a suitable low-frequency term to
1256 the resulting time series. Second, the real data seemed to have some non-linearities not cap-
1257 tured in the model, for example the response to two nearby spikes was greater than expected
1258 from the linear sum of two single spikes. This may be due to the co-operative binding of
1259 calmodulin to calcium, which gives calmodulin a supra-linear sensitivity to calcium concen-
1260 tration (Faas et al., 2011). The non-linear dynamics of this binding have been included in a
1261 recently developed spike inference model (Greenberg et al., 2018). Our model, in contrast,
1262 behaved much more linearly but could be extended in future to include such non-linearities.
1263 Third, in the real data the fluorescence peak amplitude seemed to vary from spike to spike,
1264 even for well-isolated spike events. Recent research has shown that calcium influx due to a
1265 single action potential was quite variable in pyramidal cells, and that this variability had a
1266 effect on spike inference (Éltes et al., 2019). However in our model we assumed each spike
1267 leads to the same fixed-amplitude injection of calcium to the cell, leading to much greater
1268 regularity in fluorescence peak amplitudes. This variability could be added in future versions
1269 of the model by making the injected calcium peak a random variable. Fourth, we modelled

1270 the soma as a single compartment, but in reality there is likely a non-uniform spatial profile
1271 of calcium concentration. This may matter because some endogenous buffers might access
1272 calcium right as it influxes from the extracellular space, whereas the majority of the fluo-
1273 rescence signal is more likely coming from the bulk of the cytoplasm. Future models could
1274 attempt to model these spatial dependencies to assess whether they affect the overall spike
1275 inference procedure.

1276 The concentration of free calcium ions in the neuron cytoplasm enables calcium sig-
1277 nalling, which has a vital role in neuronal energy metabolism, and neurotransmission in
1278 neurons (Brini et al., 2014). Our model allowed us to examine to which calcium buffer the
1279 incoming free calcium ions, due to an action potential, bound. We found that around 95% of
1280 the calcium ions bound to the fluorescent calcium indicator. This suggests that the introduc-
1281 tion of the fluorescent calcium indicator has a dramatic effect on the free calcium concentra-
1282 tion within the cell cytoplasm. This could have a downstream effect on the functionality of
1283 the cell.

1284 As well as the optimised parameters, the model has 13 fixed parameters than can be
1285 changed to simulate different types of calcium indicators. This model could be used to test
1286 the theoretical performance of proposed new types of calcium indicator. The model could
1287 also be used by developers of spike inference algorithms to test the effects of changing cal-
1288 cium indicator parameters on spike inference, or to test the affects of changing spiking char-
1289 acteristics on spike inference. For example, high firing rate vs low firing rate, or bursting vs
1290 no bursting. Given the increasing amplitude of the fluorescence trace with increasing mean
1291 firing rate, it would be possible to build a spike inference algorithm on this principle at least
1292 in part.

1293 Our model has already been used as a tool by our colleagues, for simulating fluorescence
1294 traces in response to cells that can fire with a continuous rate between 10 and 20Hz, but do
1295 not always do so. Our colleagues found that a combination of the amplitude and the variance
1296 of the simulated fluorescence trace was the best indicator of firing rate. For example, when
1297 a cell was not firing, the amplitude and variance of the fluorescence trace was relatively
1298 low. When the cell fired with a low firing rate $\sim 1\text{Hz}$, the mean amplitude was still low
1299 but the variance of the fluorescence trace was high, and for high firing rate $10 - 20\text{Hz}$, the
1300 fluorescence amplitude was high, and the variance was low. In this way, our model may be
1301 useful for investigating firing rates underlying real fluorescence traces in response to cells
1302 which can fire in these rage ranges.

1303 A recent paper by Greenberg et al (2018) described a biophysical model for spike train

2.4. Discussion

inference called the ‘Sequential binding model’. Their model for spike inference was similar to our model for fluorescence traces in that their model included parameters for two types of endogenous buffer. But this model also included dynamics for calcium binding to and unbinding from these endogenous buffers. Furthermore, this model included dynamics for calcium binding to and unbinding from the four binding sites present on a GCaMP6s molecule. In the accuracy measurements specified in that paper, this model performed better than the MLspike algorithm, which is also partially a biophysically model, and it performed better than the constrained non-negative deconvolution algorithm. The sequential binding model also has biophysically interpretable parameters, and its fitted parameters for quantities such as buffering capacity and calcium influx upon action potential firing fall in line with experimental values (Greenberg et al., 2018). Biophysical models like this appear to be the way forward for spike inference algorithms, and would make a good complimentary tool to our fluorescence model.

1317 **Chapter 3**

1318 **Functional networks expand across**
1319 **anatomical boundaries as correlation**
1320 **time-scale increases**

1321 *Abstract*

1322 Decades of research has established that correlated spiking plays a crucial role in represent-
1323 ing sensory information. One drawback associated with the recent improvement in recording
1324 technology and consequent large datasets is the difficulty in analysing higher order correla-
1325 tions in large neuronal ensembles. One benefit of these datasets that has not yet been explored
1326 is the opportunity to compare correlations within anatomical regions to correlations across
1327 anatomical regions. In this work, we measured correlations between neurons residing in
1328 nine different brains regions in three awake and behaving mice. Using the these correlation
1329 measurements, we created weighted undirected graph networks and applied network science
1330 methods to detect functional communities in our neural ensembles. We compared these func-
1331 tional communities to their anatomical distribution. We repeated the analysis, using different
1332 timescales for our correlation measurements, and found that functional communities were
1333 more likely to be dominated by neurons from a single brain region at shorter timescales
1334 (< 100ms).

1335 3.1 Introduction

1336 Decades of research has established that correlations play a crucial role in representing sen-
1337 sory information. For example, the onset of visual attention has been shown to have a greater
1338 affect on the correlations in the macaque V4 region than on the firing rates in that region
1339 (Cohen and Maunsell, 2009). Recent findings show that spontaneous behaviours explain cor-
1340 relations in parts of the brain not associated with motor control (Stringer et al., 2019), that
1341 satiety state appears to have a brain wide representation (Allen et al., 2019), and that subject
1342 exploratory and non-exploratory states are represented in the amygdala (Gründemann et al.,
1343 2019). So, behavioural states are likely represented across many regions of the brain, not just
1344 motor related areas. In order to understand the brain, we must understand the interactions
1345 between neurons and regions.

1346 Because of limitations in recording technology almost all research has explored corre-
1347 lations between neurons within a given brain region, or within only two regions at most
1348 (Wierzynski et al., 2009; Patterson et al., 2014; Girard, Hupé, and Bullier, 2001). Rela-
1349 tively little is known about correlations between neurons in many different brain regions.
1350 However, the recent development of ‘Neuropixels’ probes (Jun et al., 2017) has allowed
1351 extracellular voltage measurements to be collected from multiple brain regions simultane-
1352 ously routinely, and in much larger numbers than traditional methods. In this project we
1353 used a publicly-available Neuropixels dataset to analyse correlations between different brain
1354 regions (Stringer et al., 2019).

1355 A drawback associated with the improvement in recording technology is an increase in
1356 the difficulty in analysing these data. For example, analysing the i th order interactions of
1357 N neurons generally requires estimation of N^i parameters. A number that becomes astro-
1358 nomical for large N . New methods are required for analysing these new large datasets. We
1359 attempted to address this requirement in this piece of research by applying a cutting-edge
1360 network science community detection method to neural data.

1361 Another unexplored area of research is the changes in cell interactions at different timescales.
1362 Studies have shown different timescales for fluctuations in spiking activity (Murray et al.,
1363 2014), and different time scales for event representation (Baldassano et al., 2017) across dif-
1364 ferent brain regions. Still most studies focus on quantifying interactions at a given timescale.
1365 But neurons may interact differently, or may interact with different neurons at different
1366 timescales. Here we explore correlated communities of neurons at different timescales.

1367 In this work, we measured correlations between binned spike counts from neurons from

3.2. Data

1368 nine different regions of the mouse brain. These measurements induced a weighted undi-
1369 rected graph or network where each neuron is represented by a node, and the strength of
1370 the connection between these nodes/neurons is the strength of the correlation between their
1371 spike counts. We then applied newly invented network methods (Humphries et al., 2019)
1372 to this network to find any community structure, and place the neurons in these correlation
1373 based communities. Finally, we compared these functional communities to the anatomical
1374 membership of the neurons.

1375 To investigate the functional communities and their relationship with anatomy at different
1376 time scales, we repeated these analyses using different length bin widths when binning spike
1377 times.

1378 To find and analyse functional networks while controlling for the subject’s behaviour, we
1379 conditioned the binned spike counts on data from a video of the subject’s face, and repeated
1380 our analysis for spike count correlations (or noise correlations) and signal correlations.

1381 3.2 Data

1382 The data that we used in this project were collected by Nick Steinmetz and his lab members
1383 (Stringer et al., 2019; Steinmetz et al., 2019).

1384 3.2.1 Brain regions

1385 Neuropixels probes were used to collect extracellular recordings (Jun et al., 2017) from three
1386 different mice. The mice were awake, headfixed, and engaging in spontaneous behaviour.
1387 The mice were of different sexes and different ages. One mouse was ‘wild-type’, the others
1388 were mutants. Details as follows:

- 1389 1. male, wild type, P73.
- 1390 2. female, TetO-GCaMP6s, Camk2a-tTa, P113
- 1391 3. male, Ai32, Pvalb-Cre, P99

1392 Eight probes were used to collect readings from 2296, 2668, and 1462 cells respectively.
1393 Data were collected from nine brain regions in each mouse:

- 1394 • Caudate Putamen (CP)
- 1395 • Frontal Motor Cortex (Frmocxt)
- 1396 • Hippocampal formation (Hpf)

- 1397 ● Lateral Septum (Ls)
- 1398 ● Midbrain (Mb)
- 1399 ● Superior Colliculus (Sc)
- 1400 ● Somatomotor cortex (Sommotcx)
- 1401 ● Thalamus (Th)
- 1402 ● Primary visual cortex (V1)

1403 Readings were continuous and lasted for about 1 hour (Stringer et al., 2019; Steinmetz et al.,
1404 2019). Locations of each of the probes can be seen in figure 3.1.

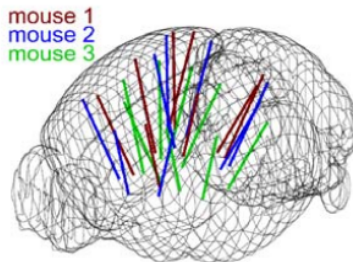


FIGURE 3.1: **Probe Locations:** The locations of the probes in each of the three mouse brains (Stringer et al., 2019).

1405 **3.2.2 Video recordings**

1406 Video recordings of the mouse's face were taken during the spontaneous behaviour. We
1407 had access to the top 500 principal components and top 500 eigenvectors of the processed
1408 videos. The frequency of recording was slightly less than 40Hz. Each frame contained
1409 327×561 pixels (Stringer et al., 2019; Steinmetz, Carandini, and Harris, 2019). These
1410 principal components were used as behavioural data. We controlled for these components
1411 when taking measurements conditioned on behaviour.

1412 **3.3 Methods**

1413 **3.3.1 Binning data**

1414 We transformed the spike timing data into binned spike count data by dividing the experi-
1415 mental period into time bins and counting the spikes fired by each cell within the time period
1416 covered by each of those bins. The data were divided into time bins of various widths ranging
1417 from 0.005s to 4s.

3.3. Methods

If the total length of the recording period was not an integer multiple of the time bin width, we cut off the remaining time at the end of the recording period. This period was at most 3.99s. This is far less than the total recording time of around 1 hour. So, this detail would not affect our results.

3.3.2 Correlation coefficients

We calculated Pearson's correlation coefficient for pairs of spike counts from pairs of neurons. For jointly distributed random variables X and Y , Pearson's correlation coefficient is defined as:

$$\rho_{XY} = \frac{\text{cov}(X, Y)}{\sigma_X \sigma_Y} \quad (3.1)$$

$$= \frac{E[(X - \mu_X)(Y - \mu_Y)]}{\sigma_X \sigma_Y} \quad (3.2)$$

where E denotes the expected value, μ denotes the mean, and σ denotes the standard deviation. The correlation coefficient is a normalised measure of the covariance. It can take values between 1 (completely correlated) and -1 (completely anti-correlated). Two independent variables will have a correlation coefficient of 0, but having 0 correlation does not imply independence.

If we do not know the means and standard deviations required for equation 3.1, but we have samples from X and Y , Pearson's sample correlation coefficient is defined as:

$$r_{XY} = \frac{\sum_{i=1}^n (x_i - \bar{x})(y_i - \bar{y})}{\sqrt{\sum_{i=1}^n (x_i - \bar{x})^2} \sqrt{\sum_{i=1}^n (y_i - \bar{y})^2}} \quad (3.3)$$

where $\{(x_i, y_i)\}$ for $i \in \{1, \dots, n\}$ are the paired samples from X and Y , and $\bar{x} = \frac{1}{n} \sum_{i=1}^n x_i$, and $\bar{y} = \frac{1}{n} \sum_{i=1}^n y_i$ are the sample means.

In practice we used the Python function `scipy.stats.pearsonr` to calculate the correlation coefficients.

1432 Total correlations, r_{SC}

In this context, we defined the total correlation (r_{SC}) of two cells to be the correlation between the spike counts of those cells across the entire period of spontaneous behaviour.

1435 **Shuffled total correlations**

1436 We measured the shuffled total correlations between two neurons by randomly permuting one
 1437 of the neuron's spike counts and measuring the total correlations. These shuffled correlations
 1438 were useful when measuring the effect of time bin width on correlations, and when decid-
 1439 ing which correlations should be preserved when creating correlation networks (see section
 1440 [3.3.5](#)).

1441 **Separating Correlations & Anti-correlations**

1442 In order to compare the effect of bin width on measures of negative r_{SC} (anti-correlation) and
 1443 positive r_{SC} separately, we had to separate correlated and anti-correlated pairs. To do this, we
 1444 simply measured the mean r_{SC} , taking the mean across all the bin widths. If this quantity was
 1445 positive or zero we regarded the pair as positively correlated. If this quantity was negative
 1446 we regarded the pair as anti-correlated.

1447 **3.3.3 Conditioning on behavioural data**

Our behavioural data consisted of the top 500 principal components (PCs) of a processed video recording of the mouse's face (see section [3.2.2](#)). Denoting the spike count of a given cell by X , and the PCs by Z_1, \dots, Z_{500} , we wanted to model X as a function of Z_1, \dots, Z_{500} in order to estimate

$$E[X|Z_1, \dots, Z_{500}] = \int_{x \in X} x P(X = x|Z_1, \dots, Z_{500}) dx \quad (3.4)$$

$$= \int_{x \in X} x \frac{P(X = x, Z_1, \dots, Z_{500})}{P(Z_1, \dots, Z_{500})} dx \quad (3.5)$$

1448 Given the 500 components, a naïve estimation of $P(Z_1, \dots, Z_{500})$ or $P(X, Z_1, \dots, Z_{500})$ by
 1449 histogramming was impossible. Therefore we modelled X as a linear combination of the
 1450 PCs.

1451 **Linear regression**

1452 We modelled the spike count of a given cell, X , as a linear combination of the PCs of the
 1453 video of the mouse's face, $\mathbf{Z} = Z_1, \dots, Z_{500}$. We tried three different types of regularization

1454 • *L*1 or 'Lasso'

1455 • *L*2 or 'Ridge regression'

3.3. Methods

- 1456 • ‘Elastic net’ regularisation (a linear combination of both $L1$ and $L2$ regularisation
1457 penalties)

1458 The elastic net regularisation performed the best, so we stuck with that.

1459 **Elastic net regularisation**

Suppose we wish to model n observations of a random variable X , $\mathbf{x} = (x_1, \dots, x_n)$ using n instances of m predictors $\mathbf{Z} = (Z_1, \dots, Z_m)$. The naïve elastic net criterion is

$$L(\lambda_1, \lambda_2, \boldsymbol{\beta}) = |\mathbf{x} - \mathbf{Z}\boldsymbol{\beta}|^2 + \lambda_2|\boldsymbol{\beta}|_2 + \lambda_1|\boldsymbol{\beta}|_1 \quad (3.6)$$

where $\boldsymbol{\beta}$ is the vector of linear coefficients and

$$|\boldsymbol{\beta}|_2 = \sum_{j=1}^m \beta_j^2 \quad (3.7)$$

$$|\boldsymbol{\beta}|_1 = \sum_{j=1}^m |\beta_j| \quad (3.8)$$

The naïve elastic net estimator $\hat{\boldsymbol{\beta}}$ is the minimiser of the system of equations 3.6 (Zou and Hastie, 2005)

$$\hat{\boldsymbol{\beta}} = \arg \min_{\boldsymbol{\beta}} L(\lambda_1, \lambda_2, \boldsymbol{\beta}) \quad (3.9)$$

1460 We implemented the model using the `ElasticNetCV` method of Python’s
1461 `sklearn.linear_models` package. We chose to put equal weighting on the $L1$ and $L2$
1462 regression parts of equation 3.6. We used 10-fold cross validation to set an optimised value
1463 for $\lambda_1 = \lambda_2$.

1464 As well as using the PCs, we also tried fitting the models using the raw video data recon-
1465 structed from the PCs and eigenvectors. These models performed worse than those using the
1466 PCs. We expected this because each representation contains the same amount of information,
1467 but the raw video representation spreads this information across many more components.
1468 This requires more parameter fitting, but given the same information.

1469 **Conditional covariance**

We calculated the expected value of the conditional covariance using the law of total covariance.

$$\text{cov}(X, Y) = E[\text{cov}(X, Y|Z)] + \text{cov}(E[X|Z], E[Y|Z]) \quad (3.10)$$

1470 where these expected values are calculated with respect to the distribution of Z as a random
1471 variable.

1472 The law of total covariance breaks the covariance into two components. The first com-
1473 ponent $E[\text{cov}(X, Y|Z)]$ is the expected value, under the distribution of Z , of the conditional
1474 covariance $\text{cov}(X, Y|Z)$. This covariance could be interpreted as the unnormalised version
1475 of what Cohen et al. (2011) call the spike count correlation (Cohen and Kohn, 2011), aka.
1476 the noise correlation. In particular, this is the covariance of the spike counts in response to
1477 repeated presentation of identical stimuli.

1478 The second component is analogous to what Cohn et al. (2011) call the *signal correlation*
1479 (Cohen and Kohn, 2011). In particular, $\text{cov}(E[X|Z], E[Y|Z])$ is the covariance between
1480 spike counts in response to different stimuli.

1481 Our linear model gave us 500 coefficients, one for each of Z_1, \dots, Z_{500} . By summing
1482 the linear combination of these coefficients and a set containing one value for each Z_i , we
1483 obtained our model's estimate for the spike count of the cell represented by X . We interpreted
1484 our model as a function that takes a set of values $\{Z_1 = z_1, \dots, Z_{500} = z_{500}\}$ as input and
1485 returns $E[X|Z_1 = z_1, \dots, Z_{500} = z_{500}]$.

1486 Using our linear model, we calculated $E[X|Z_1, \dots, Z_{500}]$ for each cell X and for all sets
1487 of values for $\{Z_1, \dots, Z_{500}\}$ available to us. We used those values to calculate
1488 $\text{cov}(E[X|Z_1, \dots, Z_{500}], E[Y|Z_1, \dots, Z_{500}])$ for each pair of cells (X, Y) . Then we proceeded
1489 to calculate

$$\begin{aligned} E[\text{cov}(X, Y|Z_1, \dots, Z_{500})] &= \text{cov}(X, Y) - \\ &\quad \text{cov}(E[X|Z_1, \dots, Z_{500}], E[Y|Z_1, \dots, Z_{500}]) \end{aligned} \quad (3.11)$$

3.3. Methods

1490 Measures of conditional correlation

As a measure of expected correlation, we measured the ‘event conditional correlation’ (Maugis, 2014)

$$\rho_{XY|Z} = \frac{E[\text{cov}(X, Y|Z)]}{\sqrt{E[\text{var}(X|Z)]}E[\text{var}(Y|Z)]} \quad (3.12)$$

1491 Although this is not an actual correlation, it is an intuitive analogue to the correlation as a
1492 normalised version of the covariance.

For comparison, we also measured the ‘signal correlation’

$$\rho_{\text{signal}} = \frac{\text{cov}(E[X|Z], E[Y|Z])}{\sqrt{\text{var}(E[X|Z])\text{var}(E[Y|Z])}} \quad (3.13)$$

1493 this is an actual correlation.

1494 3.3.4 Information Theory

1495 We used an information theory based measure to measure the difference between the com-
1496 munities that we detected in the correlation based functional networks that we constructed
1497 and the anatomical division of the cells in our data. We treated these as clusterings, and mea-
1498 sured the distance between them. We also were planning on using the mutual information
1499 between the spike counts of cells as measure upon which to build functional networks. But
1500 our measurements turned out to be heavily biased. So we abandoned that approach.

1501 As a result, we have here a lot of background on information theory. This information
1502 is still useful for understanding our measure of distance between between clusterings. So I
1503 think it is worth keeping.

1504 Entropy $H(X)$

The entropy of a random variable X , with outcomes x_1, \dots, x_N , and corresponding probabilities p_1, \dots, p_N is defined as

$$H(X) = - \sum_{n=1}^N p_n \log_2 p_n \quad (3.14)$$

1505 This quantity is also known as the information entropy or the ‘surprise’. It measures the
1506 amount of uncertainty in a random variable. For example, a variable with a probability of 1
1507 for one outcome, and 0 for all other outcomes will have 0 bits entropy, because it contains no

1508 uncertainty. But a variable with a uniform distribution will have maximal entropy as it is the
 1509 least predictable. This quantity is analogous to the entropy of a physical system (Shannon,
 1510 1948). Note that any base may be used for the logarithm in equation 3.14, but using base 2
 1511 means that the quantity will be measured in ‘bits’.

The joint entropy of two jointly distributed random variables X and Y , where Y has outcomes y_1, \dots, y_M , is defined as

$$H(X, Y) = - \sum_{n=1}^N \sum_{m=1}^M P(X = x_n, Y = y_m) \log_2 P(X = x_n, Y = y_m) \quad (3.15)$$

1512 If X and Y are independent then $H(X, Y) = H(X) + H(Y)$. Otherwise $H(X, Y) <$
 1513 $H(X) + H(Y)$. When X and Y are completely dependent and the mapping from X to Y
 1514 is one-to-one, $H(X, Y) = H(X) = H(Y)$.

The conditional entropy of Y conditioned on X is defined as

$$H(Y|X) = - \sum_{n=1}^N \sum_{m=1}^M P(X = x_n, Y = y_m) \log_2 \frac{P(X = x_n, Y = y_m)}{P(X = x_n)} \quad (3.16)$$

1515 When X and Y are independent $H(Y|X) = H(Y)$. Intuitively, we learn nothing of Y by
 1516 knowing X , so Y is equally uncertain whether we know X or not. If Y is totally dependent
 1517 on X , then the fraction in the logarithm is 1, which gives $H(Y|X) = 0$.

1518 These entropy measures are the basis of the mutual information measure.

1519 Maximum entropy limit

1520 Originally, we intended to measure the mutual information between the spike counts of cells.
 1521 We included this section to explain why using larger bin widths resulted in potentially larger
 1522 spike counts, containing potentially more information, corresponding with higher mutual
 1523 information values. The idea of measuring the mutual information between spike counts was
 1524 abandoned. But this section was kept as an illustration of how the number of values a random
 1525 variable can take affects the information conveyed by that variable.

When spiking data is binned into spike counts there is an upper limit on the entropy of these data. The maximum entropy discrete distribution is the discrete uniform distribution. A random variable with this distribution will take values from some finite set with equal probabilities. Binned spike count data will take values between 0 and some maximum observed spike count n_{\max} . A neuron with responses that maximises entropy will take these values with equal probability, i.e. if $i \in \{0, \dots, n_{\max}\}$ then $P(X = i) = \frac{1}{n_{\max}+1}$. The entropy of

3.3. Methods

this neuron will be

$$\begin{aligned}
 H(X) &= - \sum_{i=0}^{n_{\max}} P(X = i) \log_2 P(X = i) \\
 &= - \sum_{i=0}^{n_{\max}} \frac{1}{n_{\max} + 1} \log_2 \left(\frac{1}{n_{\max} + 1} \right) \\
 &= - \log_2 \left(\frac{1}{n_{\max} + 1} \right) \\
 &= \log_2 (n_{\max} + 1)
 \end{aligned}$$

1526 Therefore, the maximum entropy of the binned spike counts of a neuron is $\log_2 (n_{\max} + 1)$.
 1527 Of course, it would be very unusual for a neuron to fire in accordance with the discrete
 1528 uniform distribution. Most measurements of entropy taken on binned spiking data will be
 1529 much lower than the maximum. See figure 3.2 to see the maximum entropy as a function of
 1530 the maximum observed spike count.

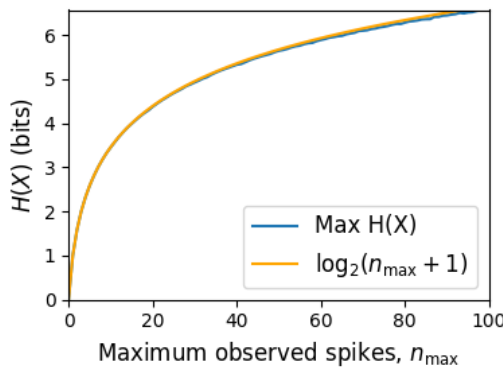


FIGURE 3.2: **Entropy Limit:** The upper limit on entropy of binned spike count data as a function of the maximum observed spike count. The orange line is the analytical maximum. The blue line is the entropy of samples with $N = 1000$ data points taken from the discrete uniform distribution.

1531 **Mutual Information** $I(X; Y)$

1532 The mutual information can be defined mathematically in a number of ways, all of which are
 1533 equivalent. These definitions illustrate the different ways of interpreting the mutual informa-
 1534 tion.

For two jointly distributed random variables X and Y , the mutual information $I(X; Y)$ is defined as

$$I(X; Y) = H(Y) - H(Y|X) \quad (3.17)$$

$$= H(X) - H(X|Y) \quad (3.18)$$

1535 Equation 3.17 fits with the following intuition: The mutual information between X and Y is
1536 the reduction in uncertainty about X gained by knowing Y , or vice versa. We could also say
1537 the mutual information is the amount of information gained about X by knowing Y , or vice
1538 versa.

Another useful entropy based definition for the mutual information is

$$I(X; Y) = H(X) + H(Y) - H(X, Y) \quad (3.19)$$

1539 This definition is useful because it does not require the calculation of conditional probabili-
1540 ties.

The mutual information can also be defined in terms of marginal, joint, and conditional distributions. For example,

$$I(X; Y) = - \sum_{n=1}^N \sum_{m=1}^M P(X = x_n, Y = y_m) \log_2 \frac{P(X = x_n, Y = y_m)}{P(X = x_n)P(Y = y_m)} \quad (3.20)$$

Notice that this can be rewritten as a Kullback–Leibler divergence.

$$I(X; Y) = D_{KL}(P(X, Y) || P(X)P(Y)) \quad (3.21)$$

1541 So, we can also think of the mutual information as a measure of the difference between
1542 the joint distribution of X and Y , and the product of their marginal distributions. Since the
1543 product of the marginal distributions is the joint distribution for independent variables, we
1544 can think of the mutual information as a measure of the variables' dependence on one another.

1545 The minimum value that $I(X; Y)$ can take is 0. This occurs when the random variables
1546 X and Y are independent. Then we have $H(X|Y) = H(X)$, and $H(Y|X) = H(Y)$, which
1547 according to equation 3.17, gives $I(X; Y) = 0$. We also have that $H(X, Y) = H(X) +$
1548 $H(Y)$ in this case, which according equation 3.19, gives $I(X; Y) = 0$. Finally, we also have
1549 $P(X, Y) = P(X)P(Y)$, which leaves us with 1 in the argument for the logarithm in equation
1550 3.20, which again gives $I(X; Y) = 0$.

3.3. Methods

1551 The mutual information reaches its maximum value when one of the variables X and
1552 Y is completely determined by knowing the value of the other. In that case $I(X;Y) =$
1553 $\min\{H(X), H(Y)\}$.

1554 **Variation of Information** $VI(X, Y)$

The variation of information is another information theoretical quantity based on the mutual information. It is defined as

$$VI(X;Y) = H(X) + H(Y) - 2I(X;Y) \quad (3.22)$$

We can rewrite this as the summation of two positive quantities

$$VI(X;Y) = [H(X) - I(X;Y)] + [H(Y) - I(X;Y)] \quad (3.23)$$

1555 In English, the variation of information is the summation of the uncertainty in the random
1556 variables X and Y excluding the uncertainty shared by those variables.

1557 This measure will become more relevant when we go on to talk about clusterings because
1558 $VI(X;Y)$ forms a metric on the space of clusterings.

1559 **Measuring entropies & mutual information**

1560 In practice, we measured the mutual information between spike counts using Python and the
1561 python package `pyitlib`. We used the PT-bias correction technique to estimate the bias of
1562 our measurements when measuring the mutual information between the spike counts of two
1563 cells (Treves and Panzeri, 1995).

1564 When measuring the mutual information between clusterings we used Python, but we
1565 used the `mutual_info_score`, `adjusted_mutual_info_score`, and
1566 `normalized_mutual_info_score` functions from the `sklearn.metrics` part of
1567 the `sklearn` package.

1568 **3.3.5 Network analysis**

1569 **Correlation networks**

1570 In order to analyse functional networks created by the neurons in our ensemble, we mea-
1571 sured the total correlation between each pair of neurons. These measurements induced an

1572 undirected weighted graph/network between the neurons. The weight of each connection
1573 was equal to the total correlation between each pair of neurons.

1574 We followed the same procedure for total correlations 3.3.2, spike count correlations, and
1575 signal correlations 3.3.3.

1576 **Rectified correlations**

1577 At the time of writing, the community detection method outlined in (Humphries et al., 2019)
1578 could only be applied to networks with positively weighted connections. But many neuron
1579 pairs were negatively correlated. To apply the community detection method, we *rectified* the
1580 network, by setting all the negative weights to zero.

1581 We also looked for structure in the network created by negative correlations by reversing
1582 the signs of the correlations, and rectifying these correlations before applying our network
1583 analysis.

1584 Finally, we used the absolute value of the correlations as the weights for the graph/network.
1585 By doing this, we hoped to identify both correlated and anti-correlated functional communi-
1586 ties of neurons.

1587 **Sparsifying data networks**

1588 When creating our correlation networks, we wanted to exclude any correlations that could
1589 be judged to exist ‘by chance’. To do this, we measured the 5th and 95th percentile of
1590 the shuffled correlations (see section 3.3.2) for the given mouse and time bin width. We
1591 then set all the data correlations between these two values to 0. This excluded any ‘chance’
1592 correlations from our network, and created a sparser network. This allowed us to make use
1593 of the ‘sparse weighted configuration model’ as described in section 3.3.5.

1594 **Communities**

1595 Given some network represented by an adjacency matrix \mathbf{A} , a community within that net-
1596 work is defined as a collection of nodes where the number of connections within these nodes
1597 is higher than the expected number of connections between these nodes. In order to quan-
1598 tify the ‘expected’ number of connections, we need a model of expected networks. This is
1599 analogous to a ‘null model’ in traditional hypothesis testing. We test the hypothesis that our
1600 data network departs from the null network model to a statistically significant degree. For
1601 undirected unweighted networks, the canonical model of a null network is the configuration

3.3. Methods

model (Fosdick et al., 2016). Since we are working with weighted sparse networks, we used more suitable null models, described below.

1604 **Weighted configuration model**

1605 The *weighted configuration model* is a canonical null network model for weighted networks.
1606 Given some data network, the weighted configuration model null network will preserve the
1607 degree sequence and weight sequence of each node in the data network. But the edges will
1608 be distributed randomly (Fosdick et al., 2016). Any structure in the data network beyond
1609 its degree sequence and weight sequence will not be captured in the weighted configuration
1610 model. So, this model can be used in testing the hypothesis that this extra structure exists.

1611 **Sparse weighted configuration model**

1612 The *sparse weighted configuration model* is another null network model. Similar in nature to
1613 the weighted configuration model (see section 3.3.5), but the sparsity of the data network is
1614 preserved in the null network. This is achieved by sampling from a probability distribution
1615 for the creation or non-creation of each possible connection, then distributing the weight of
1616 the data network randomly in this sparse network (Humphries et al., 2019). This is the null
1617 network that we used when searching for additional structure in our data networks.

1618 **Spectral rejection**

1619 We made use of the spectral rejection algorithm as outlined in (Humphries et al., 2019). The
1620 spectral rejection algorithm is a method for finding structure in a network not captured by a
1621 supposed null model, if such structure exists.

To describe the method, we denote our data network matrix \mathbf{W} , we denote the expected network of our null network model as $\langle \mathbf{P} \rangle$. Then the departure of our data network from the null network can be described by the matrix

$$\mathbf{B} = \mathbf{W} - \langle \mathbf{P} \rangle \quad (3.24)$$

1622 a common choice for $\langle \mathbf{P} \rangle$ in community detection is the ‘configuration model’ (Fosdick et
1623 al., 2016; Humphries, 2011). The matrix \mathbf{B} is often called the configuration matrix, in this
1624 context we will use the term ‘deviation matrix’ as it captures the deviation of \mathbf{W} from the
1625 null model.

1626 To test for structure in the network represented by \mathbf{W} , we examine the eigenspectrum of \mathbf{B}
1627 and compare it to the eigenspectrum of our null model. Firstly, note that since our data model
1628 doesn't allow self loops, and is not directed, the matrix representing the network will be
1629 symmetric and positive semi-definite, and will therefore be invertible with real eigenvalues.
1630 We selected a null model with the same characteristics.

1631 To find the eigenspectrum of the null model, we generated N samples from our null
1632 model P_1, \dots, P_N , and we measured their deviation matrices B_1, \dots, B_N . We then calculated
1633 the eigenspectrum of each of those samples. We calculated the upper bound of the null model
1634 eigenspectrum by taking the mean of the largest eigenvalues of B_1, \dots, B_N . We calculated a
1635 lower bound on the null model eigenspectrum by taking the mean of the smallest eigenvalues
1636 of B_1, \dots, B_N .

1637 We then calculated the eigenspectrum of \mathbf{B} , our data network deviation matrix. If any of
1638 those eigenvalues lay outside of the upper or lower bounds of the null model eigenspectrum,
1639 this is evidence of additional structure not captured by the null model. If we chose the sparse
1640 weighted configuration model (see section 3.3.5) as our null network model, then eigenvalues
1641 lying below the lower bound indicate k -partite structure in the network. For example, if one
1642 eigenvalue lay below the lower bound, this would indicate some bipartite structure in the data
1643 network. If any eigenvalues lay above the upper bound of the null model eigenspectrum, this
1644 is evidence of community structure in the data network. For example, one eigenvalue of \mathbf{B}
1645 lying above the upper bound of the null model eigenspectrum indicates the presence of two
1646 communities in the network (Humphries, 2011).

1647 **Node rejection**

1648 If there are d data eigenvalues lying outside of the null network eigenspectrum, the d eigen-
1649 vectors corresponding to these eigenvalues will form a vector space. If we project the nodes
1650 of our network into this vector space, by projecting either rows or columns of the data ma-
1651 trix, we can see how strongly each node contributes to the vector space. Nodes that contribute
1652 strongly to the additional structure will project far away from the origin, nodes that do not
1653 contribute to the additional structure will project close to the origin. We want to use this
1654 information to discard those nodes that do not contribute.

1655 We can test whether a node projects *far* away from the origin or *close* to the origin
1656 using the eigenvalues and eigenvectors of B_1, \dots, B_N . The j th eigenvector and eigenvalue
1657 of B_i gives a value for a null network's projection into the j th dimension of the additional
1658 structure vector space. The matrices B_1, \dots, B_N give N projections into that dimension.

3.3. Methods

1659 These projections are a distribution of the null networks' projections. If the data node's
1660 projection exceeds that of the null network projections this node is judged to project *far* from
1661 the origin, and therefore contribute to the additional structure. Otherwise, the node is judged
1662 to project *close* to the origin, and is therefore rejected (Humphries et al., 2019).

1663 **Community detection**

1664 Another application for this d dimensional space is community detection. We first project
1665 all of the nodes into this d -dimensional space, then perform the clustering in this space. The
1666 clustering and community detection procedure is described in (Humphries, 2011).

1667 In practice, the procedure is carried out n times (we chose $n = 100$ times), this returns n
1668 clusterings. We resolve these n clusterings to one final clustering using *consensus clustering*.
1669 We used the consensus clustering method that uses an explicit null model for the consensus
1670 matrix, as outlined in (Humphries et al., 2019).

1671 **3.3.6 Clustering Comparison**

A clustering \mathcal{C} is a partition of a set D into sets C_1, C_2, \dots, C_K , called clusters, that satisfy the following for all $k, l \in \{1, \dots, K\}$:

$$C_k \cap C_l = \emptyset \quad (3.25)$$

$$\bigcup_{k=1}^K C_k = D \quad (3.26)$$

1672 If we consider two clusterings, \mathcal{C} with clusters C_1, C_2, \dots, C_K and \mathcal{C}' with clusters
1673 C'_1, C'_2, \dots, C'_K . There are a number of measurements we can use to compare \mathcal{C} and \mathcal{C}' . In
1674 the following, the number of elements in D is denoted by n , and the number of elements in
1675 cluster C_k is n_k .

1676 **Adjusted Rand Index**

1677 The *adjusted Rand Index* is a normalised similarity measure for clusterings based on pair
1678 counting.

1679 If we consider the clusterings \mathcal{C} and \mathcal{C}' , and denote

1680 • the number of pairs in the same cluster in \mathcal{C} and \mathcal{C}' by N_{11}

1681 • the number of pairs in different clusters in \mathcal{C} and \mathcal{C}' by N_{00}

- 1682 • the number of pairs in the same cluster in \mathcal{C} and different clusters in \mathcal{C}' by N_{10}

- 1683 • the number of pairs in different clusters in \mathcal{C} and the same cluster in \mathcal{C}' by N_{01}

then the *Rand Index* is defined as

$$RI = \frac{N_{11} + N_{00}}{N_{11} + N_{00} + N_{10} + N_{01}} = \frac{N_{11} + N_{00}}{\binom{n}{2}} \quad (3.27)$$

- 1684 The Rand Index is 1 when the clusterings are identical, and 0 when the clusterings are com-
1685 pletely different.

The *adjusted Rand Index* intends on correcting the Rand Index for chance matching pairs.

This is defined as

$$ARI = \frac{2(N_{00}N_{11} - N_{01}N_{10})}{(N_{00} + N_{01})(N_{01} + N_{11}) + (N_{00} + N_{10})(N_{10} + N_{11})} \quad (3.28)$$

- 1686 The adjusted Rand Index is 1 when the clusterings are identical, and 0 when the Rand Index
1687 is equal to its expected value.

1688 When the number of clusters in each clustering is different, the concept of a pair of
1689 being in the same cluster in both clusterings becomes difficult to define. To address this, two
1690 clusterings are drawn randomly with $N_{\mathcal{C}}$ and $N_{\mathcal{C}'}$ number of clusters respectively, and a fixed
1691 number of elements in each cluster corresponding to the number of elements in each cluster
1692 in \mathcal{C} and \mathcal{C}' . Then the adjusted Rand Index is the normalised difference between the Rand
1693 Index of \mathcal{C} and \mathcal{C}' and the mean value of the Rand Index measured using many pairs of these
1694 ‘random’ clusterings.

1695 Clusterings as random variables

If we take any random element of D , the probability that this element is in cluster C_k of
clustering \mathcal{C} is

$$P(K = k) = \frac{n_k}{n} \quad (3.29)$$

- 1696 this defines a probability distribution, which makes the clustering a random variable. Any
1697 clustering can be considered as a random variable this way.

3.3. Methods

This means that we can measure any of the information theoretic quantities defined in section 3.3.4 with respect to clusterings. For example, the entropy of a clustering is

$$H(\mathcal{C}) = - \sum_{k=1}^K \frac{n_k}{n} \log \frac{n_k}{n} \quad (3.30)$$

If we have two clusterings, the joint probability distribution of these clusterings is defined as

$$P(K = k, K' = k') = \frac{|C_k \cap C'_{k'}|}{n} \quad (3.31)$$

- 1698 The joint distribution allows us to define the mutual information between two clusterings,
- 1699 $I(\mathcal{C}; \mathcal{C}')$ (Meilă, 2007).

1700 Information based similarity measures

The mutual information between two clusterings is a similarity measure, with $I(\mathcal{C}; \mathcal{C}') = 0$ if \mathcal{C} and \mathcal{C}' are completely different, and $I(\mathcal{C}; \mathcal{C}') = H(\mathcal{C}) = H(\mathcal{C}')$ if \mathcal{C} and \mathcal{C}' are identical. This can be normalised in a number of different ways to make more similarity measures (Vinh, Epps, and Bailey, 2010)

$$NMI_{joint} = \frac{I(\mathcal{C}; \mathcal{C}')}{H(\mathcal{C}, \mathcal{C}')} \quad (3.32)$$

$$NMI_{max} = \frac{I(\mathcal{C}; \mathcal{C}')}{\max\{H(\mathcal{C}), H(\mathcal{C}')\}} \quad (3.33)$$

$$NMI_{sum} = \frac{2I(\mathcal{C}; \mathcal{C}')}{H(\mathcal{C}) + H(\mathcal{C}')} \quad (3.34)$$

$$NMI_{sqrt} = \frac{I(\mathcal{C}; \mathcal{C}')}{\sqrt{H(\mathcal{C})H(\mathcal{C}')}} \quad (3.35)$$

$$NMI_{min} = \frac{I(\mathcal{C}; \mathcal{C}')}{\min\{H(\mathcal{C}), H(\mathcal{C}')\}} \quad (3.36)$$

We can control for chance similarities between the two clusterings by measuring the *adjusted mutual information* between the clusterings. This is defined as

$$AMI_{sum} = \frac{I(\mathcal{C}; \mathcal{C}') - E\{I(\mathcal{C}; \mathcal{C}')\}}{\frac{1}{2}[H(\mathcal{C}) + H(\mathcal{C}')] - E\{I(\mathcal{C}; \mathcal{C}')\}} \quad (3.37)$$

- 1701 The first term in the denominator, taking the average of the marginal entropies, can be re-
- 1702 placed by taking the maximum, minimum, or the geometric mean (Vinh, Epps, and Bailey,
- 1703 2010).

1704 **Information based metrics**

The variation of information between two clusterings $VI(\mathcal{C}; \mathcal{C}')$ (see section 3.3.4) is a metric on the space of clusterings (Meilă, 2007). That is,

$$VI(\mathcal{C}; \mathcal{C}') \geq 0 \quad (3.38)$$

$$VI(\mathcal{C}; \mathcal{C}') = 0 \iff \mathcal{C} = \mathcal{C}' \quad (3.39)$$

$$VI(\mathcal{C}; \mathcal{C}') = VI(\mathcal{C}'; \mathcal{C}) \quad (3.40)$$

$$VI(\mathcal{C}; \mathcal{C}'') \leq VI(\mathcal{C}; \mathcal{C}') + VI(\mathcal{C}'; \mathcal{C}'') \quad (3.41)$$

Another metric is the *information distance* (Vinh, Epps, and Bailey, 2010)

$$D_{max} = \max\{H(\mathcal{C}), H(\mathcal{C}')\} - I(\mathcal{C}; \mathcal{C}') \quad (3.42)$$

Both of these can be normalised

$$NVI(\mathcal{C}; \mathcal{C}') = 1 - \frac{I(\mathcal{C}; \mathcal{C}')}{H(\mathcal{C}, \mathcal{C}')} \quad (3.43)$$

$$d_{max} = 1 - \frac{I(\mathcal{C}; \mathcal{C}')}{\max\{H(\mathcal{C}), H(\mathcal{C}')\}} \quad (3.44)$$

1705 **Comparing detected communities and anatomical divisions**

1706 In order to quantify the difference or similarity between the communities detected in our cor-
 1707 relation network and the anatomical classification of the cells in that network, we considered
 1708 the communities and the anatomical regions as clusters in two different clusterings, \mathcal{C}_{comm}
 1709 and \mathcal{C}_{anat} , respectively. We then measured the similarity between the clusterings using the
 1710 mutual information, the adjusted mutual information, and the normalised mutual informa-
 1711 tion. We measured the difference between, or the distance between, the clusterings using the
 1712 variation of information, the normalised variation of information, and the normalised infor-
 1713 mation distance. We also measured the difference between the clusterings using the adjusted
 1714 Rand Index, just to use a non-information based measure.

1715 We took all of these measures for communities detected using different time bin widths.
 1716 This gave us an idea of the effect of time bin width on correlation networks in neural ensem-
 1717 bles relative to anatomical regions within those ensembles.

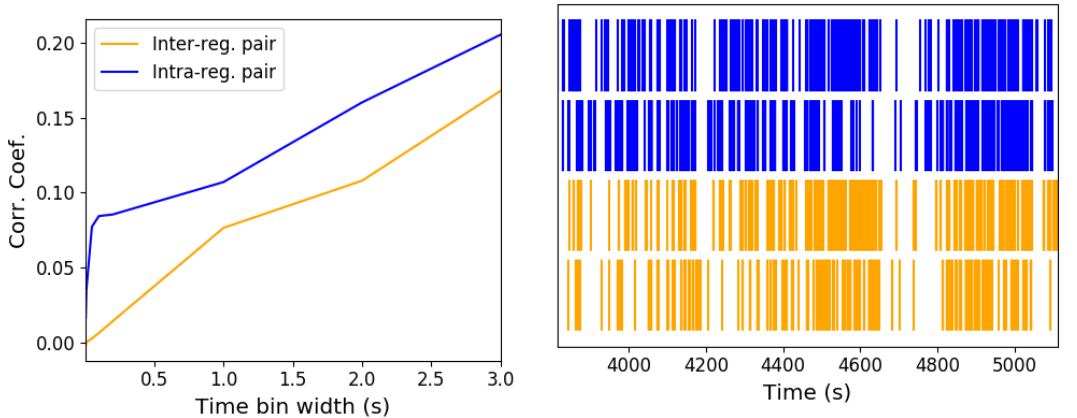
3.4 Results

Note that in the following text, we refer to the correlation coefficient between two sequences of spike counts from two different cells as the *total correlation*. We refer to the correlation between spike counts in response to a certain stimulus as the *spike count correlation* aka *noise correlation*, and we refer to the correlation between mean or expected responses to different stimuli as the *signal correlation* (Cohen and Kohn, 2011).

The nine different brain regions from which we had data were the caudate putamen (CP), frontal motor cortex (FrMoCtx), hippocampus (HPF), lateral septum (LS), midbrain (MB), primary visual cortex (V1), superior colliculus (SC), somatomotor cortex (SomMoCtx), and thalamus (TH).

3.4.1 Average correlation size increases with increasing time bin width

First we inspected the affect of time bin width on total correlations. We know that using short time bins results in artificially small correlation measurements (Cohen and Kohn, 2011), so we expected to see an increase in correlation amplitude with increasing time bin width. That is exactly what we observed. Taking 50 cells at random, we calculated the total correlation between every possible pair of these cells, using different time bin widths ranging from 0.005s to 3s. We found that the longer the time bin width, the greater the correlations (see figure 3.4a).



(A) Correlation coefficient as a function of bin width. (B) Raster plots for the four cells making up our example pairs.

FIGURE 3.3: (A) An example of the correlation coefficients between two different pairs of cells, one where both cells are in the same brain region (intra-regional pair), and one where both cells are in different brain regions (inter-regional pair). The correlation coefficients have been measured using different time bin widths, ranging from 5ms to 3s. Note the increasing amplitude of the correlations with increasing bin width. (B) A raster plot showing the spike times of each pair of cells.

1736 We also separated the positively correlated pairs from the negatively correlated pairs
1737 using the mean correlation of each pair across all bin widths (see section 3.3.2). We found
1738 that the positively correlated pairs become more positively correlated with increasing time bin
1739 width, and the negatively correlated pairs become more negatively correlated with increasing
1740 time bin width (see figures 3.4b and 3.4c).

1741 In figure 3.3a we plot correlations from two example pairs, one pair from within a region,
1742 and one pair between regions. It can be seen that the correlation coefficient increases with
1743 bin width. The correlations can be observed by eye in the raster plot for these cells in figure
1744 3.3b.

1745 When taking the mean across all pairs, the positively correlated pairs dominate in terms
1746 of both number of pairs, and amplitude of correlations. Therefore the mean across all pairs
1747 is positive.

1748 These results were observed in each of the three mouse subjects from which we had data.

1749 **3.4.2 Goodness-of-fit for Poisson and Gaussian distributions across increasing**
1750 **time bin widths**

1751 We wanted to investigate if the width of the time bin used to bin spike times into spike counts
1752 had an effect on the distribution of spike counts. We used the χ^2 statistic as a goodness-of-fit
1753 measure for Poisson and Gaussian (normal) distributions to the spike count of 100 randomly
1754 chosen neurons for a number of bin widths ranging from 0.01s to 4s. For the χ^2 statistic, the
1755 higher the value, the worse the fit.

1756 We expected a Poisson distribution to be a better fit for shorter time bin widths because
1757 spike counts must be non-negative, therefore any distribution of spike counts with mass dis-
1758 tributed at or close to 0 will be skewed. The distribution of spike counts is more likely to be
1759 distributed close to 0 when the time bin widths used to bin spike times into spike counts are
1760 small relative to the amount of time it takes for a neuron to fire an action potential ($\sim 1\text{ms}$ in
1761 the case of non-burst firing neurons).

1762 We expected a Gaussian distribution to be a better fit for longer time bin widths, because
1763 a Poisson distribution with a large rate is well approximated by a Gaussian distribution with
1764 mean and variance equal to the Poisson rate. Therefore, a Gaussian distribution would ap-
1765 proximate the mean of a collection of large spike counts, and have more flexibility than a
1766 Poisson distribution to fit the variance.

3.4. Results

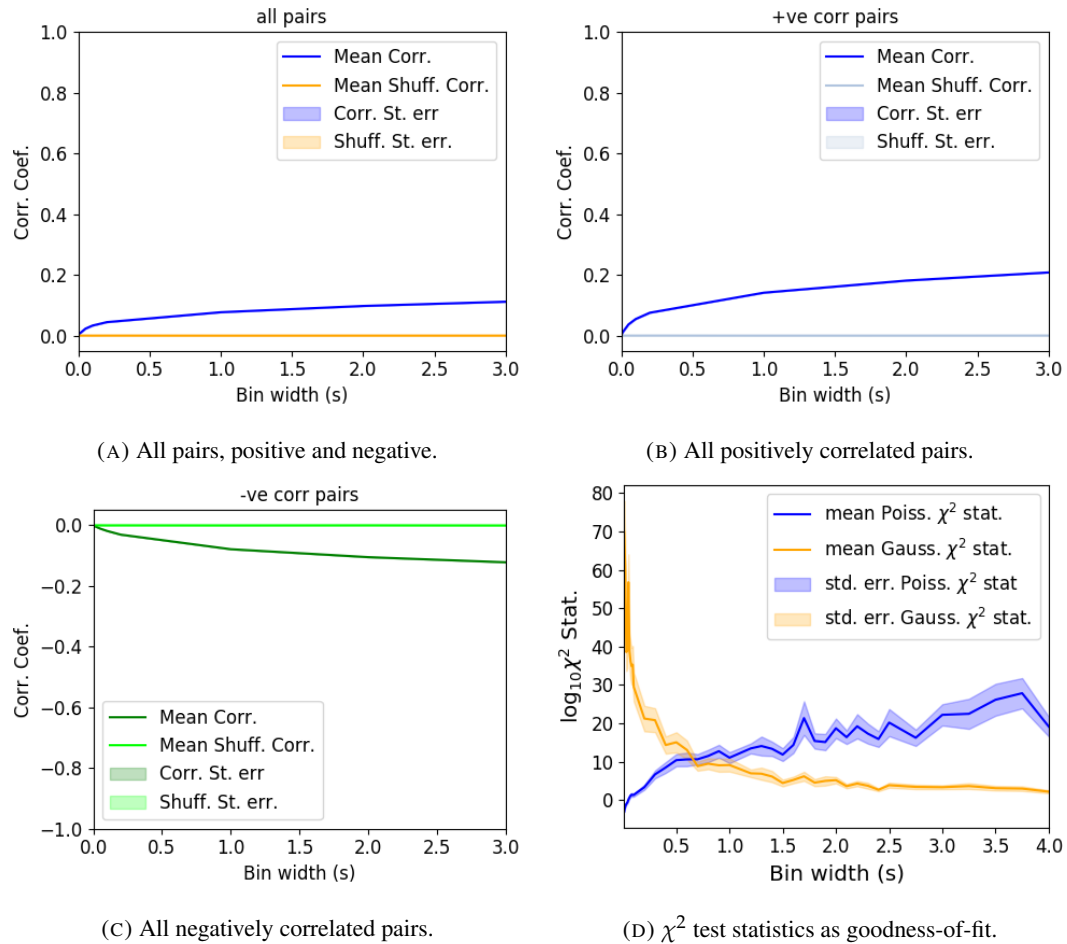


FIGURE 3.4: Mean correlation coefficients measured from pairs of 50 randomly chosen neurons. (A) All possible pairs, (B) positively correlated pairs, and (C) negatively correlated pairs. (D) Mean and standard error of χ^2 test statistics for Poisson and Gaussian distributions fitted to neuron spike counts.

1767 We found that that a Poisson distribution is the best fit for shorter time bins less than 0.7s
1768 in length. Then a Gaussian distribution is a better fit for time bins greater than 0.7s in length
1769 (see figure 3.4d).

1770 **3.4.3 Differences between and inter- and intra- regional correlations decrease
1771 with increasing bin width**

1772 We investigated the differences in distribution between inter-regional correlations, i.e. corre-
1773 lations between neurons in different brain regions, and intra-regional correlations, i.e. corre-
1774 lations between neurons in the same brain region.

1775 Firstly, we investigated these quantities for all possible pairs of ~ 500 neurons taken
1776 from across all the 9 brain regions from which we had data. We distributed these neurons as
1777 evenly as possible across all of the regions, so that cells from one region would not dominate
1778 our data. We observed that the mean intra-regional correlations were always higher than the
1779 mean inter-regional correlations for every value of time bin width used. We also observed
1780 that as the time bin width increased these mean correlations increased and the difference
1781 between the mean inter-regional and intra-regional correlations grew (see figure 3.5 (Left)).

1782 Stringer et al. (2019) had a similar finding using the same data. They used only one value
1783 for the time bin width, 1.2s. Using this time bin width to bin spike times and measure total
1784 correlations, they found that the mean ‘within-region’ correlations were always greater than
1785 the ‘out-of-region’ correlations (Stringer et al., 2019). The figure from their paper showing
1786 this result can be seen in figure 3.5 (Right).

1787 Examples of the correlations of one intra-regional pair and one inter-regional pair can be
1788 seen in figure 3.3.

1789 Secondly, we separated those pairs into intra-regional and inter-regional groups. We
1790 noted that the mean intra-regional correlations (coloured dots in figures 3.6a and 3.6b) for
1791 a given region tended to be higher than the mean inter-regional correlations (black dots in
1792 figures 3.6a and 3.6b) involving cells from that region. However, in contrast with our previous
1793 result, we noted that the difference between the mean intra-regional correlations and most
1794 highly correlated inter-regional correlations reduced as we increased the time bin width (see
1795 figures 3.6a and 3.6b). This shows that the mean correlations showin in figure 3.5 are not
1796 distributed evenly across all region pair combinations.

1797 Finally, to see these regional mean correlations in a bit more detail, to examine the indi-
1798 vidual pair combinations in particular, we displayed these data in a matrix of mean corre-
1799 lations (see figure 3.7), showing the mean intra-regional correlations on the main diagonal, and

3.4. Results

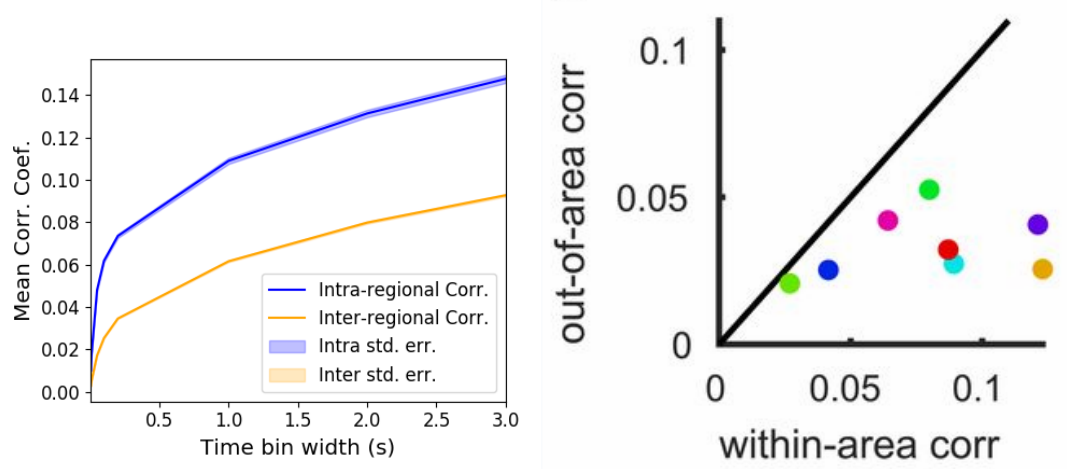


FIGURE 3.5: (Left) The mean intra-region and inter-region correlations using all possible pairs of ~ 500 neurons, spread across 9 different brain regions. (Right) Courtesy of Stringer et al. (2019), mean inter-regional (out-of-area) correlation coefficients vs mean intra-regional (within-area) correlation coefficients for a bin width of 1.2s. Note that the intra-regional coefficients are higher in each case.

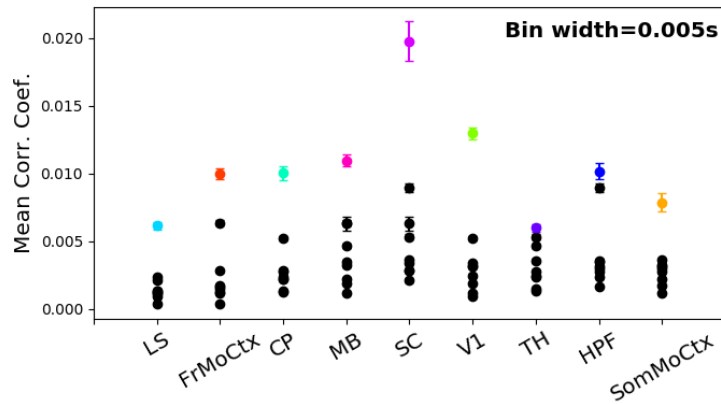
1800 the mean inter-regional correlations off diagonal. Comparing a version of this figure created
 1801 using a short time bin width of 5ms (figure 3.7a) and a version using a longer time bin width
 1802 of 1s (figure 3.7b) we observed that the mean intra-regional correlations are always relatively
 1803 high in comparison to the mean inter-regional correlations, but the mean correlations in some
 1804 inter-regional pairs are relatively much higher when using the longer time bin width.

1805 This could indicate information being processed quickly at a local or within-region level,
 1806 and the local representations of this information spreading between regions at longer timescales.

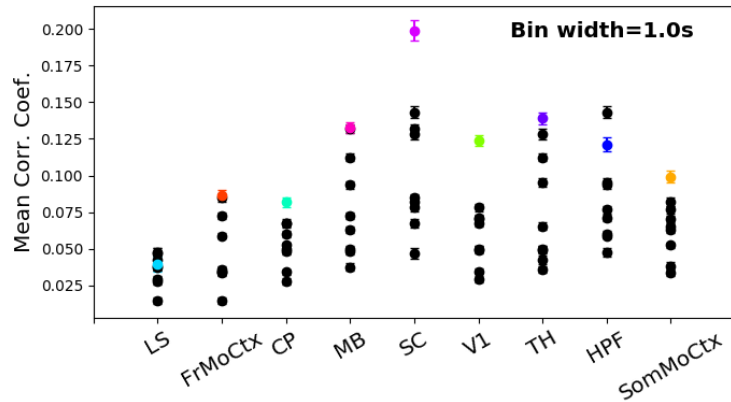
1807 These results were consistent across the three mouse subjects. But, the relative magni-
 1808 tudes of the mean intra-regional and inter-regional correlations were not consistent. For ex-
 1809 ample, the region with the highest mean intra-regional correlations when using 1s bin widths
 1810 for subject one is the superior colliculus (SC), but for subject two it is the midbrain (MB).

1811 **3.4.4 Connected and divided structure in correlation based networks reduces
 1812 in dimension with increasing bin width**

1813 We used the correlation measurements to create weighted undirected graphs/networks where
 1814 each node represents a neuron, and the weight of each edge is the pairwise correlation be-
 1815 tween those neurons represented by the nodes at either end of that edge. We aimed to find
 1816 communities of neurons within these networks, and compare the structure of these commu-
 1817 nities to the anatomical division of those neurons. The first step of this process involved
 1818 applying the ‘spectral rejection’ technique developed by Humphries et al (2019) (Humphries



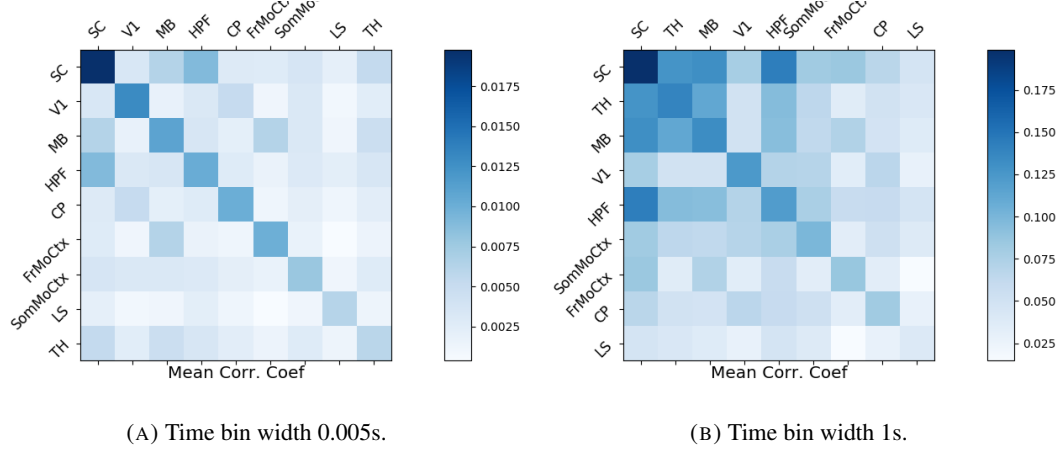
(A) Mean inter-regional and intra-regional correlations using a time bin width of 5ms.



(B) Mean inter-regional and intra-regional correlations using a time bin width of 1s.

FIGURE 3.6: The mean intra-regional correlations (coloured dots) and mean inter-regional correlations (black dots) for a given region, indicated on the x-axis, for different time bin widths. Each black dot represents the mean inter-regional correlations between the region indicated on the x-axis and one other region. (A) shows these measurements when we used a time bin width of 5ms. (B) shows these measurements when we used a time bin width of 1s. Note that the difference between the mean inter-regional correlations and mean intra-regional correlations is smaller for 1s bins.

3.4. Results



(A) Time bin width 0.005s. (B) Time bin width 1s.

FIGURE 3.7: Mean inter-regional (main diagonal) and intra-regional (off diagonal) correlation coefficients. (A) Shows these measurements when spike times were binned using 5ms time bins. (B) Shows the same, using 1s time bins. Note that the matrices are ordered according to the main diagonal values, therefore the ordering is different in each subfigure.

et al., 2019). This technique compares our data network to a chosen null network model, and finds any additional structure in the data network beyond that which is captured in the null network model (if there is any such structure).

By comparing the eigenspectrum of the data network to the eigenspectrum of many samples from the null network model, this technique allows us to estimate the dimensionality of the additional structure in the data network, and gives us a basis for that vector space. It also divides the additional structure into connected structure, and k -partite (or divided) structure. For example, if our algorithm found two dimensions of additional connected structure, and one dimension of additional divided structure. We might expect to find three communities, that is groups more strongly connected within group than without, and we might expect to find bi-partite structure, that is two sets that are more strongly connected between groups than within groups.

The technique also finds which nodes contribute to this additional structure, and divides our data network into signal and noise networks. The details of spectral rejection and node rejection can be found in sections 3.3.5 and 3.3.5 respectively, and a full overview can be found in (Humphries et al., 2019).

We chose the sparse weighted configuration model (see section 3.3.5) as our null network model. This model matches the sparsity and the total weight of the original network but distributes the weight at random across the sparse network.

We applied the spectral rejection method to our networks based on total correlations using different values for the time bin width. We observed that for smaller time bin widths, our data

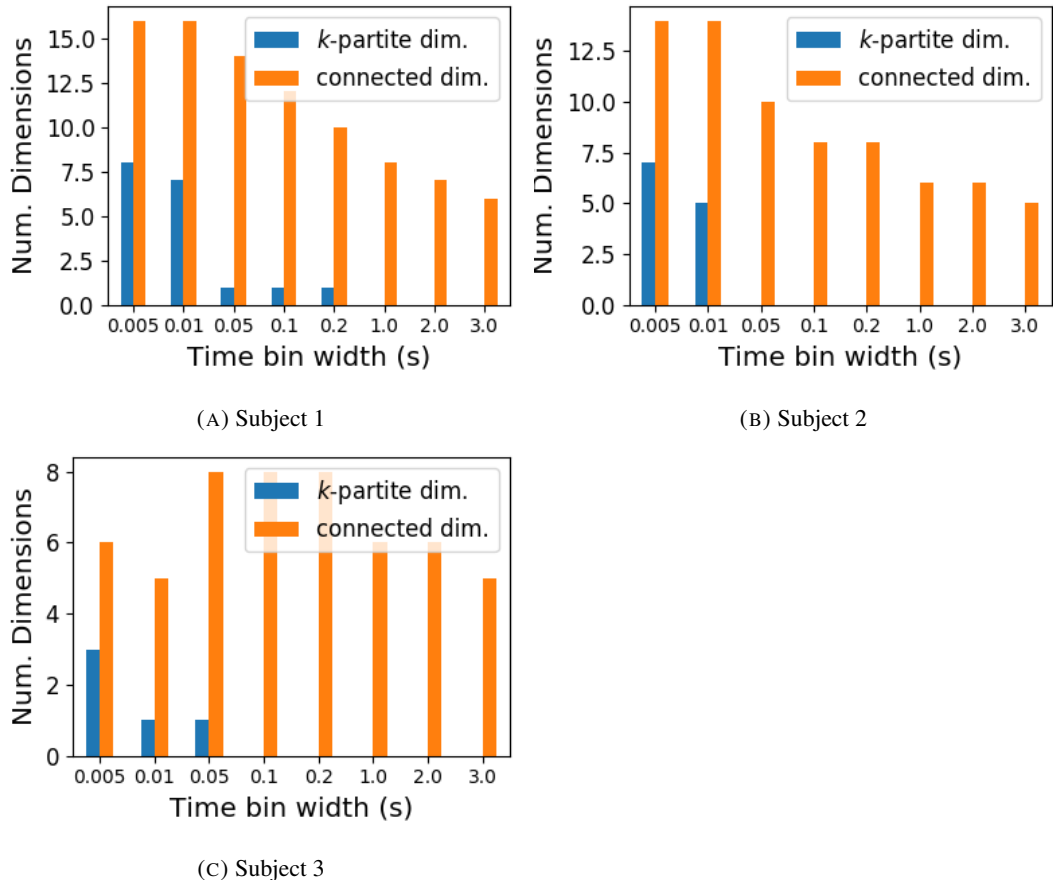


FIGURE 3.8: The number of dimensions in the k -partite and connected structure in the correlation based networks beyond the structure captured by a sparse weighted configuration null network model (see section 3.3.5), shown for different time bin widths. Note that the k -partite structure disappears for time bin width greater than 200ms for all three subjects. The dimension of the connected structure reduces with increasing bin width for 2 of the 3 subjects (top row).

3.4. Results

networks had both k -partite structure, and community structure. As the width of the time bin increased, we found that the k -partite structure disappeared from our data networks, and the dimension of the community structure reduced in two of the three mice from which we had data (see figure 3.8).

The reduction in dimensionality of the connected structure with larger bin widths could indicate information or activity being integrated through the merging of smaller functionaly communities over longer timescales.

The k -partite structure that we found when using small bin widths could be an indication of physical connections between neurons. This is supported by the fact that these k -partite communities are not found over longer timescales. The effect of physical connections through axodendritic or dendrodendritic synapses would only be noticeable at short timescales.

3.4.5 Detecting communities in correlation based networks

We applied the community detection procedure described in section 3.3.5 to our signal networks for our various time bin widths. We detected a greater number of smaller communities at shorter time bin widths, and a smaller number of larger communities for longer time bin widths (see figure 3.9). This was expected after the results found in section 3.4.4. We found more dimensions of additional structure at shorter time bin widths, therefore we found more communities at shorter time bin widths.

The number of communities that we detected was always greater than the dimensionality of the additional structure that we found by applying spectral rejection.

We also noticed that at short time bin widths the communities detected tended to be dominated by cells from one region. Whereas communities existing in networks created using wider time bin widths tended to contain cells from many different brain regions. More on this in the next section.

3.4.6 Functional communities resemble anatomical division at short timescales

In order to quantify the similarity of the communities detected to the anatomical division of the cells. We treated both the anatomical division and the communities as clusterings of these cells. We then used measures for quantifying the difference or similarity between clusterings to quantify the difference or similarity between the detected communities and the anatomical division. Details of these measures can be found in section 3.3.6 or in (Vinh, Epps, and Bailey, 2010).

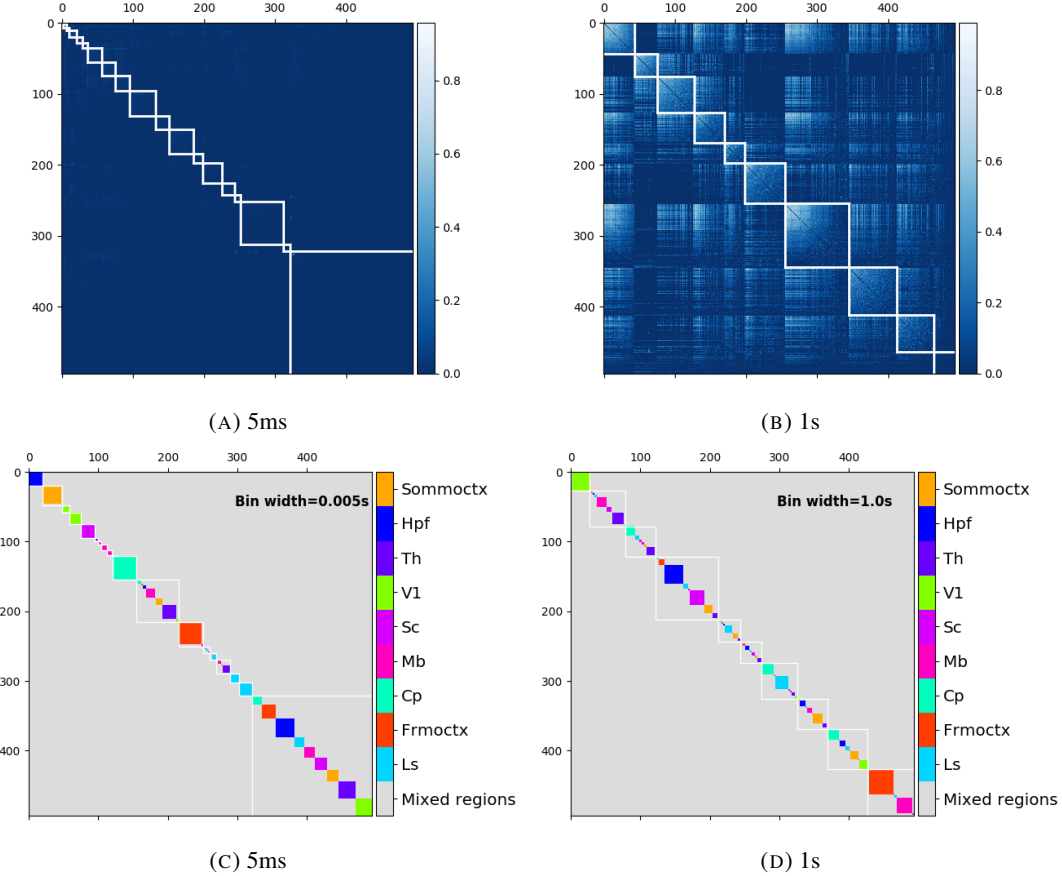


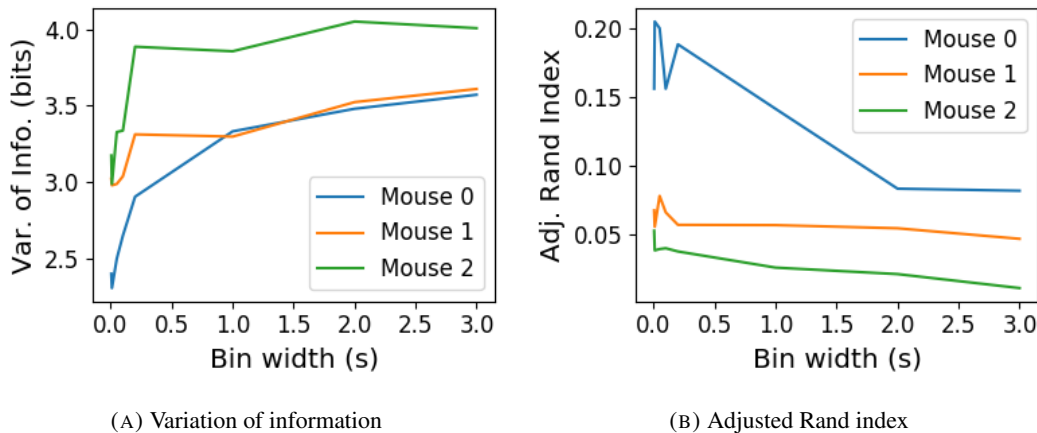
FIGURE 3.9: (A-B) Correlation matrices with detected communities indicated by white lines. Each off main diagonal entry in the matrix represents a pair of neurons. Those entries within a white square indicate that both of those neurons are in the same community as detected by our community detection procedure. Matrices shown are for 5ms and 1s time bin widths respectively. Main diagonal entries were set to 0. (C-D) Matrices showing the anatomical distribution of pairs along with their community membership. Entries where both cells are in the same region are given a colour indicated by the colour bar. Entries where cells are in different regions are given the grey colour also indicated by the colour bar.

3.4. Results

We used two different types of measures for clustering comparison; information based measures (see section 3.3.6) and pair counting based measures (see section 3.3.6). We include one example of each in figure 3.10.

The variation of information is the information based measure included in figure 3.10a. This measure forms a metric on the space of clusterings. The larger the value for the variation of information, the more different the clusterings.

The adjusted Rand index is the pair counting based measure included in figure 3.10b. In contrast with the variation of information, the adjusted Rand index is a normalised similarity measure. The adjusted Rand index takes value 1 when the clusterings are identical, and takes value 0 when the clusterings are no more similar than chance.



(A) Variation of information

(B) Adjusted Rand index

FIGURE 3.10: (A) The variation of information is a measure of distance between clusterings. The distance between the anatomical ‘clustering’ and community detection ‘clustering’ increases with increasing time bin width. (B) The adjusted Rand index is a normalised similarity measure between clusterings. The anatomical and community detection clusterings become less similar as the time bin width increases.

Both measures indicated that the detected communities and the anatomical division of the cells were more similar when we used shorter time bins widths (see figure 3.10). This indicates that correlated behaviour in neuronal ensembles is more restricted to individual brain regions at short timescales (< 250ms), and the correlated activity spreads out across brain regions over longer time scales.

3.4.7 Conditional correlations & signal correlations

In light of the excellent research of Stringer et al (2019) showing that spontaneous behaviours can drive activity in neuronal ensembles across the visual cortex and midbrain (Stringer et al., 2019), we decided to control for the mouse’s behaviour when performing our analyses. It is possible that our community detection process may be detecting communities across

multiple brain regions at longer time scales due to aggregating neuronal activity driven by several spontaneous behaviours occurring during the time interval covered by a given time bin. A time bin of 1s, for example, could contain a spike count where those spikes were driven by different spontaneous behaviours. We aimed to investigate this possibility by applying our community detection analysis to conditional correlation measures.

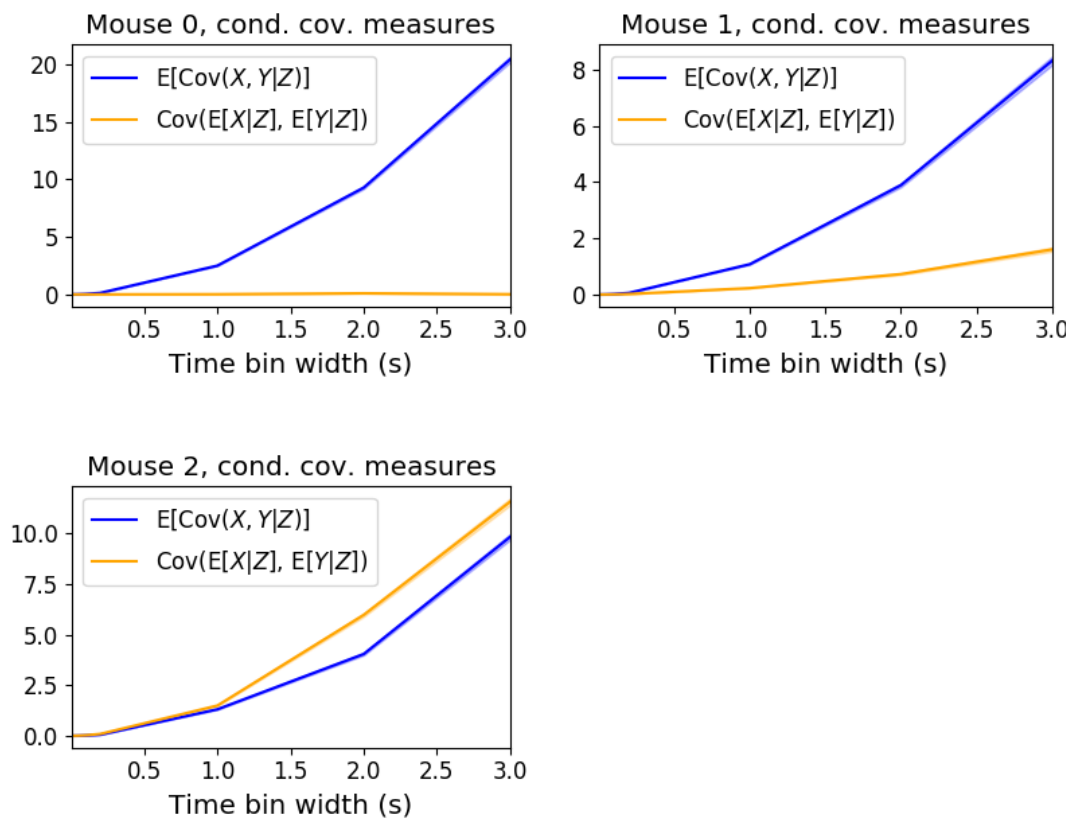


FIGURE 3.11: Comparing the components of the total covariance across different values for the time bin width. We observed a consistent increase in $E[\text{cov}(X, Y|Z)]$ as the time bin width increased. But we saw different trends for $\text{cov}(E[X|Z], E[Y|Z])$ for each mouse.

We used the top 500 principal components of a video of the mouse's face as a measure of the mouse's behaviour (see section 3.2.2). We modelled the spike counts as a linear combination of the principal components using linear regression with ElasticNet regularisation (see section 3.3.3). Using this model, we quantified the expected spike count given the mouse's behaviour $E[X|Z_1, \dots, Z_{500}]$.

We used these expected values to measure $\text{cov}(E[X|Z], E[Y|Z])$, and we used that value, the covariance $\text{cov}(X, Y)$, and the *law of total covariance* (see section 3.3.3) to measure

3.4. Results

1904 $E[\text{cov}(X, Y|Z)]$. Here X and Y represent spike counts from individual cells, and Z is short-
 1905 hand for the 500 principal components mentioned above. The two components of the co-
 1906 variance, $\text{cov}(E[X|Z], E[Y|Z])$ and $E[\text{cov}(X, Y|Z)]$, represent a ‘signal covariance’ and ex-
 1907 pected value of a ‘spike count covariance’ respectively, analogous to the signal correlation
 1908 and spike count correlation (Cohen and Kohn, 2011).

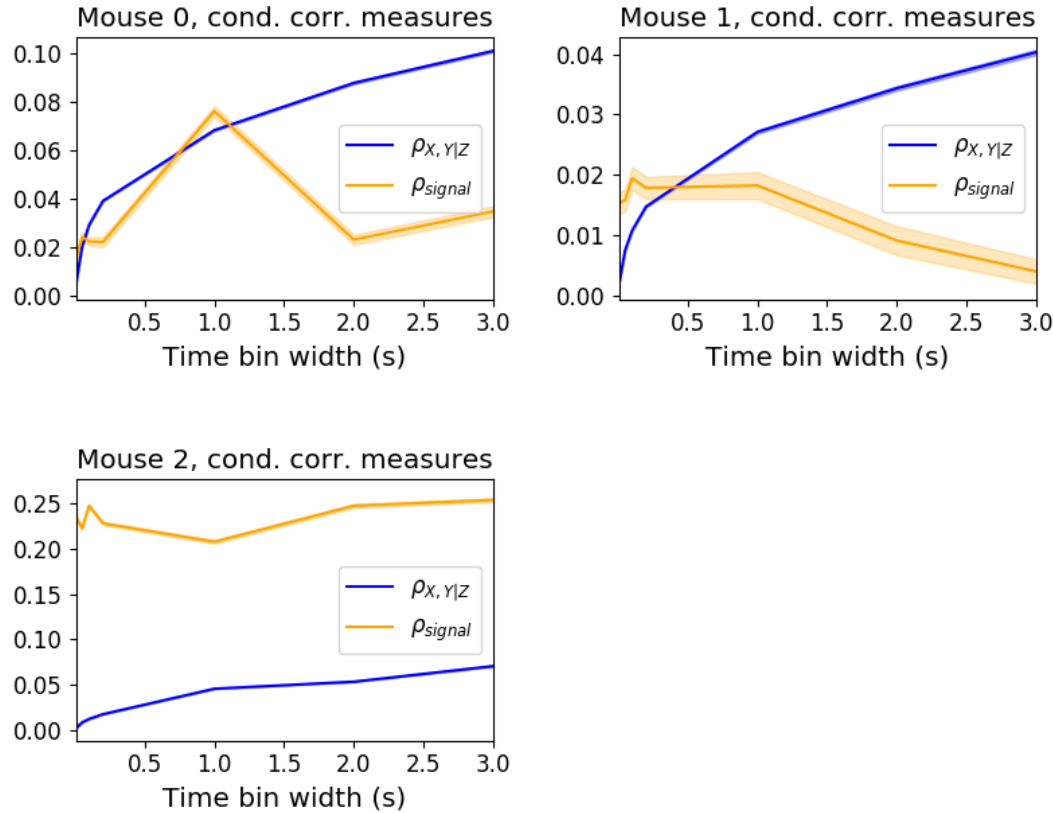


FIGURE 3.12: Comparing the components of the total covariance across different values for the time bin width. We saw a consistent increase in $\rho_{X,Y|Z}$ as the time bin width increased in all three subjects. But we saw different trends in ρ_{signal} for each of the subjects.

1909 We examined the means of these components for different values of the time bin width
 1910 (see figure 3.11). We observed a consistent increase in $E[\text{cov}(X, Y|Z)]$ as the time bin width
 1911 increased. But we saw different trends for $\text{cov}(E[X|Z], E[Y|Z])$ for each mouse.

1912 Using $\text{cov}(E[X|Z], E[Y|Z])$ we measured the signal correlation, ρ_{signal} , and using $E[\text{cov}(X, Y|Z)]$
 1913 we measured the event conditional correlation, $\rho_{X,Y|Z}$ (see section 3.3.3 for more details).
 1914 We saw a consistent increase in $\rho_{X,Y|Z}$ as the time bin width increased, this corresponds to
 1915 the result for $E[\text{cov}(X, Y|Z)]$. We observed different trends for ρ_{signal} for each mouse, this
 1916 corresponds to the result for $\text{cov}(E[X|Z], E[Y|Z])$.

1917 We applied our network noise rejection and community detection process to networks

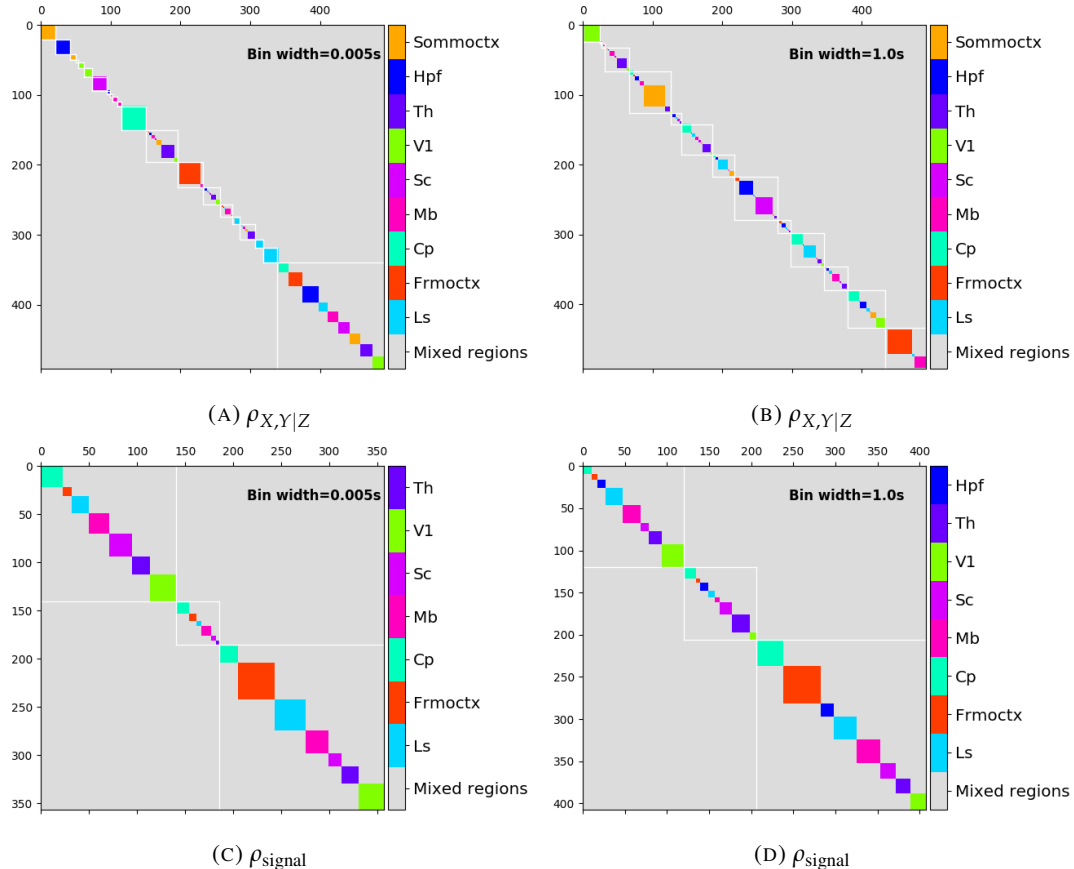


FIGURE 3.13: Matrices showing the regional membership of pairs by colour, and the communities in which those pairs lie. (A-B) Detected communities and regional membership matrix for network based on rectified spike count correlation $\rho_{X,Y|Z}$, using time bin widths of 0.005s and 1s respectively. (C-D) Detected communities and regional membership matrix for network based on rectified signal correlation ρ_{signal} , using time bin widths of 0.005s and 1s respectively.

3.4. Results

1918 based on the spike count correlations $\rho_{X,Y|Z}$ and the signal correlations ρ_{signal} . We noted that
 1919 the community detection on $\rho_{X,Y|Z}$ behaved similarly to the community detection on the total
 1920 correlation. We can see this in figures 3.13a and 3.13b. At very short time bin widths, we
 1921 detect more communities, and those communities often contain cells from one brain region
 1922 only. At longer time bin widths, we detect fewer communities, and those communities tend
 1923 to contain cells from multiple brain regions. When we examine the distance between (or
 1924 similarity between) the anatomical division of the cells, and the detected communities we
 1925 notice that the two clusterings are more similar at shorter time bin widths (see figure 3.14).

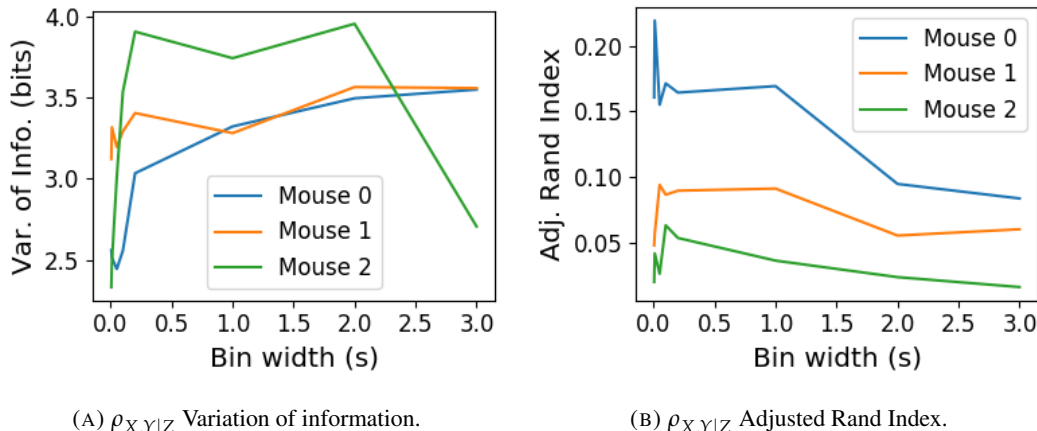


FIGURE 3.14: Distance and similarity measures between the anatomical division of the neurons, and the communities detected in the network based on the spike count correlations $\rho_{X,Y|Z}$. (A) The variation of information is a ‘distance’ measure between clusterings. The distance between the anatomical ‘clustering’ and the community clustering increases as the time bin width increases. (B) The adjusted Rand index is a similarity measure between clusterings. The detected communities become less similar to the anatomical division of the cells as the time bin width increases.

1926 When we applied the network noise rejection and community detection process to the
 1927 networks based on the signal correlations ρ_{signal} we found the number of communities we
 1928 detected reduced with increasing time bin width. But the number of communities detected
 1929 was less than that for the total correlations or the spike count correlations. The communi-
 1930 ties detected always tended to contain cells from multiple regions at both short and long
 1931 timescales (see figures 3.13c and 3.13d). The communities detected bore very little relation
 1932 to the anatomical division of the cells. The adjusted Rand index between the community
 1933 clustering and the anatomical ‘clustering’ is close to zero for every time bin width (see figure
 1934 3.15b). This indicates that the similarity between the clusterings is close to chance. We did
 1935 observe a slight downward trend in the variation of information with increasing bin width
 1936 (see figure 3.15a), but this is more likely due to a decrease in the number of communities

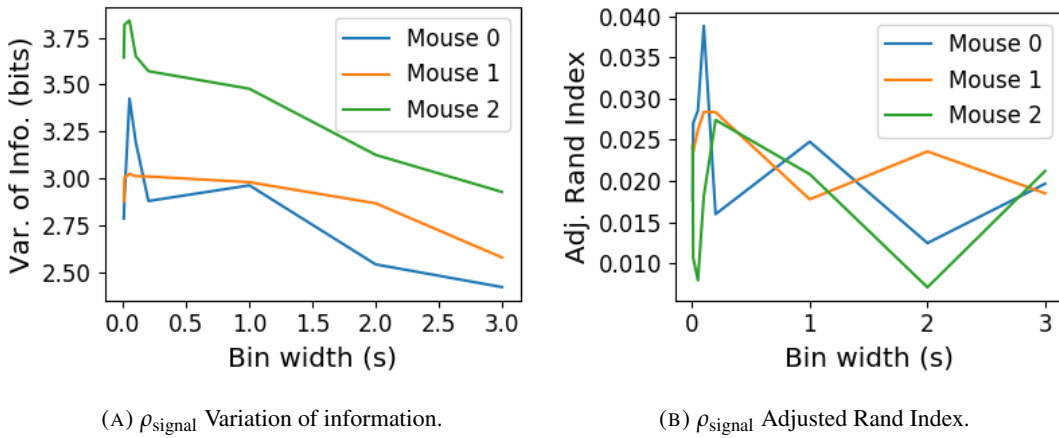
(A) ρ_{signal} Variation of information.(B) ρ_{signal} Adjusted Rand Index.

FIGURE 3.15: Distance and similarity measures between the anatomical division of the neurons, and the communities detected in the network based on the signal correlations ρ_{signal} . (A) The variation of information is a ‘distance’ measure between clusterings. The distance between the anatomical ‘clustering’ and the community clustering increases as the time bin width increases. (B) The adjusted Rand index is a similarity measure between clusterings. The detected communities become less similar to the anatomical division of the cells as the time bin width increases.

1937 detected rather than any relationship with anatomy.

1938 We also observed that the network noise rejection process rejected some of the cells
1939 when applied to the network based on the signal correlations. This means that those cells
1940 did not contribute to the additional structure of the network beyond that captured by the
1941 sparse weighted configuration model. This is why the matrices in figures 3.13c and 3.13d are
1942 smaller than their analogues in figures 3.13a and 3.13b.

1943 The communities detected in the signal correlation based networks indicate that there are
1944 groups of cells from different brain regions that react similarly to different activity states.
1945 These groups also exist at all timescales from milliseconds to seconds. This indicates that
1946 there are subsets of cells in each region that respond to activity states regardless of the
1947 timescale of these activities.

1948 3.4.8 Absolute correlations and negative rectified correlations

1949 At the moment, the network noise rejection protocol can only be applied to weighted undi-
1950 rected graphs with non-negative weights. This meant that we had to rectify our correlated
1951 networks before applying the network noise rejection and community detection process. We
1952 wanted to investigate what would happen if instead of rectifying the correlations, we used the
1953 absolute value, or reversed the signs of the correlations and then rectified.

3.4. Results

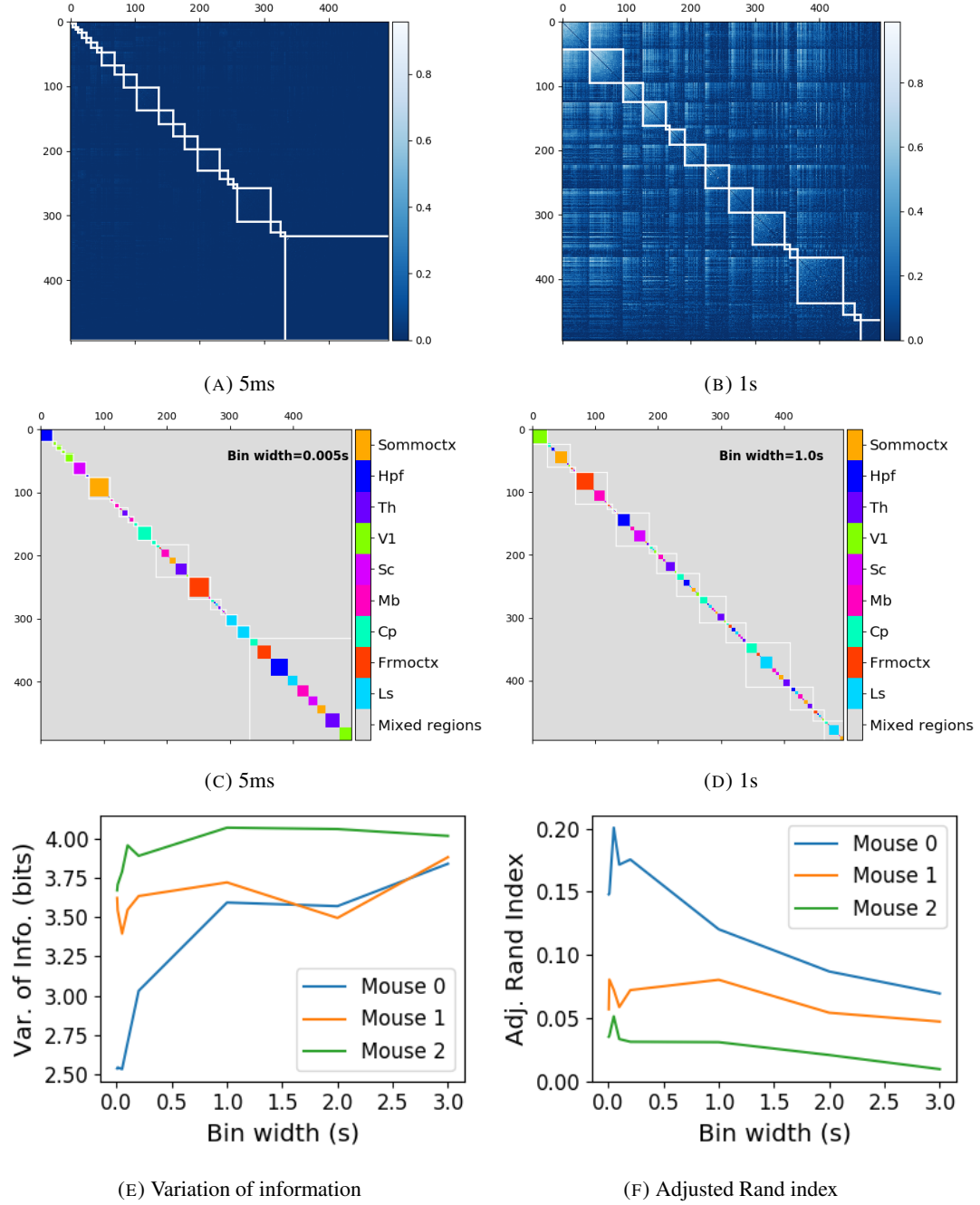


FIGURE 3.16: (A-B) Absolute correlation matrices with detected communities indicated by white lines. These communities are based on the absolute value of the total correlation between each pair of cells. Those entries within a white square indicate that both of those neurons are in the same community. Matrices shown are for 5ms and 1s time bin widths respectively. Main diagonal entries were set to 0. (C-D) Matrices showing the anatomical distribution of pairs along with their community membership. Regional membership is indicated by the colour bar. (E) Variation of information between the anatomical division of the cells, and the detected communities. (F) Adjusted Rand index between the anatomical division, and the detected communities.

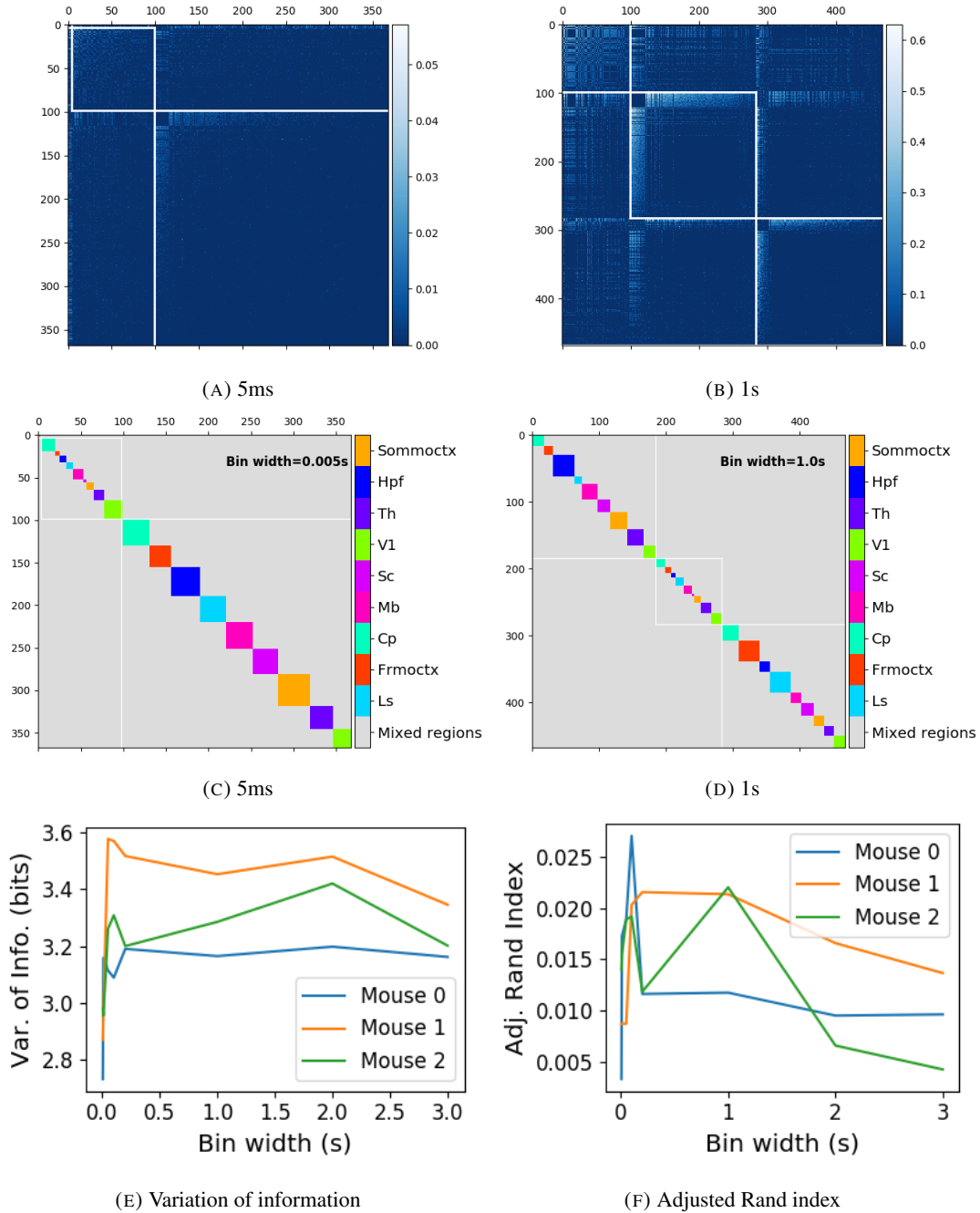


FIGURE 3.17: (A-B) Sign reversed rectified correlation matrices with detected communities indicated by white lines. Those entries within a white square indicate that both of those neurons are in the same community. Matrices shown are for 5ms and 1s time bin widths respectively. Main diagonal entries were set to 0. (C-D) Matrices showing the anatomical distribution of pairs along with their community membership. Regional membership is indicated by the colour bar. (E) Variation of information between the anatomical division of the cells, and the detected communities. (F) Adjusted Rand index between the anatomical division, and the detected communities.

3.5. Discussion

When we used the absolute value of the correlations, we found very similar results to those shown above for the rectified total correlations and the rectified spike count correlations. We detected more communities using shorter bin widths, and these communities were more similar to the brain's anatomy than those communities detected using a longer bin width (see figure 3.16). The only exception being that we detected more communities. This could indicate that we detected both positively and negatively correlated communities, but we haven't done any further investigation so we cannot say for sure.

When we used the sign reversed rectified correlated networks, we tended to find fewer communities. Each community contained cells from many different anatomical regions, at both long and short bin widths (see figures 3.17a, 3.17b, 3.17c, 3.17d). The communities bore little relation to the anatomical distribution of the cells, this can be seen in figure 3.17f, the values close to zero indicate that the similarity between the two clusterings are around chance level. This indicates that there was not much structure in the negatively correlated networks beyond that captured by the sparse weighted configuration model.

3.5 Discussion

It is well established that the brain uses correlated behaviour in neuronal ensembles to represent the information taken in through sensation (Cohen and Maunsell, 2009; Litwin-Kumar, Chacron, and Doiron, 2012; deCharms and Merzenich, 1996). However, most studies that examine the nature of these correlations in-vivo, study an ensemble of cells from only one or two brain regions (Cohen and Kohn, 2011; Wierzynski et al., 2009; Patterson et al., 2014; Girard, Hupé, and Bullier, 2001). Furthermore, recent results have shown that behaviour can drive correlated activity in multiple brain regions, including those not normally associated with motor control (Stringer et al., 2019; Gründemann et al., 2019; Allen et al., 2019). In this study, we utilised one of the newly recorded large datasets containing electrophysiological recordings from multiple brain regions simultaneously. We investigated correlated behaviour in these different brain regions and we investigated correlated behaviour between neurons in different regions, during spontaneous behaviour.

A number of studies have found that the timescale of correlated behaviour induced by a stimulus can be modulated by the stimulus structure and behavioural context. For example, the spike train correlations between cells in weakly electric fish are modulated by the spatial extent of the stimulus (Litwin-Kumar, Chacron, and Doiron, 2012), and neurons in the marmoset primary auditory cortex modulate their spike timing (and therefore correlation) in

1986 response to stimulus features without modulating their firing rate (deCharms and Merzenich,
1987 1996). Furthermore, the width of the time bins over which spike counts are measured has
1988 been shown to have an effect on the magnitude of those correlations (Cohen and Kohn, 2011).
1989 Despite this, very little research has been done comparing correlation measures from the same
1990 dataset at different timescales. We investigated this by varying the time bin width used to bin
1991 spike times into spike counts from as short as 5ms up to 3s.

1992 In order to further investigate the effect of these correlations at different timescales, we
1993 regarded our neuronal ensemble as a weighted undirected graph, where each neuron is rep-
1994 resented by a node, and the weight on each edge is the correlation between the neurons
1995 connected by that edge. We then applied a novel clustering method from network science
1996 (Humphries et al., 2019) to identify communities in these networks. Communities in a net-
1997 work graph refer to sets of nodes that are more strongly connected to each other than the
1998 nodes outside of their set. Another way to put this is to say that the nodes in a community
1999 are more strongly connected than *expected*. What connection strength might be expected is
2000 defined by a null network model. We chose a null network model that matched the sparsity
2001 and total strength of our correlation based data networks. So, if two cells were in the same
2002 community, those cells were more correlated than would be expected given the correlation
2003 strength of their ensemble.

2004 These networks, and the community detection process, were completely agnostic of the
2005 anatomical division of the cells in our ensemble. When we compared the detected commu-
2006 nities with the anatomical division of the cells using distance and similarity measures for
2007 clusterings, we found that the detected communities were more similar to the anatomical
2008 division at shorter timescales. That is, when we used a wider time bin to count spikes, and
2009 computed pairwise correlations with these spike counts, the correlated communities tended to
2010 exist within anatomical regions at shorter timescales, and tended to span anatomical regions
2011 at longer timescales. This could reflect localised functional correlations at short time scales
2012 rippling outwards across brain regions at longer timescales. The brain may be processing
2013 some information quickly locally, and carrying out further, perhaps more detailed, represen-
2014 tation over a longer timescale across many regions using the representations that were just
2015 built locally.

2016 These changes in communities across timescales could also be driven by the anatomy
2017 of the individual cells. For example, it may simply take longer to transmit action potentials
2018 over longer distances, hence correlated activity over longer timescales will exist between

3.5. Discussion

2019 anatomical regions, rather than within. However, the switch to almost exclusively multi-
2020 regional functional networks at 1s bin widths, rather than a mixture of multi-region, and
2021 single-region suggests that the inter-regional correlations either overpower, or inhibit the
2022 local correlations. So there may be more at play than just timescales.

2023 We acknowledged that the region spanning correlated communities that we detected at
2024 longer time scales could exist due to collating activity driven by distinct spontaneous activ-
2025 ities. In order to account for this, we modelled the spike counts as a linear function of the
2026 top 500 principal components of a video of the mouse’s face filmed simultaneously with the
2027 electrophysiological readings. We applied our network noise rejection and community de-
2028 tection process to the weighted undirected networks formed by the spike count correlations
2029 (or noise correlations) and the signal correlations that we calculated using our model. For the
2030 spike count correlation networks, we found much the same results as for the total correlations
2031 as described above. For the signal correlations, the communities detected in these networks
2032 bore little relation to the anatomical division of the cells. Recent findings have shown that
2033 behavioural data accounts for correlations in many brain regions that would otherwise be
2034 dismissed as noise (Stringer et al., 2019), our finding to shows that these correlations are still
2035 governed by the timescale division between local communication and across-region commu-
2036 nication.

2037 There is a lot of room for further investigation based on this research. For a start, the
2038 data that we used here were collected from nine different regions in the mouse brain, but
2039 none of these regions were part of the somatosensory cortex. Given that a mouse experiences
2040 so much of its environment through its sense of smell, some data from this region would be
2041 interesting to investigate. On the same theme, the mice in the experiment from which the
2042 data were collected were headfixed and placed on a rotating ball, but were otherwise behav-
2043 ing spontaneously. Had these mice been exposed to a visual, aural, or olfactory stimulus,
2044 we could have examined the responses of the cells in the brain regions corresponding to vi-
2045 sion, hearing, and olfaction, and compared these responses to the responses from the other
2046 brain regions. Furthermore, we could have investigated the interaction between the sets of
2047 responses.

2048 Another space for further investigation is the community detection. The algorithm that we
2049 used here never detects overlapping communities. But functional communities could indeed
2050 have overlaps. Clustering methods that detect overlapping clusters do exist (Baadel, Thabtah,
2051 and Lu, 2016). Applying one of those algorithms could yield some interesting results. Also,
2052 the community detection algorithm that we used here cannot process graphs with negative

2053 weights, this forced us to separate positive and negative correlations before applying our
2054 network noise rejection and community detections process, or use the absolute value of our
2055 correlations. A community detection algorithm that can work on weighted undirected graphs
2056 with negative weights could yield some interesting results here.

2057 **Chapter 4**

2058 **A simple two parameter distribution
2059 for modelling neuronal activity and
2060 capturing neuronal association**

2061 *Abstract*

2062 Recent developments in electrophysiological technology have lead to an increase in the size
2063 of electrophysiology datasets. Consequently, there is a requirement for new analysis tech-
2064 niques that can make use of these new datasets, while remaining easy to use in practice. In
2065 this work, we fit some one or two parameter probability distributions to spiking data collected
2066 from a mouse exposed to visual stimuli. We show that the Conway-Maxwell-binomial dis-
2067 tribution is a suitable model for the number of active neurons in a neuronal ensemble at any
2068 given moment. This distribution fits these data better than binomial or beta-binomial distribu-
2069 tions. It also captures the correlated activity in the primary visual cortex induced by stimulus
2070 onset more effectively than simply measuring the correlations, at short timescales (< 10ms).
2071 We also replicate the finding of Churchland et al (2010) relating to stimulus onset quenching
2072 neural variability in cortical areas, and we show a correspondence between this quenching
2073 and changes in one of the parameters of the fitted Conway-Maxwell-binomial distributions.

2074 **4.1 Introduction**

2075 Recent advances in electrophysiological technology, such as ‘Neuropixels’ probes (Jun et al.,
2076 2017) have allowed extracellular voltage measurements to be collected from larger numbers
2077 of cells than traditional methods, in multiple brain regions simultaneously, and routinely.
2078 These larger datasets require innovative methods to extract information from the data in a
2079 reasonable amount of time, ‘reasonable’ being subjective in this case.

2080 Theoretically, all the information at any given moment in an electrophysiological dataset
2081 with n neurons could be captured by calculating the probability distribution for every possi-
2082 ble spiking pattern. This would require defining a random variable with 2^n possible values, a
2083 task that quickly becomes impossible as n increases. Attempts at approximating this random
2084 variable often involve measuring pairwise or higher order correlations (Schneidman et al.,
2085 2006; Flach, 2013; Ganmor, Segev, and Schneidman, 2011). But pairwise correlations may
2086 not be enough to characterise instantaneous neural activity (Tkačik et al., 2014). Further-
2087 more, these kinds of models tend to ignore the temporal structure of neuronal data, in favour
2088 of smaller model size, and scalability.

2089 Higher order correlations would be helpful here, but defining and quantifying these cor-
2090 relations can be tricky (Staude, Grün, and Rotter, 2010). If we use the interaction parameters
2091 arising from the exponential family model as measures of higher order correlations, mea-
2092 suring these correlations becomes computationally impractical quite quickly (the number
2093 of ‘three neuron correlations’ to measure scales with $(^n_3)$). In this work, we dispense with
2094 measuring correlations directly, and we attempt to characterise correlated behaviour using a
2095 parameter in statistical model.

2096 In this work, we examined the ability of simple distributions to model the number of
2097 active (spiking) neurons in a neuronal ensemble at any given timepoint. We compared a
2098 little-known distribution named the Conway-Maxwell-binomial distribution to the binomial
2099 distribution and the beta-binomial distribution. The binomial distribution is a probability dis-
2100 tribution over the number of successes in a sequence of independent and identical Bernoulli
2101 trials. The beta-binomial distribution is similar, but allows for a bit more flexibility while still
2102 being a model for heterogeneity. Similar to the binomial and beta-binomial, the Conway-
2103 Maxwell-binomial distribution is a probability distribution over the number of successes in a
2104 series of Bernoulli trials, but allows over- and under-dispersion relative to the binomial dis-
2105 tribution. This distribution should therefore be a good candidate for our purposes. We found
2106 that Conway-Maxwell-binomial distribution was usually the best candidate of the three that

4.2. Data

2107 we examined.

2108 We also observed some interesting changes in the number of active neurons in the primary
2109 visual cortex and hippocampus at stimulus onset and some changes in this activity in the
2110 thalamus which were sustained for the full duration of the stimulus presentation. This let us
2111 know that there were some responses to model.

2112 We found that fitting a Conway-Maxwell-binomial distribution was a better method of
2113 capturing association between neurons than measuring the spike count correlation for the
2114 short time bins that we used (< 10ms).

2115 Finally, we also wanted to investigate parallels between the parameters of the Conway-
2116 Maxwell-binomial distribution and quantities that have been established as relevant to sen-
2117 sory processing. So, we replicated the findings made by Churchland et al. (2010) relating
2118 to a reduction in neural variability at stimulus onset in the macaque cortical regions, but for
2119 data taken from the mouse primary visual cortex. We compared these findings to the values
2120 of the fitted Conway-Maxwell-binomial distribution parameters.

2121 4.2 Data

2122 We used data collected by Nick Steinmetz and his lab ‘CortexLab at UCL’ (Steinmetz, Caran-
2123 dini, and Harris, 2019). The data can be found online ¹ and are free to use for research
2124 purposes.

2125 Two ‘Phase3’ Neuropixels (Jun et al., 2017) electrode arrays were inserted into the brain
2126 of an awake, head-fixed mouse for about an hour and a half. These electrode arrays recorded
2127 384 channels of neural data each at 30kHz and less than $7\mu\text{V}$ RMS noise levels. The sites
2128 are densely spaced in a ‘continuous tetrode’-like arrangement, and a whole array records
2129 from a 3.8mm span of the brain. One array recorded from visual cortex, hippocampus, and
2130 thalamus, the other array recorded from motor cortex and striatum. The data were spike-
2131 sorted automatically by Kilosort and manually by Nick Steinmetz using Phy. In total 831
2132 well-isolated individual neurons were identified.

2133 4.2.1 Experimental protocol

2134 The mouse was shown a visual stimulus on three monitors placed around the mouse at right
2135 angles to each other, covering about ± 135 degrees azimuth and ± 35 degrees elevation.

¹<http://data.cortexlab.net/dualPhase3/>

2136 The stimulus consisted of sine-wave modulated full-field drifting gratings of 16 drift di-
2137 rections ($0^\circ, 22.5^\circ, \dots, 337.5^\circ$) with 2Hz temporal frequency and 0.08 cycles/degree spatial
2138 frequency displayed for 2 seconds plus a blank condition. Each of these 17 conditions were
2139 presented 10 times in a random order across 170 different trials. There were therefore 160
2140 trials with a drifting-grating visual stimulus present, and 10 trials with a blank stimulus.

2141 **4.3 Methods**

2142 **4.3.1 Binning data**

2143 We converted the spike times for each cell into spike counts by putting the spike times into
2144 time bins of a given ‘width’ (in milliseconds). We used time bins of 1ms, 5ms, and 10ms.
2145 We used different time bin widths to assess the impact of choosing a bin width.

2146 **4.3.2 Number of *active* neurons**

2147 To count the number of active neurons in each neuronal ensemble, we split the time interval
2148 for each trial into bins of a given width. We counted the number of spikes fired by each cell
2149 in each bin. If a cell fired *at least* one spike in a given bin, we regarded that cell as active in
2150 that bin. We recorded the number of active cells in every bin, and for the purposes of further
2151 analysis, we recorded each cell’s individual spike counts.

2152 It should be noted that when we used a bin width of 1ms, the maximum number of
2153 spikes in any bin was 1. For the wider time bins, some bins had spike counts greater than
2154 1. Consequently when using a bin width of 1ms, the number of active neurons and the total
2155 spike count of a given bin were identical. But for wider bin widths, the total spike count was
2156 greater than the number of active neurons.

2157 So for the 1ms bin width, the activity of a neuron and the number of spikes fired by that
2158 neuron in any bin can be modelled as a Bernoulli variable. But for wider time bins, only the
2159 activity can be modelled in this way.

2160 **4.3.3 Moving windows for measurements**

2161 When taking measurements (e.g. moving average over the number of active neurons) or
2162 fitting distributions (eg. the beta binomial distribution) we slid a window containing a certain
2163 number of bins across the data, and made our measurements at each window position. For
2164 example, when analysing 1ms bin data, we used a window containing 100 bins, and we slid

4.3. Methods

Bin width (ms)	Window size (bins)	Window size (ms)	Windows per trial
1ms	100	100ms	296
5ms	40	200ms	286
10ms	40	400ms	266

TABLE 4.1: Details of the different bin width and analysis window sizes used when binning spike times, and analysing those data.

2165 the window across the time interval for each trial moving 10 bins at a time. So that for
2166 3060ms of data, we made 296 measurements.

2167 For the 5ms bin width data, we used windows containing 40 bins, and slid the window 2
2168 bins at a time when taking measurements.

2169 For the 10ms bin width data, we used windows containing 40 bins, and slid the window
2170 1 bin at a time when taking measurements (see table 4.1 for concise details).

2171 By continuing to use windows containing 40 bins, we retained statistical power but sac-
2172 rificed the number of measurements taken.

2173 There was an interval between each trial with a grey image in place of the moving bar
2174 stimulus. This interval varied in time. But we included some of this interval when recording
2175 the data for each trial. We started recording the number of active neurons, and the number
2176 of spikes from each neuron from 530ms before each trial until 1030ms after each trial. This
2177 way, we could see the change in our measurements at the onset of a stimulus and the end of
2178 stimulus presentation.

2179 As mentioned in section 4.3.2, we recorded the number of active neurons in each bin, and
2180 the spike count for each neuron in each bin. The measurements we took using these data in
2181 each window were as follows:

2182 **Moving average** The average number of active cells in each window.

2183 **Moving variance** The variance of the number of active cells in each window.

2184 **Average correlation** We measured the correlation between the spike counts of each pair of
2185 cells in the ensemble, and took the average of these measurements.

2186 **Binomial p** We fitted a binomial distribution to the data in each window and recorded the
2187 fitted probability of success, p in each case.

2188 **Beta-binomial α, β** We fitted a beta-binomial distribution to the data in each window, and
2189 recorded the values of the fitted shape parameters, α and β , of each distribution.

2190 **Conway-Maxwell-binomial distribution p, ν** We fitted a Conway-Maxwell-binomial dis-
2191 tribution to the data in each window, and recorded the fitted values of p and ν for each
2192 distribution.

2193 **Log-likelihoods** We also recorded the log-likelihood of each of the fitted distributions for
2194 each window.

2195 **4.3.4 Fano factor**

The *Fano factor* of a random variable is defined as the ratio of the variable's variance to its mean.

$$F = \frac{\sigma^2}{\mu} \quad (4.1)$$

2196 We measured the Fano factor of the spike count of a given cell by measuring the mean and
2197 variance of the spike count across trials, and taking the ratio of those two quantities. When
2198 calculated in this way the Fano factor can be used as a measure of neural variability that
2199 controls for changes in the firing rate. This is similar to the calculation used in (Churchland
2200 et al., 2010).

2201 **4.3.5 Probability Distributions suitable for modelling ensemble activity**

2202 We present here three different probability distributions that could be suitable to model the
2203 number of active neurons in an ensemble. Each distribution has the set $\{0, \dots, n\}$ as its sup-
2204 port, where n is the number of neurons in the ensemble. These are simple distributions with
2205 either two or three parameters each. However, we regard n as known when using these dis-
2206 tributions for modelling, so in effect each distribution has either one or two free parameters.

2207 **Association**

2208 *Association* between random variables is similar to the correlation between random variables
2209 but is more general in concept. The correlation coefficient is a measure of association; and
2210 association doesn't necessarily have a mathematical definition like correlation does. Essen-
2211 tially, an association between two random variables is a dependency of any kind. Positively
2212 associated variables tend to take the same value, and negatively associated variables tend to
2213 take different values. In this research, we work with probability distributions of the num-
2214 ber of successes in a set of Bernoulli trials. These Bernoulli variables may or may not be
2215 associated.

4.3. Methods

2216 A probability distribution over the number of successes in n Bernoulli trials, where the
2217 Bernoulli variables may be associated, could constitute a good model for the number of active
2218 neurons in an ensemble of n neurons. As long as the observation period is divided into time
2219 bins short enough so that any neuron is unlikely to fire more than spike in any time bin.

2220 **Binomial distribution**

The binomial distribution is a two parameter discrete probability distribution that can be thought of as a probability distribution the number of successes from n independent Bernoulli trials, each with the same probability of success. The parameters of the binomial distribution are n the number of trials, and $0 \leq p \leq 1$, the probability of success for each of these trials. A random variable with the binomial distribution can take values from $\{0, \dots, n\}$.

The probability mass function of the distribution is

$$P(k; n, p) = \binom{n}{k} p^k (1-p)^{n-k} \quad (4.2)$$

2221 As a model for the activity of a neuronal ensemble, the main problem with the binomial
2222 distribution is that it treats each neuron, represented as a Bernoulli trial, as independent. It is
2223 well known that neurons are not independent, and that correlated behaviour between neurons
2224 is vital for representing sensory information (Cohen and Maunsell, 2009). The binomial dis-
2225 tribution falls short in this regard, but it is useful as performance benchmark when assessing
2226 the performance of other models.

2227 **Beta-binomial distribution**

2228 The beta distribution is the conjugate distribution of the binomial distribution. The beta-
2229 binomial distribution is the combination of the beta distribution and the binomial distribution,
2230 in that the probability of success for the binomial distribution is sampled from the beta dis-
2231 tribution. This allows the beta-binomial distribution to capture some over dispersion relative
2232 to the binomial distribution.

The beta-binomial distribution is a three parameter distribution, n the number of Bernoulli trials, and $\alpha \in \mathbb{R}_{>0}$ and $\beta \in \mathbb{R}_{>0}$ the shape parameters of the beta distribution. The probability mass function for the beta-binomial distribution is

$$P(k; n, \alpha, \beta) = \binom{n}{k} \frac{B(k + \alpha, n - k + \beta)}{B(\alpha, \beta)} \quad (4.3)$$

2233 where $B(\alpha, \beta)$ is the beta function.

This probability distribution can be reparametrised in a number of ways. One of which defines new parameters π and ρ by

$$\pi = \frac{\alpha}{\alpha + \beta} \quad (4.4)$$

$$\rho = \frac{1}{\alpha + \beta + 1} \quad (4.5)$$

2234 This reparametrisation is useful because π acts as a location parameter analogous to the p
2235 parameter of a binomial distribution. A value of $\rho > 0$ indicates over-dispersion relative to a
2236 binomial distribution.

2237 As a model for the activity of a neuronal ensemble, the beta-binomial distribution is
2238 more suitable than a binomial distribution because the over-dispersion of the beta-binomial
2239 distribution can be used to model positive association between the neurons. An extreme
2240 example of this over-dispersion/positive association can be seen in figure 4.1b. In this figure,
2241 the neurons are positively associated and so tend to take the same value, consequently the
2242 probability mass of the beta-binomial distribution builds up close to $k = 0$ and $k = n$. It is
2243 worth noting that the location parameter for each distribution has the same value, $p = \pi =$
2244 0.5.

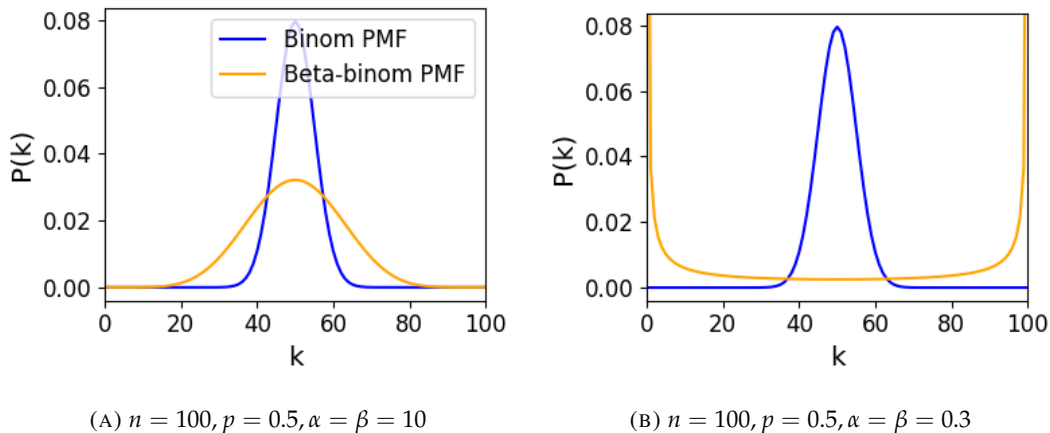


FIGURE 4.1: Figures showing the over-dispersion possible for a beta-binomial distribution relative to a binomial distribution. Parameters are shown in the captions.

2245 **Conway-Maxwell-binomial distribution**

2246 The Conway-Maxwell-binomial distribution (COMb distribution) is a three parameter generalisation of the binomial distribution that allows for over dispersion and under dispersion

4.3. Methods

relative to the binomial distribution. The parameters of the distribution are n the number of Bernoulli trials, and two shape parameters $0 \leq p \leq 1$, and $\nu \in \mathbb{R}$.

The probability mass function of the COMb distribution is

$$P(k; n, p, \nu) = \frac{1}{S(n, p, \nu)} \binom{n}{k}^{\nu} p^k (1-p)^{n-k} \quad (4.6)$$

where

$$S(n, p, \nu) = \sum_{j=0}^n \binom{n}{j}^{\nu} p^j (1-p)^{n-j} \quad (4.7)$$

The only difference between this PMF and the PMF for the standard binomial is the introduction of ν and the consequent introduction of the normalising function $S(n, p, \nu)$.

Indeed, if $\nu = 1$ the COMb distribution is identical to the binomial distribution with the same values for n and p . We can see in figure 4.2d that the KL-divergence $D_{KL}(P_{COMb}(n, p, \nu) || P_{Bin}(n, p)) = 0$ along the line where $\nu = 1$. The analytical expression for the divergence is

$$D_{KL}(P_{COMb}(k; n, p, \nu) || P_{Bin}(k; n, p)) = (\nu - 1) E_{P_{COMb}(k; n, p, \nu)} \left[\log \binom{n}{k} \right] \quad (4.8)$$

$$- \log S(n, p, \nu) \quad (4.9)$$

At $\nu = 1$, we have $S(n, p, 1)$ which is just the sum over the binomial PMF, so $S(n, p, 1) = 1$ and therefore $D_{KL}(P_{COMb}(n, p, \nu) || P_{Bin}(n, p)) = 0$.

If $\nu < 1$ the COMb distribution will exhibit over-dispersion relative to the binomial distribution. If $p = 0.5$ and $\nu = 0$ the COMb distribution is the discrete uniform distribution, and if $\nu < 0$ the mass of the COMb distribution will tend to build up near $k = 0$ and $k = n$. This over-dispersion represents positive association in the Bernoulli variables. An example of this over-dispersion can be seen in figure 4.2b.

If $\nu > 1$ the COMb distribution will exhibit under-dispersion relative to the binomial distribution. The larger the value of ν the more probability mass will build up at $n/2$ for even n , or at $\lfloor n/2 \rfloor$ and $\lceil n/2 \rceil$ for odd n . This under-dispersion represents negative association in the Bernoulli variables. An example of this under-dispersion can be seen in figure 4.2a.

It should be noted that the p parameter of the COMb distribution does not correspond to the mean of the distribution, as is the case for the binomial p parameter, and beta-binomial π parameter. That is, the COMb p parameter is not a location parameter. An illustration of this can be seen in figure 4.2c. This is because an interaction between the p and ν parameters skews the mean. There is no analytical expression for the mean of the COMb distribution.

ν	Relative dispersion	Association between neurons/variables
< 1	over	positive
1	none	none
> 1	under	negative

TABLE 4.2: Relative dispersion of the COMb distribution, and association between Bernoulli variables as represented by the value of the ν parameter.

2268 Since the COMb distribution has the potential to capture positive and negative associa-
2269 tions between the neurons/Bernoulli variables, it should be an excellent candidate for mod-
2270 elling the number of active neurons in a neuronal ensemble.

2271 We wrote a dedicated Python package to enable easy creation and fitting of COMb dis-
2272 tribution objects. The format of the package imitates the format of other distribution objects
2273 from the `scipy.stats` Python package. The COMb package can be found here:

2274 https://github.com/thomasjdelaney/Conway_Maxwell_Binomial_Distribution

2275 4.3.6 Fitting

2276 We fitted binomial, beta-binomial, and Conway-Maxwell-binomial (COMb) distributions to
2277 the neural activity in each of the overlapping windows covering each trial. To fit the distribu-
2278 tions we minimised the appropriate negative log likelihood function using the data from the
2279 window.

There is an analytical solution for maximum likelihood estimate of the binomial distribution's p parameter.

$$\hat{p} = \frac{1}{n} \sum_{i=1}^N k_i \quad (4.10)$$

2280 We minimised the negative log likelihood function of the beta-binomial distribution nu-
2281 merically. We calculated the negative log likelihood for a sample directly, by taking the sum
2282 of the log of the probability mass function for each value in the sample. We minimised the
2283 negation of that function using the `minimise` function of the `scipy.optimize` Python
2284 package.

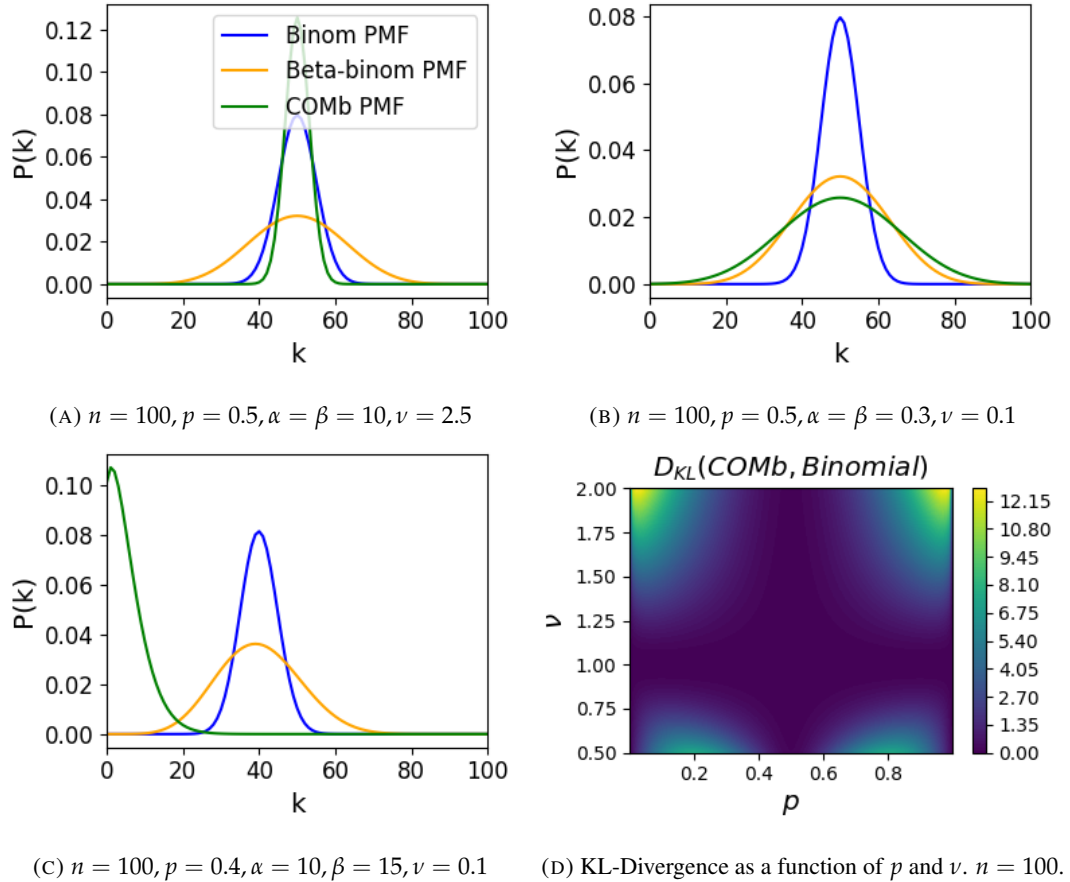


FIGURE 4.2: Figures showing (A) the under-dispersion and (B) over-dispersion permitted by the COMb distribution relative to a binomial distribution. (C) illustrates that the p parameter of the COMb distribution does not correspond to the mean of the distribution, as it does for the binomial and beta-binomial distributions. (D) shows a heatmap for the value of the Kullback-Liebler divergence between the COMb distribution and the standard binomial distribution with same value for n , as a function of p and ν . The point of this figure is to give the reader a sense of how the values of p and ν influence the difference between the COMb distribution and the binomial distribution. The divergence is smallest when $\nu \approx 1$, or when $p \approx 0.5$. When $\nu = 1$, the PMF for the COMb distribution is the same as the PMF for the binomial distribution. When $p = 0.5$ the mass of the distribution is centred around $n/2$ for both the COMb and the binomial distribution. The difference between the two distributions is controlled by the ν parameter. The further the p and ν parameters are from 0.5 and 1 respectively, the greater the difference between the COMb distribution and the binomial distribution. Parameters for all figures are shown in the captions.

The log likelihood function of the COMb distribution given some sample $\{k_1, \dots, k_N\}$ is

$$\ell(p, \nu | k_1, \dots, k_N) = N [n \log(1 - p) - \log S(n, p, \nu)] \quad (4.11)$$

$$+ \log \frac{p}{1 - p} \sum_{i=1}^N k_i \quad (4.12)$$

$$+ \nu \sum_{i=1}^N \log \binom{n}{k_i} \quad (4.13)$$

2285 We minimised the negation of this function using numerical methods. More specifically, we
2286 used the `minimise` function of the `scipy.optimize` Python package.

2287 **4.3.7 Goodness-of-fit**

2288 After fitting, we measured the goodness-of-fit of each model/distribution with their log like-
2289 lihood. We calculated this directly using the `logpmf` functions of the distribution objects in
2290 Python.

2291 **4.4 Results**

2292 We defined a neuron as *active* in a time bin if it fires at least one spike during the time interval
2293 covered by that bin. We measured the number of active neurons in the primary visual cortex
2294 of a mouse in 1ms bins across 160 trials of a moving bar visual stimulus. We then slid a
2295 100ms window across these 1ms bins taking measurements, and fitting distributions along
2296 the way. We did the same for neurons in the thalamus, hippocampus, striatum, and motor
2297 cortex. We repeated the analysis for 5ms time bins with 40 bin windows, and 10ms time bins
2298 with 40 bin windows.

2299 **4.4.1 Increases in mean number of active neurons and variance in number of
2300 active neurons at stimulus onset in some regions**

2301 We measured the average number of active neurons, and the variance of the number of active
2302 neurons in a 100ms sliding window starting 500ms before stimulus onset until 1000ms after
2303 stimulus onset. We found differences in the response across regions. There were no observed
2304 changes in response to the stimulus in the motor cortex or the striatum. The changes in the
2305 other regions are detailed below.

4.4. Results

2306 Primary visual cortex

2307 We found a transient increase in both the average and variance of the number of active neu-
2308 rons at stimulus onset, followed by a fall to pre-stimulus levels, followed by another transient
2309 increase (see figure 4.3). The oscillation in both of these measurements appear to reflect the
2310 frequency of the stimulus (see Data section 4.2.1), and it is known that stimulus structure can
2311 influence response structure(Litwin-Kumar, Chacron, and Doiron, 2012). We see a similar
2312 but lower amplitude oscillation at the end of the stimulus presentation.

2313 Hippocampus

2314 In the hippocampus we observed a transient increase in the average number of active neurons
2315 and in the variance of the number of active neurons at stimulus onset (see figure 4.4). The
2316 increase lasted about 125ms, and the subsequent fall to baseline took the a similar amount of
2317 time.

2318 Thalamus

2319 In the thalamus we observed a transient increase in the both the average and variance of
2320 the number of active neurons on stimulus onset, followed by a fall to pre-stimulus levels,
2321 followed by a sustained increase until the stimulus presentation ends.

2322 As one you might expect for a visual stimulus, the change in the average number of active
2323 neurons was greatest in the primary visual cortex. In this region, this quantity doubled on
2324 stimulus onset. In contrast, in the hippocampus and the thalamus, the average number of
2325 active neurons only increased by a fraction of the unstimulated baseline value. The duration
2326 of the response in V1 and the hippocampus at stimulus onset was 300 – 400ms, but the
2327 response in the thalamus appeared to last for the duration of stimulus presentation. The V1
2328 also showed a change in the average number of active neurons at stimulus end. The change
2329 was similar to that observed at stimulus onset, but smaller in magnitude (see figures 4.3, 4.4,
2330 and 4.5)

2331 4.4.2 Conway-Maxwell-binomial distribution is usually a better fit than bino- 2332 mial or beta-binomial

2333 Since the Conway-Maxwell-binomial distribution has not been fitted to neuronal data before,
2334 it is not clear that it would be a better fit than the binomial or beta-binomial distributions.
2335 In order to find out which parametric distribution was the best fit for the largest proportion

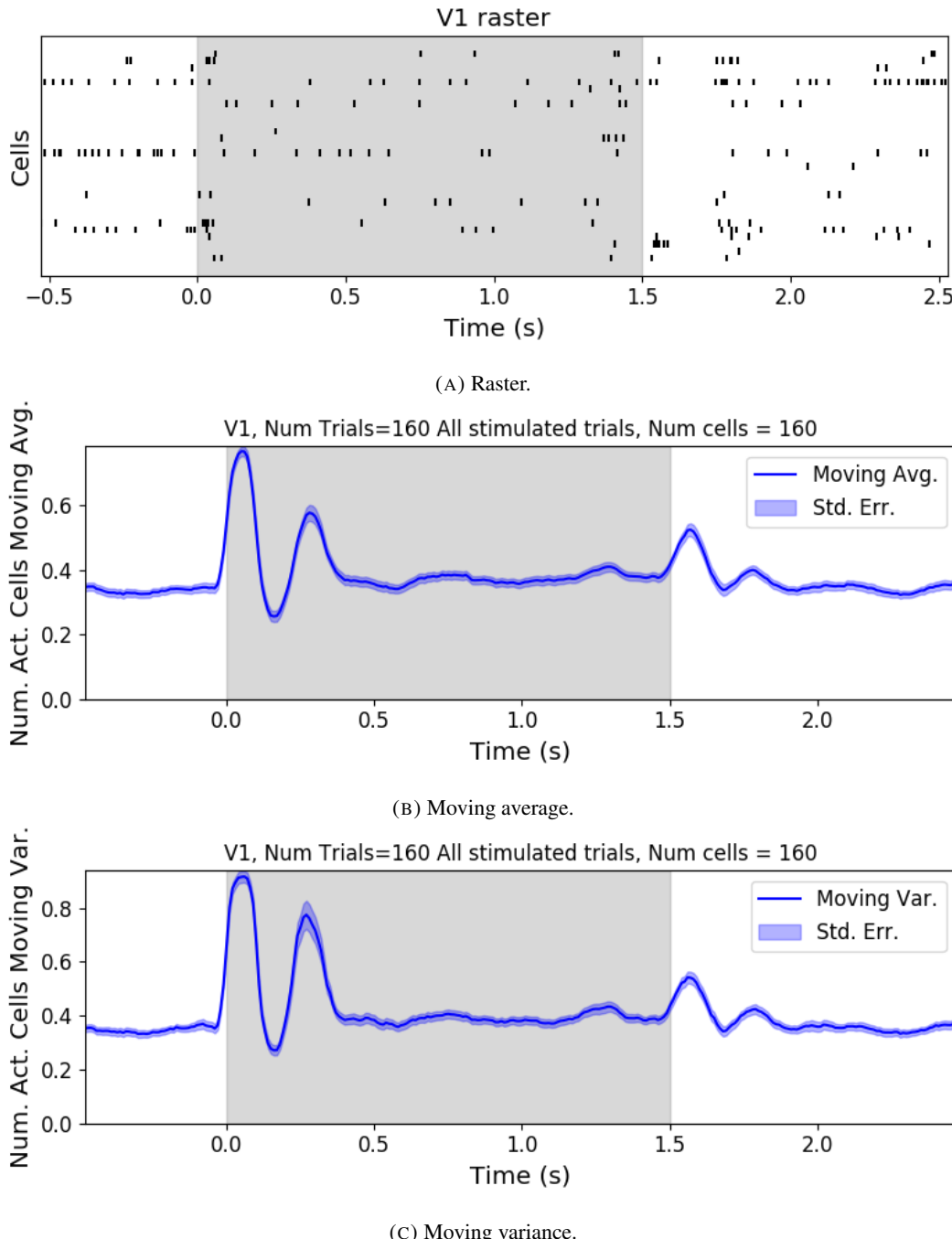


FIGURE 4.3: (A) Raster plot showing the spikes fired by 33 randomly chosen neurons in the primary visual cortex. (B-C) (B) average and (C) variance of the number of active neurons, measured using a sliding window 100ms wide, split into 100 bins. The midpoint of the time interval for each window is used as the timepoint (x-axis point) for the measurements using that window. The grey shaded area indicates the presence of a visual stimulus. The opaque line is an average across the 160 trials that included a visual stimulus of any kind. We can see a transient increase in the average number of active neurons and the variance of this number, followed by a fluctuation and another increase.

4.4. Results

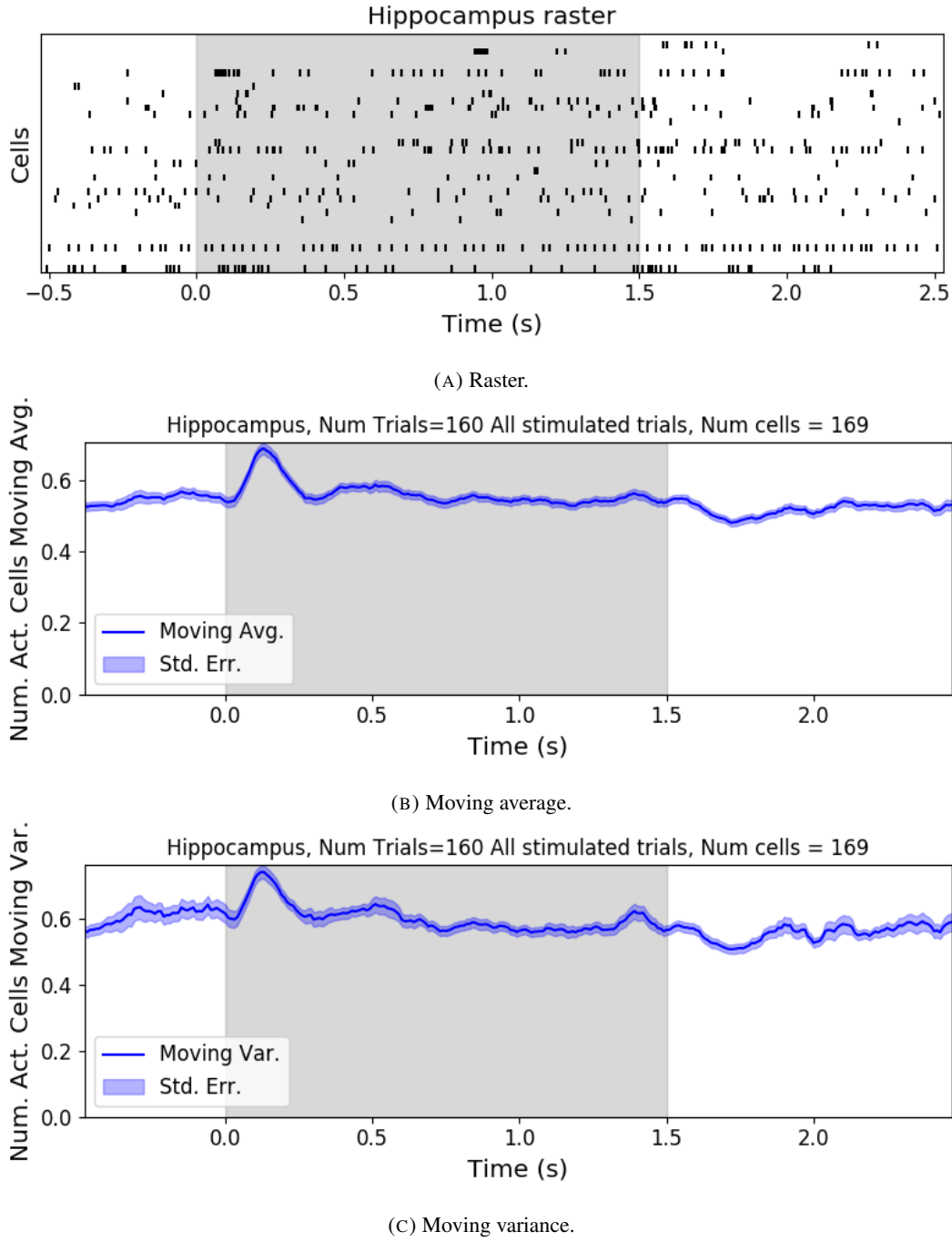


FIGURE 4.4: (A) Raster plot showing the spikes fired by 33 randomly chosen neurons in the hippocampus. (B-C) (B) average and (C) variance of the number of active neurons, measured using a sliding window 100ms wide, split into 100 bins. The midpoint of the time interval for each window is used as the timepoint (x-axis point) for the measurements using that window. The grey shaded area indicates the presence of a visual stimulus. The opaque line is an average across the 160 trials that included a visual stimulus of any kind. We can see a transient increase in the average number of active neurons and the variance of this number at stimulus onset.

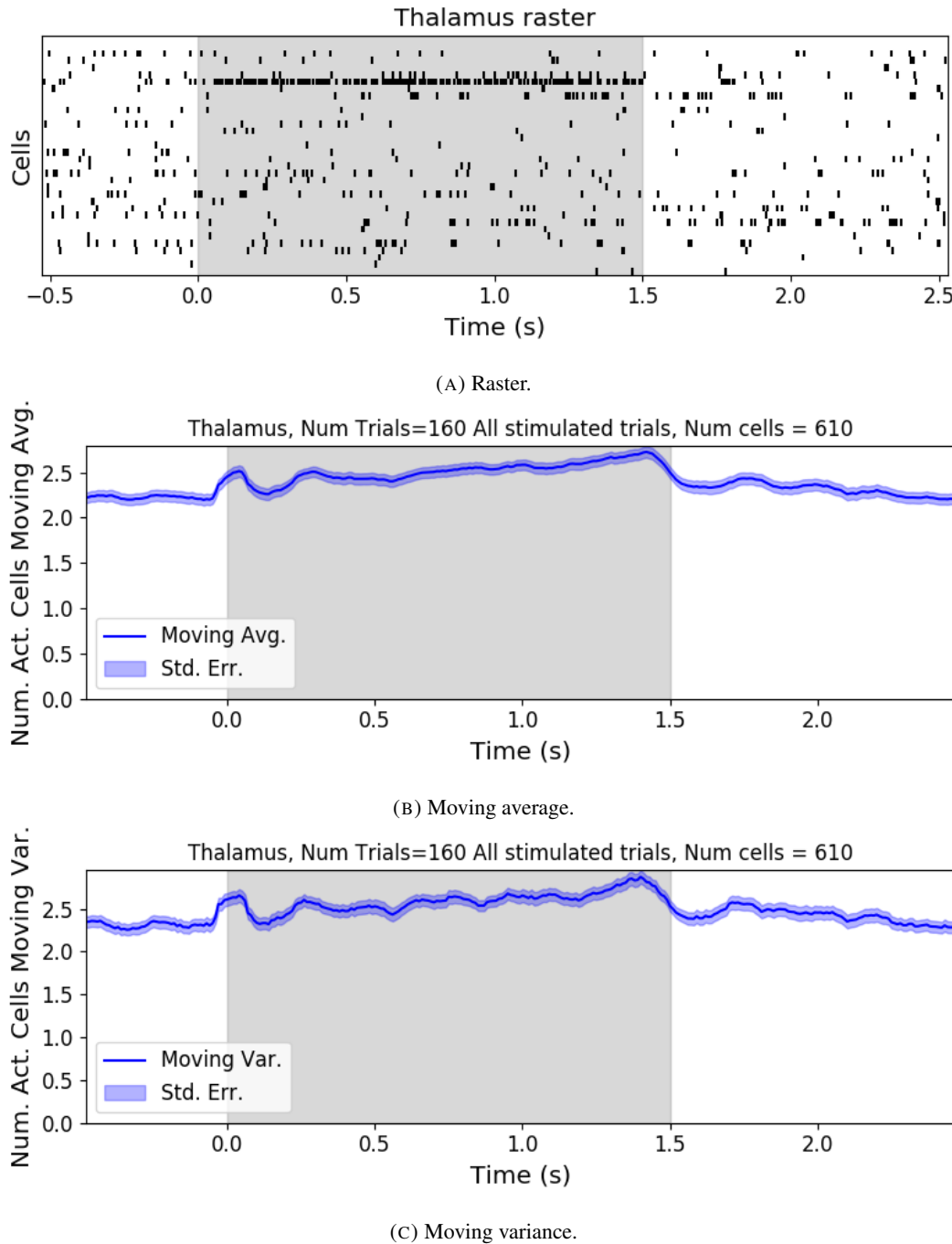
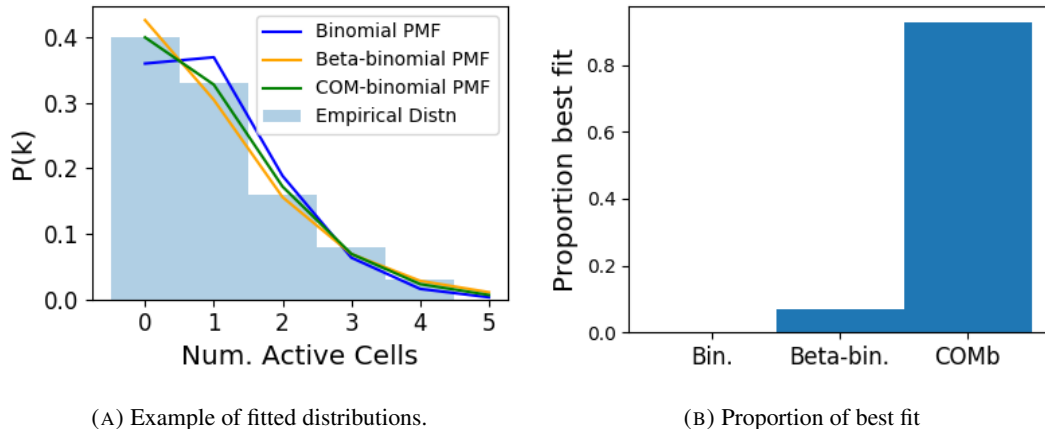


FIGURE 4.5: (A) Raster plot showing the spikes fired by 33 randomly chosen neurons in the thalamus. (B-C) (B) average and (C) variance of the number of active neurons, measured using a sliding window 100ms wide, split into 100 bins. The midpoint of the time interval for each window is used as the timepoint (x-axis point) for the measurements using that window. The grey shaded area indicates the presence of a visual stimulus. The opaque line is an average across the 160 trials that included a visual stimulus of any kind. We can see an immediate increase at stimulus onset, a subsequent fall, and another sustained increased until the stimulus presentation ends.

4.4. Results

of our data, we fit a binomial, a beta-binomial, and a Conway-Maxwell-binomial (COMb) distribution to each window for each bin width, and each region. Then we assessed the goodness-of-fit of each distribution by calculating the log-likelihood of each fitted distribution using the associated sample. We measured the proportion of samples for which each distribution was the best fit, for each bin width value and each region.

We found that the COMb distribution was the best fit for most of the samples regardless of bin width or region. The bin width had an effect on the number of samples for which the COMb distribution was the best fit. The results are summarised in table 4.3. For a bin width of 1ms, the COMb distribution was the best fit for over 90% of samples, the beta-binomial distribution was the best fit for less than 10% of samples, and the binomial distribution was the best fit for less than 1% of samples, across regions. For 5ms bins, the COMb distribution was the best fit for 70 – 80% of samples, the beta-binomial distribution was the best fit for 20 – 30% of the samples, and again the binomial distribution was the best fit for less than 1% of samples, across regions. Finally, for 10ms bins, the COMb distribution was the best fit for 53 – 80% of samples, the beta-binomial distribution was the best fit for 20 – 47% of the samples, and the binomial distribution was the best fit for less than 0.1% of samples, across regions.



(A) Example of fitted distributions.

(B) Proportion of best fit

FIGURE 4.6: (A) An example of the binomial, beta-binomial, and Conway-Maxwell-binomial distributions fitted to a sample of neural activity. The Conway-Maxwell-binomial distribution is the best fit in this case. The histogram shows the empirical distribution of the sample. The probability mass function of each distribution is indicated by a different coloured line. (B) Across all samples in all trials, the proportion of samples for which each fitted distribution was the best fit. The Conway-Maxwell-binomial distribution was the best fit for 93% of the samples taken from V1 using a bin width of 1ms.

Bin Width (ms)	Binomial	Beta-binomial	COMb
1ms	< 1%	< 10%	> 90%
5ms	< 0.1%	20 – 30%	70 – 80%
10ms	< 0.1%	20 – 47%	53 – 80%

TABLE 4.3: Proportion of samples for which each distribution was the best fit, grouped by bin width. The COMb distribution is the best fit most of the time.

2353 **4.4.3 Relative goodness-of-fit for binomial, beta-binomial, and COMb distri-**
2354 **butions**

2355 In the previous section we showed that the COMb distribution was usually a better option
2356 than the binomial or beta-binomial distributions when attempting to fit a distribution to a
2357 sample of the number of active neurons. In this section, we aim to illustrate typically how
2358 much better the COMb distribution is.

2359 **Log likelihoods of distributions fitted to stimulated and unstimulated responses**

2360 We fitted binomial, beta-binomial, and COMb distributions to two windows in each of the 160
2361 trials with a visual stimulus. One of the windows was the last full window before stimulus
2362 onset. The other window was the first full window after stimulus onset. We measured the log
2363 likelihood for each fitted distribution. For the histograms of these log likelihood values for
2364 data from the primary visual cortex using 1ms bin width, see figure 4.7.

2365 Comparing unstimulated to stimulated windows, we observed that the log likelihood val-
2366 ues were greater for the unstimulated windows for all three distributions. This shows that the
2367 distributions were fitting better to the number of active neurons in the unstimulated windows.
2368 This might be due to a greater diversity in the distributions of number of active neurons in
2369 the stimulated windows (see figure 4.3). We saw similar results for the primary visual cortex
2370 when using 5ms and 10ms bin widths. For other regions, the histograms for unstimulated
2371 and stimulated windows were more similar, covering similar ranges of log likelihoods.

2372 We observed a marginal increase in the log likelihoods from binomial to beta-binomial to
2373 COMb distributions for both unstimulated and stimulated windows. But, the distribution of
2374 the log likelihoods looked quite similar for all three distributions. So, the COMb distribution
2375 only fits a little bit better than the other two distributions. We observed similar results when
2376 using different time bin widths, and data from different brain regions.

4.4. Results

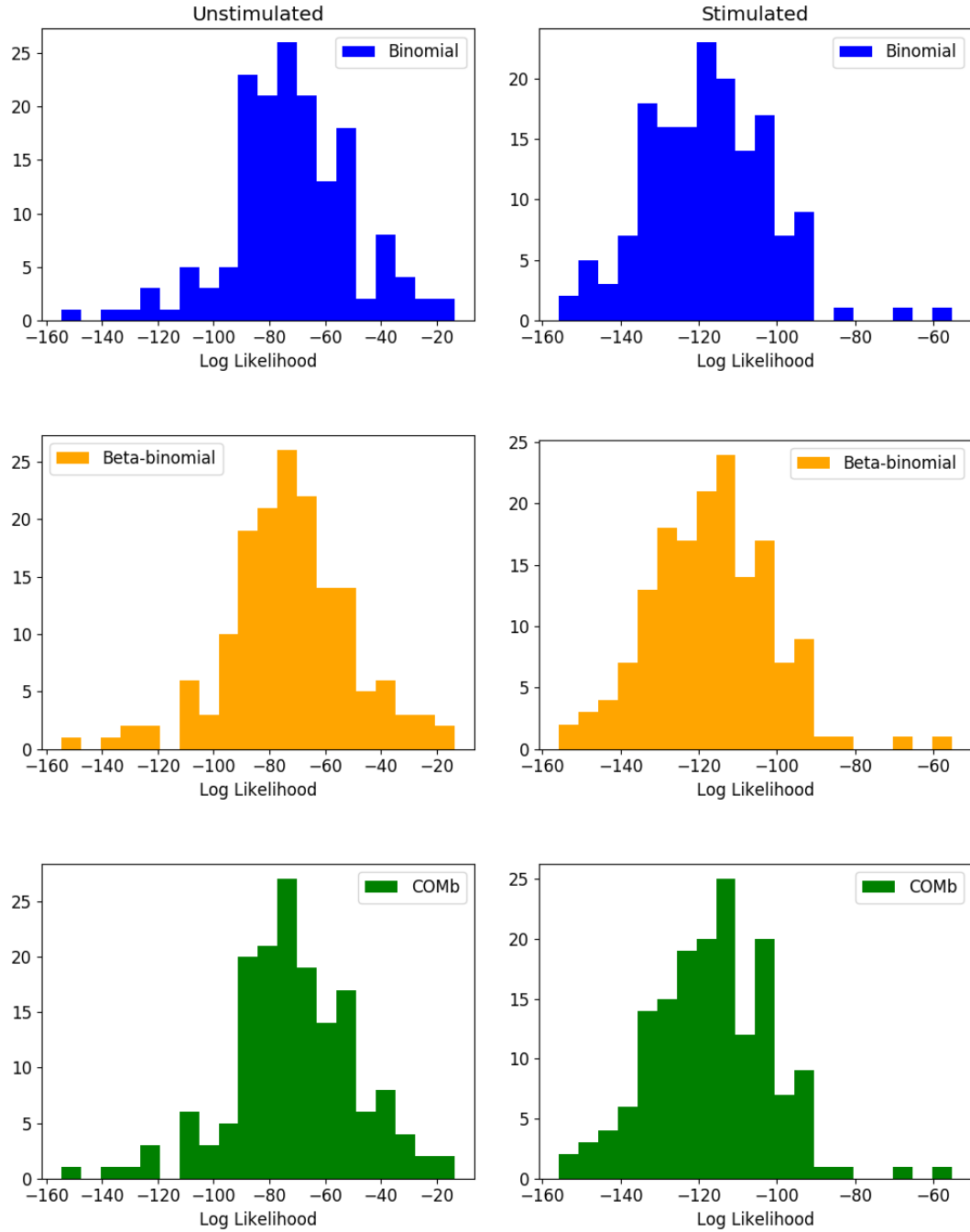


FIGURE 4.7: Number of active neurons data from the primary visual cortex, 1ms bin widths. (Left column) Histograms of log likelihoods for the binomial, beta-binomial, and COMb distributions fitted to windows where no visual stimulus was present. 160 trials. (Right column) Similar histograms for windows where a visual stimulus was present. 160 trials. In both cases, there are marginal increases in the log likelihoods from binomial to beta-binomial to COMb. The log likelihoods are larger for the unstimulated windows.

2377 **Distribution of fitted parameters for stimulated and unstimulated responses**

2378 We recorded the fitted parameters of each of the three distributions fitted to both the unstim-
2379 ulated and stimulated windows mentioned in section 4.4.3. We noticed an increase in the
2380 binomial distribution’s parameter for the stimulated windows (figure 4.8 top row). When
2381 we used wider bin widths, we noticed the same relative increase from unstimulated to stim-
2382 ulated windows, and the values over which the parameter was distributed increased. The
2383 relative increase from unstimulated to stimulated windows was also visible in data from the
2384 hippocampus, but not in other regions.

2385 For the beta-binomial distribution, we converted the fitted α and β parameters to π and
2386 ρ parameters (see Methods section 4.3.5) before examining their histograms. In this form,
2387 the $0 \leq \pi \leq 1$ parameter is a location parameter, and the $\rho > 0$ parameter is a shape
2388 parameter than encodes over-dispersion in the distribution relative to a binomial distribution.
2389 Comparing distribution of parameters fitted to the unstimulated windows to the distribution
2390 of those fitted to the stimulated windows, we observed slight increases in both the π and ρ
2391 paramters (figure 4.8 middle row). When we used a wider bin width, the paramter values were
2392 distributed across larger absolute values. The results comparing unstimulated to stimulated
2393 distributions were similar to the 1ms case. For the other regions, we observed similar results
2394 in the hippocampus. All the other regions show little difference between unstimulated and
2395 stimulated histograms in a given bin width. As we increased the size of the bin width used
2396 the absolute values across which the parameters were distributed increased.

2397 For the COMb distribution, the ν paramter was distributed around 1 for the unstimulated
2398 windows. For the stimulated windows ν was more tightly distributed and centred around
2399 0.75. This reflects a positive association between the neurons present immediately after stim-
2400 ulus onset. We also observed that the p parameter was distributed over slightly greater values
2401 for the stimulated windows as compared to the unstimulated (figure 4.8 bottom row). For
2402 increased bin widths, we observed that the ν parameter was distributed lower than for the
2403 1ms bin width case. The reduction in ν at for the stimulated windows was still present. We
2404 observed this drop in the ν parameter in the hippocampal data also, albeit to a lesser extent
2405 than in the primary visual cortex. We didn’t observe differences in the the data from the other
2406 regions.

4.4. Results

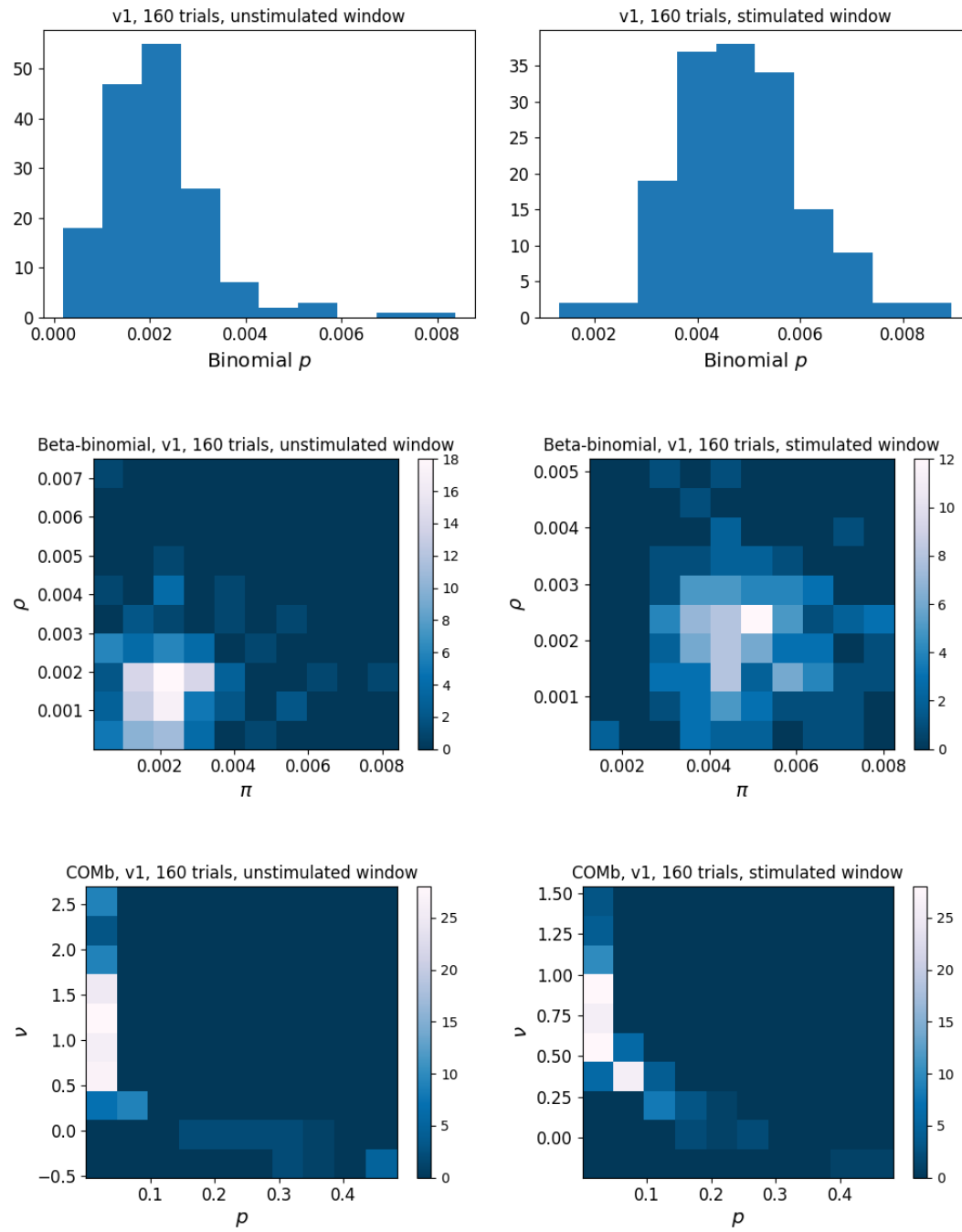


FIGURE 4.8: Histograms of fitted parameters for binomial, beta-binomial, and COMb distributions. Distributions fitted to data from the primary visual cortex, using 1ms bin widths. (Left column) The distributions were fitted a window before the onset of the visual stimulus. (Right column) The distributions were fitted to a window immediately after the onset of the visual stimulus.

2407 **Examples of empirical distributions and fitted distributions**

2408 In figure 4.9 there are some examples of fitted binomial, beta-binomial, and COMb distri-
2409 butions alongside the empirical distributions to which they are fitted. We can see that these
2410 fitted distributions over distributed their probability mass to $P(0)$ (or $P(0)$ and $P(1)$ for the
2411 thalamus) and underdistributed their probability mass elsewhere. Also, each of the three fit-
2412 ted distributions look similar in each example. This is in agreement with our observations in
2413 section 4.4.3.

2414 **4.4.4 Conway-Maxwell-binomial distribution captures changes in association
2415 at stimulus onset**

2416 We fit a Conway-Maxwell-binomial (COMb) distribution to the number of active neurons in
2417 the 1ms time bins in a 100ms sliding window. We also measured the correlation coefficient
2418 between the spike counts of all possible pairs of neurons, and took the average of these
2419 coefficients. We did this for all the trials with a visual stimulus. We observed a reduction in
2420 the COMb distribution's ν parameter at stimulus onset from around 1 to between 0 and 1 (see
2421 figure 4.10a). A value of ν less than 1 indicates positive association between the neurons (see
2422 section 4.3.5). We might expect to see this positive association reflected in the correlation
2423 coefficients, but this is not the case. We see no change in the time series of average correlation
2424 measures at stimulus onset.

2425 This may be due to the very short time bin we used in this case. We know that using small
2426 time bins can artificially reduce correlation measurements (Cohen and Kohn, 2011). In this
2427 case, fitting the COMb distribution may be a useful way to measure association in a neuronal
2428 ensemble over very short timescales (< 10ms).

2429 **4.4.5 Replicating stimulus related quenching of neural variability**

2430 Churchland et al. (2010) inspected the effect of a stimulus on neural variability. One of the
2431 measures of neural variability that they employed was the Fano factor of the spike counts of
2432 individual cells (see section 4.3.4). They found a reduction in neural variability as measured
2433 by the Fano factor in various cortical areas in a macaque at the onset of various visual stimuli,
2434 or a juice reward (Churchland et al., 2010).

2435 We measured the Fano factor of the spike count of each cell in each brain region, during
2436 each trial. We measured the mean and standard error of these Fano factors from 500ms before
2437 stimulus onset until 1000ms after stimulus end. For the primary visual cortex, we found a

4.4. Results

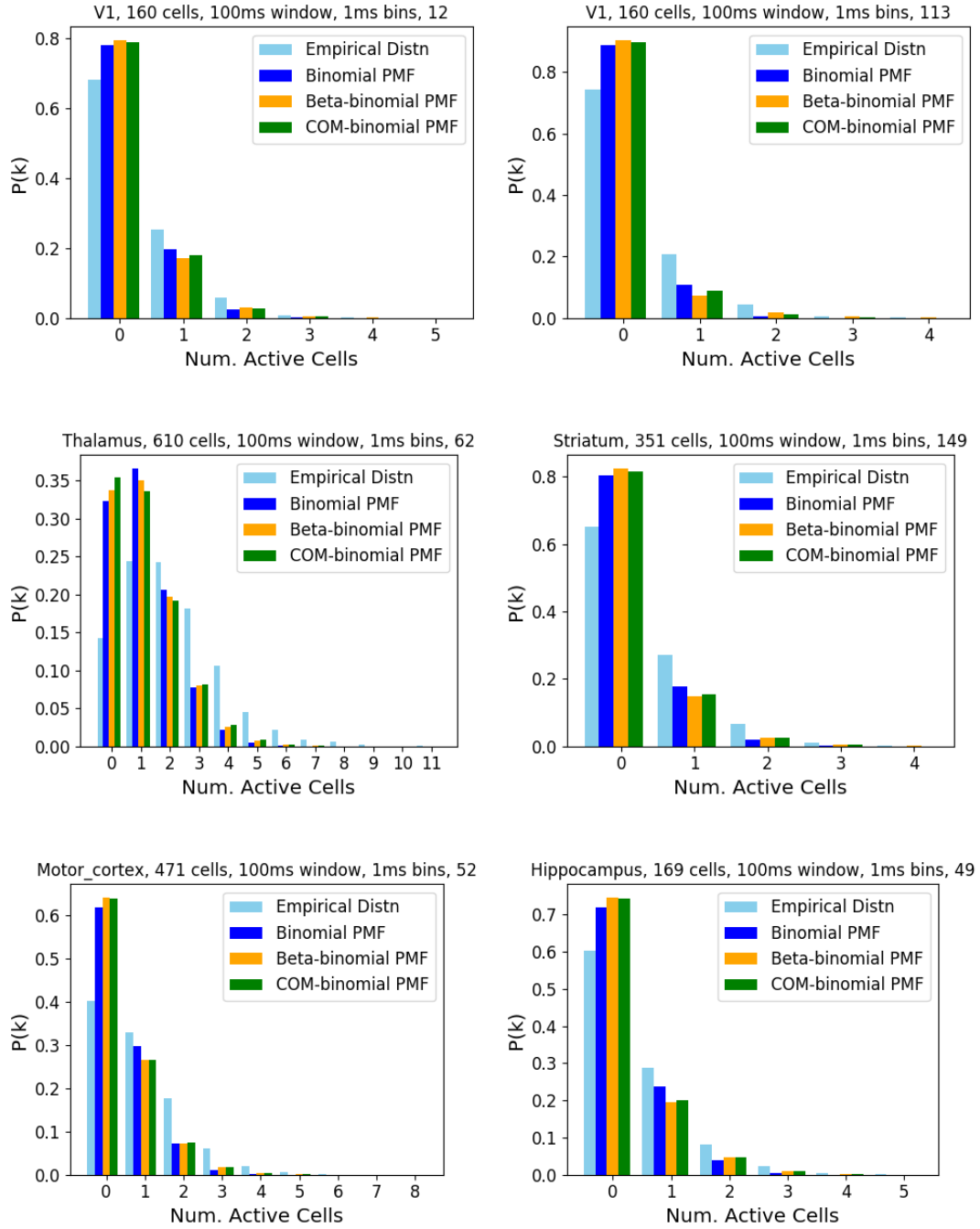


FIGURE 4.9: Examples of empirical and fitted distributions. At least one example from each of the 5 brain regions from which we had data.

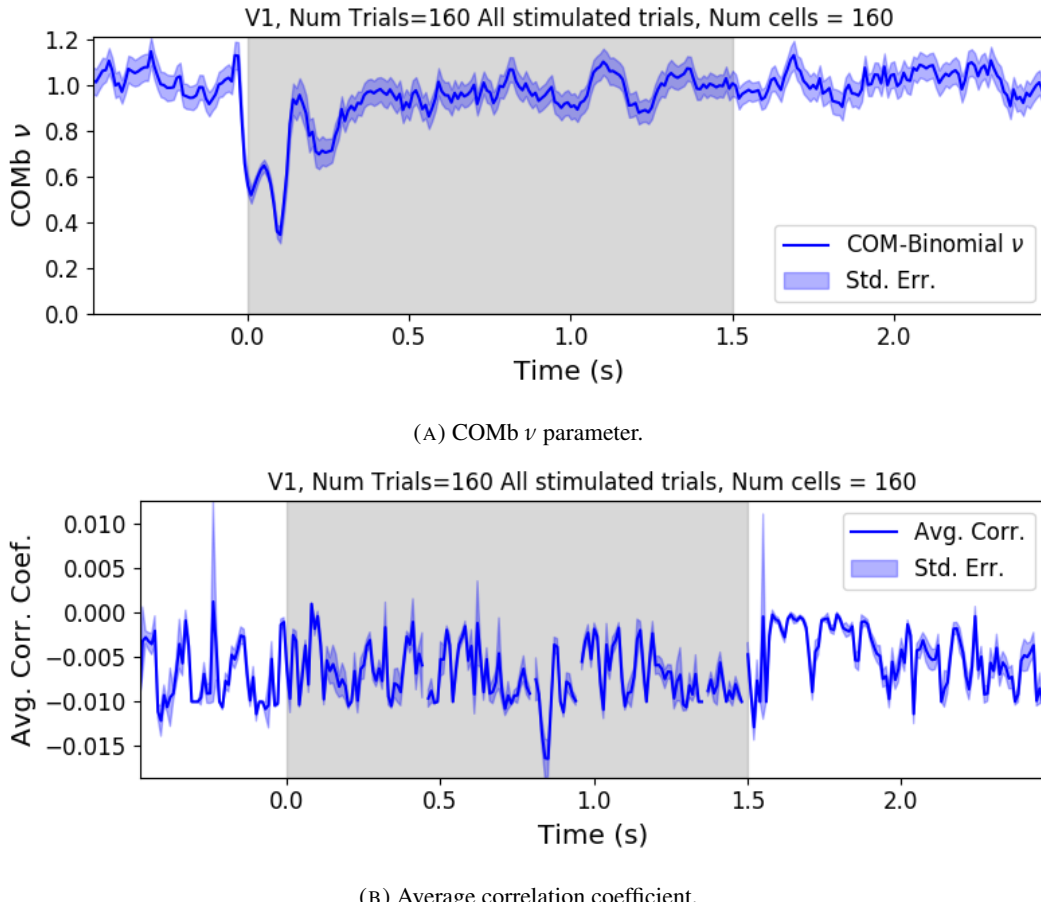


FIGURE 4.10: (A) We fit a Conway-Maxwell-binomial distribution to the number of active neurons in 1ms time bins of a 100ms sliding window. We did this for all trials with a visual stimulus and took the average across those trials. We see a transient drop in value for the distribution's ν parameter at stimulus onset. This shows an increase in positive association between the neurons. (B) We measured the correlation coefficient between the spike counts of all possible pairs of neurons in the same sliding window. The took the average of those coefficients. We also did this for every visually stimulated trial, and took the average across trials. The increase in positive association is not reflected with an increase in average correlation.

2438 transient reduction in the Fano factor immediately after stimulus onset. We used a Mann-
 2439 Whitney U test to check that the Fano factors measured in a window starting at stimulus
 2440 onset and ending 100ms later were significantly lower than the factors measured in a window
 2441 ending at stimulus onset ($p < 0.001$, see figure 4.11a). We did not get this statistically
 2442 significant result in any other region.

2443 Our findings agree with those of Churchland et al. for the primary visual cortex. However
 2444 Churchland also found a reduction in the Fano factor in the dorsal premotor cortex (PMd) at
 2445 stimulus onset. Our measurements from the mouse motor cortex show no change at stimulus
 2446 onset (see figure 4.11b). This could indicate some difference in the functionality of the motor
 2447 cortex in a macaque and the motor cortex of a mouse.

4.4. Results

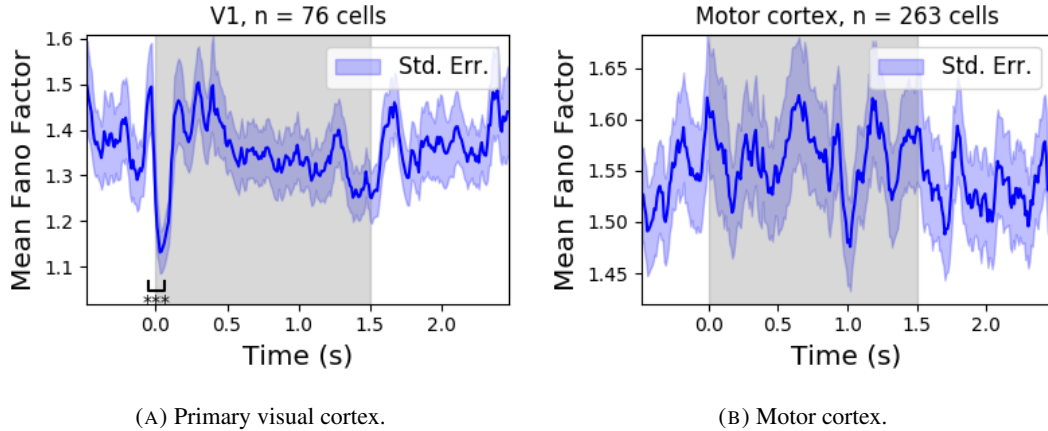


FIGURE 4.11: (A) The mean Fano factor of the spike counts of the cells in the primary visual cortex. Means were taken across cells first, then across trials. There was a significant decrease in the Fano factors immediately after stimulus onset. (B) The mean Fano factor of the spike counts of the cells in the motor cortex. No significant change in measurements at any point.

2448 Similar to these findings in the Fano factor, we found a reduction in the ν parameter of
 2449 the COMB distribution on stimulus onset in V1 (figure 4.10a) and in no other region from
 2450 which we had data. Specifically, the ν parameter reduced from around 1, to between 1 and 0.
 2451 This represents a change from no association between the neurons, to a positive association.
 2452 It is possible that this positive association may be responsible for the reduction in the Fano
 2453 factor.

2454 **4.4.6 Effects of greater bin widths**

2455 Using a greater bin width (10ms) affected the scale and shape of the most of the measure-
 2456 ments taken (described in section 4.3.3). The average correlation coefficient is the exception
 2457 to this. The 10ms bin width is still so small that the average correlation coefficient was also
 2458 small (similar scale as figure 4.10b).

2459 Using the greater bin width acted as a low pass filter on the other measurements taken
 2460 and the parameters of the fitted distributions. For example compare figure 4.10a to figure
 2461 4.12a. Note also that the ν parameter varies between 0.6 and 0.2 when using the 10ms bin
 2462 width. This indicates some positive association between the neurons at all times, even when
 2463 not stimulated or when adapted to the stimulus. This may be caused by the wider bin width
 2464 resulting in more neurons classified as active. The change in association at stimulus onset is
 2465 still captured by the change in the ν parameter.

2466 The mean number of active neurons was about 10 times greater for a 10ms bin width
 2467 compared to a 1ms bin width. The variance in the number of active neurons was also greater

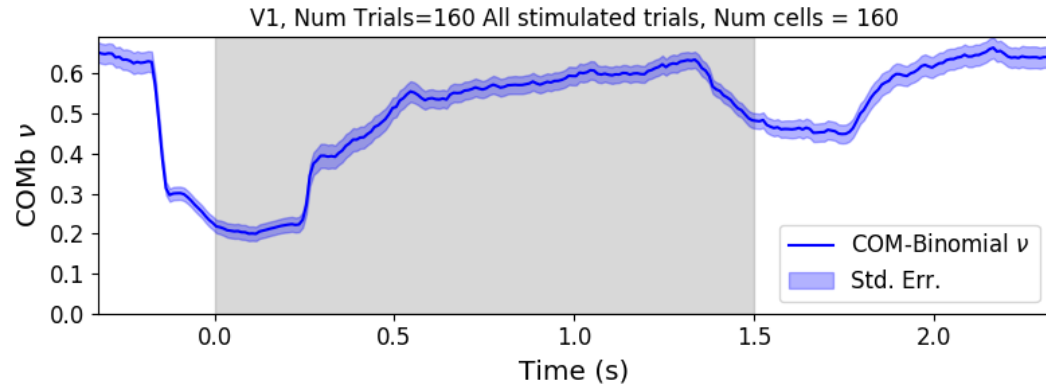
2468 for the wider bin width. This caused a change in the scale of the Fano factor (see figure 4.12b
2469 compared to figure 4.11a). Also, the reduction in the mean Fano factor at stimulus onset is
2470 not significant when using the 10ms bin width (Mann-Whitney U test, $p = 0.07$). This is
2471 likely due to greater variance in the Fano factors of the individual cells. Bear in mind that we
2472 are using the activity in each bin (either 0 or 1) rather than the actual spike counts in each bin.
2473 When using a 1ms bin width, there is no difference between the spike count and the activity
2474 but when using a wider bin width, there may be more than one spike per bin.

2475 4.5 Discussion

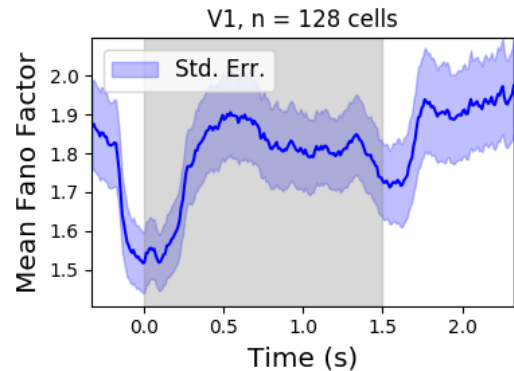
2476 Our aim in this research was to develop a new statistical method for analysing the activity
2477 of a neuronal ensemble at very short timescales. We wanted our method to use information
2478 taken from the whole ensemble, but we also wanted the method to be quick and easy to
2479 implement. It is likely that analysis methods with these characteristics will become valuable
2480 as electrophysiological datasets include readings from more cells over longer time periods. In
2481 this case, we used the number of active, or spiking, neurons in a very short time bin (< 10ms)
2482 as a measure of ensemble activity.

2483 First of all, we showed that there were changes in response that we could model at these
2484 very short time scales in some of the brain regions from which we had recordings. We ob-
2485 served changes in the average number of active neurons, and the variance of the number of
2486 active neurons in three different brain regions in response to visual stimuli. Since we know
2487 that correlated behaviour is associated with sensory perception (deCharms and Merzenich,
2488 1996), we might hope to measure the pairwise correlations within the neuronal population
2489 in order to further investigate these responses. But, using such short time bins can produce
2490 artificially small spike count correlation measurements (Cohen and Maunsell, 2009). Over-
2491 coming this limitation was one of our objectives for our new method. In order to do this, we
2492 abandoned the idea of measuring the correlations directly and embraced the concept of *asso-*
2493 *ciation*. In order to quantify the association between neurons, we used the Conway-Maxwell-
2494 binomial distribution to model the number of active (spiking) neurons in an ensemble as a
2495 sum of possibly associated Bernoulli random variables.

2496 We showed that the Conway-Maxwell-binomial distribution performed better than the
2497 more common options of the binomial and beta-binomial distributions. Furthermore, we
2498 showed that the positively associated behaviour between neurons in the primary visual cortex
2499 could be captured by fitting a Conway-Maxwell-binomial distribution, but was not captured



(A) Primary visual cortex ν parameter, bin width is 10ms.



(B) Primary visual cortex Fano factor, bin width is 10ms.

FIGURE 4.12: (A) The mean ν parameter of the COMb distribution fitted to activity in the primary visual cortex. Mean taken across all stimulated trials. A bin width of 10ms was used to classify cells as active or inactive. The change in association at stimulus onset is still captured. Some high frequency fluctuations are filtered out by using the wider bins (compare to figure 4.10a) (B) The mean Fano factor of the cells in the primary visual cortex. The change in the mean Fano factor at stimulus onset is not significant when using a bin width of 10ms.

2500 by the more standard approach of measuring the spike count correlation. The associated
2501 behaviour could not be measured using spike count correlations, because of the very short
2502 bins required to capture short timescale behaviour.

2503 We replicated a famous result from Churchland et al (2010) relating to the quenching of
2504 neural variability in cortical areas at stimulus onset, and in doing so, we established a corre-
2505 spondence between the association quantifying parameter of the Conway-Maxwell-binomial
2506 (COMb) distribution and the neural variability as measured by the Fano factor. We found a
2507 reduction in the ν parameter of the COMB distribution at stimulus onset, indicating a change
2508 from no association to positive association between neurons in V1. We found a corresponding
2509 reduction in the Fano factor of the individual cells in V1. The positive association between
2510 neurons induced by the stimulus would constrain the neurons to fire at the same time. The
2511 stimulus also induced a larger number of neurons to spike. These two actions combined could
2512 cause an increase in the firing rate of individual cells that is greater in magnitude than the in-
2513 crease in firing rate variability. If this is indeed the case, then the association as captured by
2514 the COMB distribution could be regarded as one of the ‘natural parameters’ of the ensemble
2515 response for short timescales. That is, a quantity that directly measures some aspect of the
2516 behaviour of the ensemble. In this case, it the correlated behaviour of the individual neurons
2517 is captured.

2518 This work could be just a first step in creating analysis methods based on the Conway-
2519 Maxwell-binomial distribution, or similar statistical models. One way to extend the method
2520 would be to pair it up with the ‘Population Tracking model’ (O’Donnell et al., 2017). This
2521 model attempts to characterise the interaction between an ensemble and each member of the
2522 ensemble by quantifying the probability of spiking for a given a cell, given the number of
2523 active cells in the whole population. Combining this model with the COMB distribution
2524 would give us a model that could accurately fit the number of active neurons at any moment,
2525 and that gives a probability of firing for each cell, and therefore probabilities for full spiking
2526 patterns, without adding a huge number of parameters to fit.

2527 A more complex way to extend the model would be to fit a Conway-Maxwell-binomial
2528 distribution to data recorded from multiple brain regions simultaneously, with a different fit
2529 for each region, then to analyse the temporal relationship between the fitted parameters of
2530 each region. If we analysed the time series of the COMB distribution parameters from the
2531 different regions, looking at cross-correlations between regions, this may give some results
2532 relating to the timescales in which information is processed in different brain regions.

2533 **Chapter 5**

2534 **Studies with practical limitations &**
2535 **negative results**

2536 *Abstract*

2537 Here I will present some details on research topics that I started, but that unfortunately did not
2538 lead anywhere useful. There are two pieces of research, based on two papers. Each paper is
2539 related to the overall theme of my PhD of analysing and modelling behaviours of populations
2540 of neurons. The first part is based on a model of parallel spike trains including higher order
2541 interactions by Shimazaki et al (2012). The second part is based on a multiscale model for
2542 making inferences on hierarchical data.

2543 **5.1 Dynamic state space model of pairwise and higher order neu-**
2544 **ronal correlations**

2545 In their paper Shimazaki et al (2012) aimed to model spike trains from populations of neurons
2546 in parallel, with pairwise and higher order dynamic interactions between the trains. They
2547 modelled the spike trains as multi-variate binary processes using a log-linear model, and they
2548 extracted spike interaction parameters using a Bayesian filter/EM-algorithm. They developed
2549 a goodness-of-fit measure for the model to test if including these higher order correlations
2550 is necessary for an accurate model. Their measure was based on the Bayes factor but they
2551 also assessed the suitability of higher order models using the AIC and BIC. So the increase
2552 in the number of parameters associated with fitting higher order interactions was taken into
2553 account. They tested the performance of the model on synthetic data with known higher
2554 order correlations. They used the model to look for higher order correlations in data from
2555 awake behaving animals. They use the model to demonstrate dynamic appearance of higher
2556 order correlations in the monkey motor cortex (Shimazaki et al., 2012).

2557 We used the available Python repository to implement the model, and we successfully
2558 worked through the tutorial provided. But we found that the model did not scale well to
2559 larger populations. We attempted to fit the model to a population of 10 neurons and found we
2560 didn't manage to finish the process. Since, our goal was to find a model to scale to hundreds
2561 or thousands of neurons, we decided that this model was no longer worth pursuing.

2562 **5.2 A multiscale model for hierarchical data applied to**
2563 **neuronal data**

2564 In their paper Kolaczyk et al (2001) developed a framework for a modelling hierarchically
2565 aggregated data, and making inferences based on a model arising from this framework. They
2566 assumed that a hierarchical aggregation existed on the data in question, where each element at
2567 each level of the hierarchy had some associated measurements, an associated mean process,
2568 which was the expected value of these measurements. They also assumed that the measure-
2569 ments of each parent were equal to the sum of the measurements from all of its children.
2570 They showed that these assumptions gave rise to a relationship between parent and child
2571 measurements across all levels of the hierarchy, where the product of the likelihood of the
2572 parameters of the lowest level of the hierarchy can be expressed as products of conditional
2573 likelihoods of the elements of higher levels of the hierarchy (Kolaczyk and Huang, 2010).

5.2. A multiscale model for hierarchical data applied to neuronal data

2574 We hoped that the hierarchical structure of the brain (regions to subregions to cells) and a
2575 high level activity measure (fMRI or EEG) could be combined with this model to infer lower
2576 level activity from a high level measure.

2577 They gave examples of these expressions for measurements sampled from Gaussian dis-
2578 tributions, and Poisson distributions, and showed the definitions of the hierarchical param-
2579 eters which reparametrise the distribution of these data taking the hierarchy into account.
2580 They go on to suggest prior distributions for this multiscale model, and integrate these priors
2581 to give posterior distributions for the measurements from each element at each level in the hi-
2582 erarchy, and expressions for the MAP estimated parameters of each the associated processes
2583 (Kolaczyk and Huang, 2010).

2584 We implemented their model in Python by creating some synthetic data from Poisson
2585 distributions, and defining a hierarchy by agglomerating these data. We calculated the MAP
2586 estimates using our knowledge of the hierarchy, and using the expressions given in the paper.
2587 We found that the MAP estimates were far less accurate than would be achieved by simply
2588 ignoring the hierarchy during estimation, and using a maximum likelihood approach. After
2589 that, we decided to move on.

2590 **Chapter 6**

2591 **Discussion**

2592 In this project, we attempted to address some of the challenges in data collection from
2593 large neuronal ensembles (specifically with calcium imaging) and some of the problems in
2594 analysing the data collected from large neuronal ensembles.

2595 Firstly, we investigated the relationship between cell biochemistry, action potentials and
2596 the fluorescence traces produced by fluorescent calcium indicators. We did this by building
2597 a biophysical model that takes in a spike train and returns the fluorescence trace that that
2598 spike would induce. The model included mechanics for the binding of calcium to fluorescent
2599 and endogenous mobile and immobile buffers, and the consequent changes in concentration
2600 of free and bounded calcium. The model consisted of 17 parameters, 13 of which were
2601 set according to data from the literature, and 4 of which were free parameters. We trained
2602 the model using simultaneously collected spiking and calcium imaging data (Berens et al.,
2603 2018). We fitted the model by matching the $\Delta F/F_0$ in response to an action potential, and
2604 by matching the power spectrum of the actual fluorescence trace. This meant that our model
2605 would include the correct amount of noise as well as return the correct change in amplitude
2606 in response to an action potential.

2607 Since our model produced fluorescence traces, we could apply spike inference algorithms
2608 to the modelled fluorescence traces that our model produced after training, and compare the
2609 performance of the algorithms on the modelled traces to their performance on the real traces.
2610 We used three spike inference algorithms, two of which were based on modelling the cal-
2611 cium trace as an autoregression (Friedrich and Paninski, 2016; Pnevmatikakis et al., 2016),
2612 and another inference algorithm that was a little more biologically inspired, but amounted to
2613 a very similar algorithm (Deneux et al., 2016). We compared the performance of the algo-
2614 rithms by using them to infer spikes from 20 real and modelled fluorescence traces induced
2615 by 20 corresponding real spike trains. We then used several binary classification measures
2616 (true positive rate, accuracy etc.) to asses the quality of the spike inference for the real and

2617 modelled fluorescence traces. We found that the spike inference algorithms performed sim-
2618 ilarly on real and modelled traces, showing that our model is capturing at least some of the
2619 characteristics of the real fluorescence traces.

2620 In order to investigate the effect of indicator characteristics on the modelled fluorescence
2621 trace and spike inference quality, we perturbed the indicator's affinity and dissociation rate
2622 in parallel, keeping the ratio of the two the same for all perturbations. We measured the SNR
2623 of the trace, and the true positive rate of the spike inference algorithms at each perturbed
2624 value pair. We found that perturbing the values lower caused in decrease in SNR and spike
2625 inference quality. This shows that our model could be used to test theoretical fluorescent cal-
2626 cium indicators without having to actually manufacture them. Experimental neuroscientists
2627 could also use our model to judge which indicator characteristics are most influential in their
2628 experimental context.

2629 We then investigated the effect of perturbing buffer concentration, and indicator concen-
2630 tration, on the signal-to-noise ratio of the modelled fluorescence trace and spike inference
2631 quality. This was a worthwhile experiment because endogenous buffer concentrations vary
2632 from cell to cell (Bartol et al., 2015; Maravall et al., 2000; Neher and Augustine, 1992), as
2633 does indicator expression (Chen et al., 2013). We found that extreme perturbations away
2634 from the indicator concentration taken from the literature lowered the SNR of the trace, and
2635 the spike inference quality. We also found that increases in the concentration of endogenous
2636 buffer above the value taken from the literature caused a decrease in the SNR and spike infer-
2637 ence quality. This reiterates that the indicator and endogenous buffers compete to bind with
2638 free calcium molecules, and this has an effect on fluorescence and consequently on spike
2639 inference.

2640 We then created some synthetic spike trains with controlled mean firing rates sampled
2641 the rates from an Ornstein-Uhlenbeck process. We found that the higher the firing rate, the
2642 lower the accuracy of the spike inference algorithms. But the mean firing could perhaps be
2643 inferred from the amplitude of the fluorescence traces. The higher firing rate, the higher the
2644 amplitude. Calibrating the model to facilitate and accurate measurement would require some
2645 kind of ground truth, but relative comparisons could be made without any other knowledge
2646 of the underlying spiking process.

2647 One obvious limitation to our model is the lack of binding mechanics for both the indi-
2648 cator and endogenous buffers. Greenberg et al included these mechanics in their successful
2649 spike inference model. We felt that the timescale of these binding mechanics was so small in
2650 comparison to the fluorescence dynamics that omitting them would make no difference. But

2651 it is possible that their inclusion would improve our model.

2652 After investigating the difficulties with inferring spiking data from calcium imaging data,
2653 we moved from data collection to analysis and we decided to implement a new network anal-
2654 ysis method on data from a neuronal ensemble. Using an electrophysiological dataset with
2655 spike sorted data from 9 different brain regions in 3 mice (Steinmetz, Carandini, and Harris,
2656 2019), we binned the spike times for each cell into spike counts for each cell and measured
2657 the correlation coefficients between these spike counts for a selection of cells evenly dis-
2658 tributed across the 9 regions. We repeated these measurements for time bin widths ranging
2659 from 5ms to 3s. We rectified these measurements and, for a given time bin width, used them
2660 as weights for a weighted undirected graph where each node represents a neuron, and the
2661 weight of each edge is the correlation between the neurons represented by the nodes on that
2662 edge. We applied a novel spectral analysis and community detection method (Humphries
2663 et al., 2019) to this network. This clustered the nodes in our ensemble into communities
2664 whose behaviour was more correlated than expected. Our measure of 'expected correlation
2665 strength' were based on a random network that matched our data network's sparsity and total
2666 weight. We compared the detected communities to the anatomical division of our cells using
2667 clustering comparison measures. We then conditioned the binned spike counts on the be-
2668 haviour of the mouse using the principal components of a video of the mouses face recorded
2669 simultaneously with the electrophysiology. We broke the total covariance down into 'spike
2670 count covariance' and 'signal covariance' components conditioning on the behavioural data
2671 and using the law of total covariance. We then repeated our analysis for spike count corre-
2672 lations, and signal correlation. Finally, since our community detection method was only valid
2673 on graphs with non-negative weights, we used different methods for creating a non-negative
2674 graph from our total correlations, and we repeated our analysis on those graphs.

2675 Our first finding was that the time bin width used to bin spike times into spike counts had
2676 a effect on the mean magnitude of the correlations measured. The wider the bin, the higher
2677 the correlations. Not only that, we separated the pairs into positively and negative correlated
2678 pairs, and we found that positively correlated pairs have greater correlation coefficients when
2679 using a wider bin, and negatively correlated pairs have more negative correlation coefficients
2680 when using a wider bin. We also found that the width of the bin used had an effect on the
2681 distribution of the spike counts. For smaller bin widths, the distribution of spike counts was
2682 better represented by a skewed distribution like the Poisson distribution. For wider bins, the
2683 spike counts were better represented by a Gaussian distribution.

2684 Next we investigated the differences between correlations within regions and between

regions. When we divided the pairs according to those two groups, we found that the mean within-region correlations were higher at every bin width, and the difference between the two means grew with increasing bin width. When we split the pairs of cells according to their regions, we found that the mean within-region correlations in any given region were usually greater than the mean between-region correlations for any region pair involving that region. The difference between the mean within-region correlation and the highest between-region correlations involving that region grew smaller with increasing bin width. To investigate this further, we plotted these mean correlations in matrices. Although the mean within-region correlations were usually the highest value in their row or column, as the bin width increased, the mean between-region correlations grew in magnitude relative to the within-region figure.

Next we chose a null network model, and we used the ‘Network Noise Rejection’ process (Humphries et al., 2019) to check for additional structure in our correlation based data network that was not captured by the null model. We found additional structure for any bin width that we used. We also found that the dimensionality of the additional structure reduced as we increased the bin width. This could mean that the processes or representations that take place over longer timescales within the brain also take place in a lower dimensional space.

We applied a community detection method (Humphries, 2011) to the signal correlation networks arising from the network noise rejection. We found that the number of communities detected decreased with increasing bin width. We also noticed that at shorter bin widths, the detected communities were more likely to consist of cells from one brain region only. We investigated this further by using clustering comparison methods to compare the detected communities with the anatomical division of the cells. We found that for short timescales $< 50\text{ms}$ correlated communities tended to exist within anatomical regions, and for longer timescales $> 100\text{ms}$, the correlated communities tended to exist across anatomical regions. This is broadly in agreement with a similar finding for EEG data from humans performing semantic or memory tasks (Stein and Sarnthein, 2000). Von Stein et al. (2000) found that visual processing taking place locally in the visual system was captured in the gamma frequency range (25 – 70Hz), while semantic processing was captured in the beta range (12 – 18Hz), and tasks involving mental imagery and working memory retention were captured in the theta and alpha ranges (4 – 8Hz, and 8 – 12Hz respectively).

We then conditioned our correlation measures on the the mouse’s behaviour. This allowed us to create spike count correlation (or noise correlation) networks, and signal correlation networks (Cohen and Kohn, 2011). We applied our analysis to these networks. For the

spike count correlation networks we found very similar results to the total correlation networks. More communities at smaller bin widths, and communities resembled the anatomical division at smaller bin widths. Given that recent findings show that behaviour can account for correlated spiking in many areas of the brain (Stringer et al., 2019), these results for the spike count correlation show that this correlated behaviour is still processed locally at short timescales, while processes and representations that take more time make use of correlated activity across multiple regions.

For the signal correlations, we still found additional structure in these networks. But we always detected a smaller number of communities. These communities also had no relation to the anatomical division of the cells. This result shows that there are groups of cells across multiple brain regions that are activated similarly by certain behaviours.

All of the networks so far were based on rectified correlation measures, because the network noise rejection and community detection processing is (currently) only valid for networks with non-negative weights. For the final part of our analysis, we tried different ways of transforming our total correlations into non-negative quantities before applying our analysis. First of all we took the absolute value of our correlation measures. Our results were very similar to those for the rectified correlations with the exception that we detected more communities consistently. It is possible that using this method detects both positively and negatively correlated communities.

We also tried reversing the sign of all the correlations, then rectifying the network. We hope that this would allow us to detect the negatively correlated communities. We did detect communities in these networks, but never more than three, and these communities bore no relationship with the anatomical distribution of the cells.

There is a lot of potential for network science applications in computational neuroscience. For example, some pairwise measure other than correlation coefficients could be used as the weights of the graph. The synaptic connections between cells can be isolated in-vitro (Okun et al., 2015). A map of these synaptic connections could be used as the basis for directed graphs. The analysis methods applicable to directed graphs could give insights about the formation of synaptic connections, or the dynamic changes in these connections over time. Other methods of community detection could be used on directed or undirected graphs. We used a ‘hard’ clustering method in our research, that is, each neuron could be a member of one cluster/community only. ‘Fuzzy-clustering’ methods do exist, where each element of the set to be clustered could be a member of more than one cluster (Baadel, Thabtah, and Lu, 2016).

Having spent much time investigating correlated behaviour using coefficients of spike counts, we decided to try another method for capturing correlated behaviour in neuronal ensembles. We used electrophysiological data taken from 5 brain regions of an awake mouse exposed to visual stimuli (Steinmetz et al., 2019). We modelled the number of active neurons in a given brain region as the number of successes in a collection of dependent Bernoulli random variables using the Conway-Maxwell-binomial distribution. To avoid violating the Bernoulli assumption, we binned the spike times using 1ms bins. The Conway-Maxwell-binomial distribution is a two parameter extension of the standard binomial distribution. The extra parameter allows the distribution to capture possible positive or negative association between the Bernoulli trials (Kadane, 2016). This means that we are assuming that all the neurons are dependent in the same way. This is not an accurate assumption, but it allows us model the data in a simple way.

First of all we established that there were changes in the number of active neurons in response to the visual stimuli. This was the case in the hippocampus, thalamus, and primary visual cortex. Each region had its own signature response. We measured the mean and variance of the number of active neurons in a sliding window starting before stimulus onset, and finishing after the end of stimulus presentation.

As well as the Conway-Maxwell-binomial distribution, we also fitted binomial, and beta-binomial distributions to the number of active neurons in a sliding window. We found that the Conway-Maxwell-binomial distribution was the best fit for over 90% of the samples. This means that the COMb distribution is capturing some dependency between the neurons, because the binomial distribution assumes independence. Also the COMb distribution captures this dependence more accurately than the beta-binomial distribution, which does have some capacity for over dispersion.

Next we showed that the Conway-Maxwell-binomial distribution captured the change in association at stimulus onset better than the correlation coefficient. The extremely small bin width artificially shrunk the correlation coefficient to the point where this measurement didn't detect any correlated activity. But the association parameter of the COMb distribution detected some positive association between the neurons at stimulus onset. So, for particularly short time bins, where neurons can be treated as Bernoulli random variables, the Conway-Maxwell-binomial distribution is a good way to capture correlated behaviour. There are other measurements for capturing association to which this distribution should be compared. Cross-correlograms could be used for some measure of synchrony, for example.

2785 Finally, we replicated a famous finding of Churchland et al. (2010) relating to the quenching
2786 of neural variability at stimulus onset, thereby finding a parallel between this reduction
2787 in the Fano factor and a reduction in the association parameter of the COMb distribution.

2788 We showed that computational neuroscientists can make progress by being inventive with
2789 their statistical models. A similar distribution to investigate would be the Conway-Maxwell-
2790 Poisson distribution. This is similar to the standard Poisson distribution, but with an addi-
2791 tional parameter that allows for over- or under- dispersion relative to a Poisson distribution.
2792 This might be ideal for modelling firing rates of individual neurons. Some interaction be-
2793 tween the fitted parameters could capture the association between neurons.

2794 There is one technology that has the potential to take over from both electrophysiology
2795 and calcium imaging. The technique of voltage imaging has become more useful in recent
2796 years. The aim for neuroscience would be to develop a voltage imaging dye or protein that
2797 images the membrane potential of a neuron with enough spatial and temporal resolution to de-
2798 tect action potentials. The voltage imaging dyes that have been developed so far do not have
2799 high enough spatial resolution to single out individual cells in-vivo using staining (Bando
2800 et al., 2019). But, genetically encoded voltage indicators have been developed that have high
2801 enough resolution to indicate individual spikes and subthreshold activity from small numbers
2802 of cells in the striatum, hippocampus, and cortex of awake behaving mice (Piatkevich et al.,
2803 2019). These indicators have the potential to take over from calcium imaging, and if imaging
2804 deep within the brain becomes possible, electrophysiology could also be replaced. This is
2805 speculation, but the potential is there.

2806

Bibliography

- 2807 Allen, William E. et al. (2019). “Thirst regulates motivated behavior through modulation of
2808 brainwide neural population dynamics”. In: *Science* 364.6437.
- 2809 Baadel, S., F. Thabtah, and J. Lu (2016). “Overlapping clustering: A review”. In: *2016 SAI
2810 Computing Conference (SAI)*, pp. 233–237.
- 2811 Baldassano, Christopher et al. (2017). “Discovering Event Structure in Continuous Narrative
2812 Perception and Memory”. In: *Neuron* 95.3, 709 –721.e5.
- 2813 Bando, Yuki et al. (2019). “Genetic voltage indicators”. In: *BMC Biology* 17.1, p. 71.
- 2814 Bartol, Thomas M. et al. (2015). “Computational reconstitution of spine calcium transients
2815 from individual proteins”. In: *Frontiers in Synaptic Neuroscience* 7, p. 17.
- 2816 Berens, Philipp et al. (May 2018). “Community-based benchmarking improves spike rate in-
2817 ference from two-photon calcium imaging data”. In: *PLOS Computational Biology* 14.5,
2818 pp. 1–13.
- 2819 Bezanson, Jeff et al. (Sept. 2012). “Julia: A Fast Dynamic Language for Technical Comput-
2820 ing”. In: *MIT*.
- 2821 Brini, Marisa et al. (2014). “Neuronal calcium signaling: function and dysfunction”. In: *Cel-
2822 lular and Molecular Life Sciences* 71.15, pp. 2787–2814.
- 2823 Buccino, Alessio P. et al. (2019). “SpikeInterface, a unified framework for spike sorting”. In:
2824 *bioRxiv*.
- 2825 Chen, Tsai-Wen et al. (July 2013). “Ultrasensitive fluorescent proteins for imaging neuronal
2826 activity”. In: *Nature* 499, 295–300.
- 2827 Churchland, Mark M. et al. (2010). “Stimulus onset quenches neural variability: a widespread
2828 cortical phenomenon”. eng. In: *Nature neuroscience* 13.3. 20173745[pmid], pp. 369–378.
- 2829 Cohen, Marlene R. and Adam Kohn (2011). “Measuring and interpreting neuronal corre-
2830 lations”. In: *Nature Neuroscience* 14.7, pp. 811–819.
- 2831 Cohen, Marlene R. and John H. R. Maunsell (2009). “Attention improves performance pri-
2832 marily by reducing interneuronal correlations”. eng. In: *Nature neuroscience* 12.12. 19915566[pmid],
2833 pp. 1594–1600.

- 2834 Dana, Hod et al. (Sept. 2014). “Thy1-GCaMP6 Transgenic Mice for Neuronal Population
2835 Imaging In Vivo”. In: *PloS one* 9, e108697.
- 2836 deCharms, R. Christopher and Michael M. Merzenich (1996). “Primary cortical represen-
2837 tation of sounds by the coordination of action-potential timing”. In: *Nature* 381.6583,
2838 pp. 610–613.
- 2839 Deneux, Thomas et al. (July 2016). “Accurate spike estimation from noisy calcium signals
2840 for ultrafast three-dimensional imaging of large neuronal populations in vivo”. In: *Nature*
2841 *Communications* 7.1.
- 2842 Dombeck, Daniel A. et al. (2010). “Functional imaging of hippocampal place cells at cellular
2843 resolution during virtual navigation”. In: *Nature Neuroscience* 13.11, pp. 1433–1440.
- 2844 Éltes, Tímea et al. (2019). “Improved spike inference accuracy by estimating the peak am-
2845 plitude of unitary [Ca₂₊] transients in weakly GCaMP6f-expressing hippocampal pyra-
2846 midal cells”. In: *The Journal of Physiology* 597.11, pp. 2925–2947.
- 2847 Faas, Guido C. et al. (2011). “Calmodulin as a direct detector of Ca₂₊ signals”. In: *Nature*
2848 *Neuroscience* 14.3, pp. 301–304.
- 2849 Fiala, John C. and Kristen M. Harris (1999). *Dendrite Structure*.
- 2850 Flach, Boris (Sept. 2013). “A Class of Random Fields on Complete Graphs with Tractable
2851 Partition Function”. In: *IEEE transactions on pattern analysis and machine intelligence*
2852 35, pp. 2304–6.
- 2853 Forney, G. D. (1973). “The viterbi algorithm”. In: *Proceedings of the IEEE* 61.3, pp. 268–
2854 278.
- 2855 Fosdick, Bailey et al. (Aug. 2016). “Configuring Random Graph Models with Fixed Degree
2856 Sequences”. In: *SIAM Review* 60.
- 2857 Friedrich, Johannes and Liam Paninski (2016). “Fast Active Set Methods for Online Spike In-
2858 ference from Calcium Imaging”. In: *Advances in Neural Information Processing Systems*
2859 29. Ed. by D. D. Lee et al. Curran Associates, Inc., pp. 1984–1992.
- 2860 Ganmor, Elad, Ronen Segev, and Elad Schneidman (2011). “Sparse low-order interaction
2861 network underlies a highly correlated and learnable neural population code”. In: *Pro-
2862 ceedings of the National Academy of Sciences* 108.23, pp. 9679–9684.
- 2863 Girard, P., J. M. Hupé, and J. Bullier (2001). “Feedforward and Feedback Connections Be-
2864 tween Areas V1 and V2 of the Monkey Have Similar Rapid Conduction Velocities”. In:
2865 *Journal of Neurophysiology* 85.3. PMID: 11248002, pp. 1328–1331.
- 2866 Greenberg, David et al. (Nov. 2018). “Accurate action potential inference from a calcium
2867 sensor protein through biophysical modeling:” in:

Bibliography

- 2868 Gründemann, Jan et al. (2019). “Amygdala ensembles encode behavioral states”. In: *Science*
2869 364.6437.
- 2870 Hodgkin, A. L. and A. F. Huxley (1939). “Action Potentials Recorded from Inside a Nerve
2871 Fibre”. In: *Nature* 144.3651, pp. 710–711.
- 2872 Humphries, Mark et al. (Jan. 2019). “Spectral rejection for testing hypotheses of structure in
2873 networks”. In:
- 2874 Humphries, Mark D. (2011). “Spike-Train Communities: Finding Groups of Similar Spike
2875 Trains”. In: *Journal of Neuroscience* 31.6, pp. 2321–2336.
- 2876 Jun, James J. et al. (2017). “Fully integrated silicon probes for high-density recording of
2877 neural activity”. In: *Nature* 551.7679, pp. 232–236.
- 2878 Kadane, Joseph B. (June 2016). “Sums of Possibly Associated Bernoulli Variables: The
2879 Conway–Maxwell-Binomial Distribution”. In: *Bayesian Anal.* 11.2, pp. 403–420.
- 2880 Kilhoffer, Marie-Claude et al. (Sept. 1992). “Use of Engineered Proteins With Internal Tryp-
2881 tophean Reporter Groups and Perturbation Techniques to Probe the Mechanism of Ligand-
2882 Protein Interactions: Investigation of the Mechanism of Calcium Binding to Calmodulin”.
2883 In: *Biochemistry* 31.34, pp. 8098–8106.
- 2884 Koch, Christoff (1999). *Biophysics of Computation: Information Processing in Single Neu-*
2885 *rons*. Oxford University Press.
- 2886 Kolaczyk, Eric and Haiying Huang (Sept. 2010). “Multiscale Statistical Models for Hierar-
2887 chical Spatial Aggregation”. In: *Geographical Analysis* 33, pp. 95 –118.
- 2888 Lee, Suk-HO et al. (July 2000). “Differences in Ca²⁺ buffering properties between excitatory
2889 and inhibitory hippocampal neurons from the rat”. In: *The Journal of Physiology* 525.
- 2890 Litwin-Kumar, Ashok, Maurice Chacron, and Brent Doiron (Sept. 2012). “The Spatial Struc-
2891 ture of Stimuli Shapes the Timescale of Correlations in Population Spiking Activity”. In:
2892 *PLoS computational biology* 8, e1002667.
- 2893 Maravall, M et al. (May 2000). “Estimating intracellular calcium concentrations and buffer-
2894 ing without wavelength ratioing”. In: *Biophysical Journal* 78.5, pp. 2655–2667.
- 2895 Maugis, Pa (Jan. 2014). “Event Conditional Correlation: Or How Non-Linear Linear Depen-
2896 dence Can Be”. In:
- 2897 Meilă, Marina (2007). “Comparing clusterings—an information based distance”. In: *Journal*
2898 *of Multivariate Analysis* 98.5, pp. 873 –895.
- 2899 Murray, John D. et al. (2014). “A hierarchy of intrinsic timescales across primate cortex”. In:
2900 *Nature Neuroscience* 17.12, pp. 1661–1663.

- 2901 Neher, E. and G. J. Augustine (1992). “Calcium gradients and buffers in bovine chromaffin
2902 cells”. eng. In: *The Journal of physiology* 450. 1331424[pmid], pp. 273–301.
- 2903 O’Donnell, Cian et al. (Jan. 2017). “The population tracking model: a simple, scalable statis-
2904 tical model for neural population data”. English. In: *Neural Computation* 29.1, pp. 50–
2905 93.
- 2906 Okun, Michael et al. (2015). “Diverse coupling of neurons to populations in sensory cortex”.
2907 In: *Nature* 521.7553, pp. 511–515.
- 2908 Ouzounov, Dimitre G. et al. (2017). “In vivo three-photon imaging of activity of GCaMP6-
2909 labeled neurons deep in intact mouse brain”. eng. In: *Nature methods* 14.4. 28218900[pmid],
2910 pp. 388–390.
- 2911 Patterson, Carlyn A. et al. (2014). “Similar adaptation effects in primary visual cortex and
2912 area MT of the macaque monkey under matched stimulus conditions”. In: *Journal of*
2913 *Neurophysiology* 111.6. PMID: 24371295, pp. 1203–1213.
- 2914 Peron, Simon P. et al. (2015). “A Cellular Resolution Map of Barrel Cortex Activity during
2915 Tactile Behavior”. In: *Neuron* 86.3, pp. 783–799.
- 2916 Piatkevich, Kiryl D. et al. (2019). “Population imaging of neural activity in awake behaving
2917 mice”. In: *Nature* 574.7778, pp. 413–417.
- 2918 Pnevmatikakis, E.A. et al. (Jan. 2016). “Simultaneous Denoising, Deconvolution, and Demix-
2919 ing of Calcium Imaging Data”. In: *Neuron* 89.2, pp. 285–299.
- 2920 Pnevmatikakis, Eftychios et al. (Nov. 2013). “Bayesian spike inference from calcium imaging
2921 data”. In: *Conference Record - Asilomar Conference on Signals, Systems and Computers*.
- 2922 Pnevmatikakis, Eftychios et al. (Sept. 2014). “A structured matrix factorization framework
2923 for large scale calcium imaging data analysis”. In:
- 2924 Schneidman, Elad et al. (2006). “Weak pairwise correlations imply strongly correlated net-
2925 work states in a neural population”. eng. In: *Nature* 440.7087. 16625187[pmid], pp. 1007–
2926 1012.
- 2927 Shannon, C. E. (1948). “A Mathematical Theory of Communication”. In: *Bell System Tech-
2928 nical Journal* 27.3, pp. 379–423.
- 2929 Shimazaki, Hideaki et al. (2012). “State-space analysis of time-varying higher-order spike
2930 correlation for multiple neural spike train data”. eng. In: *PLoS computational biology*
2931 8.3. 22412358[pmid], e1002385–e1002385.
- 2932 Staude, Benjamin, Sonja Grün, and Stefan Rotter (2010). “Higher-Order Correlations and
2933 Cumulants”. In: *Analysis of Parallel Spike Trains*. Ed. by Sonja Grün and Stefan Rotter.
2934 Boston, MA: Springer US, pp. 253–280.

Bibliography

- 2935 Stein, Astrid von and Johannes Sarnthein (2000). “Different frequencies for different scales
2936 of cortical integration: from local gamma to long range alpha/theta synchronization”. In:
2937 *International Journal of Psychophysiology* 38.3, pp. 301 –313.
- 2938 Steinmetz, Nick, Matteo Carandini, and Kenneth D. Harris (2019). ”*Single Phase3*” and
2939 ”*Dual Phase3*” *Neuropixels Datasets*.
- 2940 Steinmetz, Nick et al. (Mar. 2019). “Eight-probe Neuropixels recordings during spontaneous
2941 behaviors”. In:
- 2942 Stevenson, Ian H. and Konrad P. Kording (2011). “How advances in neural recording affect
2943 data analysis”. In: *Nature Neuroscience* 14.2, pp. 139–142.
- 2944 Stringer, Carsen et al. (2019). “Spontaneous behaviors drive multidimensional, brainwide
2945 activity”. In: *Science* 364.6437.
- 2946 Tada, Mayumi et al. (2014). “A highly sensitive fluorescent indicator dye for calcium imaging
2947 of neural activity in vitro and in vivo”. In: *European Journal of Neuroscience* 39.11,
2948 pp. 1720–1728.
- 2949 Tian, Lin et al. (2009). “Imaging neural activity in worms, flies and mice with improved
2950 GCaMP calcium indicators”. eng. In: *Nature methods* 6.12. 19898485[pmid], pp. 875–
2951 881.
- 2952 Tkačik, Gašper et al. (2014). “Searching for collective behavior in a large network of sen-
2953 sory neurons”. eng. In: *PLoS computational biology* 10.1. 24391485[pmid], e1003408–
2954 e1003408.
- 2955 Treves, Alessandro and Stefano Panzeri (1995). “The Upward Bias in Measures of Informa-
2956 tion Derived from Limited Data Samples”. In: *Neural Computation* 7.2, pp. 399–407.
- 2957 Vinh, Nguyen Xuan, Julien Epps, and James Bailey (Dec. 2010). “Information Theoretic
2958 Measures for Clusterings Comparison: Variants, Properties, Normalization and Correc-
2959 tion for Chance”. In: *J. Mach. Learn. Res.* 11, 2837–2854.
- 2960 Vogelstein, Joshua T. et al. (Oct. 2010). “Fast nonnegative deconvolution for spike train infer-
2961 ence from population calcium imaging”. In: *Journal of neurophysiology* 104.6, 295–300.
- 2962 Wierzyński, ”Casimir M. et al. (2009). ””State-Dependent Spike-Timing Relationships be-
2963 tween Hippocampal and Prefrontal Circuits during Sleep””. In: ”*Neuron*” ”61.””4”, ”587
2964 –596”.
- 2965 Zariwala, Hatim A. et al. (2012). “A Cre-dependent GCaMP3 reporter mouse for neuronal
2966 imaging in vivo”. eng. In: *The Journal of neuroscience : the official journal of the Society*
2967 *for Neuroscience* 32.9. 22378886[pmid], pp. 3131–3141.

- 2968 Zou, Hui and Trevor Hastie (2005). “Regularization and variable selection via the Elastic
2969 Net”. In: *Journal of the Royal Statistical Society, Series B* 67, pp. 301–320.